Doctoral theses at NTNU, 2023:422

Thanh-Nam Tran

Development of tunable Y-junction laser diodes

for trace-gas sensing applications

Doctoral thesis

NTNU
Norwegian University of Science and Technology
Thesis for the Degree of Philosophiae Doctor
Faculty of Information Technology and Electrical Engineering
Department of Electronic Systems

NTNU
Norwegian University of Science and Technology

Thanh-Nam Tran

Development of tunable Y-junction laser diodes

for trace-gas sensing applications

Thesis for the Degree of Philosophiae Doctor

Trondheim, December 2023

Norwegian University of Science and Technology
Faculty of Information Technology and Electrical Engineering
Department of Electronic Systems

NTNU
Norwegian University of
Science and Technology

NTNU
Norwegian University of Science and Technology

Thesis for the Degree of Philosophiae Doctor

Faculty of Information Technology and Electrical Engineering
Department of Electronic Systems

ISBN 978-82-326-7544-9 (printed ver.)
ISBN 978-82-326-7543-2 (electronic ver.)
ISSN 1503-8181 (printed ver.)
ISSN 2703-8084 (online ver.)

Doctoral theses at NTNU, 2023:422

Printed by NTNU Grafisk senter

Abstract

Y-junction laser diodes are promising light sources needed for trace-gas sensing systems based on tunable diode-laser absorption spectroscopy. The merit of this laser structure is the fabrication simplicity and the ability for realization of tunable laser devices. This PhD dissertation presents successful development of widely tunable Y-junction laser diodes emitting in mid-infrared regime based on the optimization of laser growth and fabrication process.

Antimonide-based mid-infrared laser structures have been grown using molecular beam epitaxy Carrier concentration in the doped cladding layers play a key role in the electrical properties of the laser diodes. Thus, optimization of carrier concentration is required with regards to dopant density. Incorporation of tellurium (Te) and beryllium (Be) dopants in $Al_{0.9}Ga_{0.1}As_{0.06}Sb_{0.94}$ cladding layers was investigated to enhance the electrical properties while minimizing the defect levels for better optical properties. The dependence of carrier concentration and Hall mobility on dopant density for both n- and p-type doped AlGaAsSb cladding layers has been precisely determined using Hall effect and secondary ion mass spectrometry depth profile measurements. Carrier concentration was found to have linear dependence on the dopant density for Be-doped $Al_{0.9}Ga_{0.1}As_{0.06}Sb_{0.94}$ for dopant density up to 2.9×10^{19} cm^{-3}, whereas it gets saturated for Te-doped $Al_{0.9}Ga_{0.1}As_{0.06}Sb_{0.94}$ samples at 1.6×10^{17} cm^{-3} for dopant density values above 8.0×10^{18} cm^{-3}. Deep level transient spectroscopy revealed the presence of deep trap levels (most likely DX-centers) as a cause of low doping efficiency in the Te-doped $Al_{0.9}Ga_{0.1}As_{0.06}Sb_{0.94}$ samples.

The grown laser materials were processed into Fabry-Perot (FP) and Y-junction lasers with different configuration. Light confinement in a high loss waveguide such as the Y-junction structure requires a well-defined ridge waveguide structure. Such structure can be obtained from optimized photolithography processes and precise control of etching processes using *in situ* reflectance monitored inductively-coupled plasma reactive ion etching. The etch depth or the height of the ridge waveguide were precisely and repeatably controlled with an endpoint depth precision within ± 10 nm using this etching technique. As a result, significant improvement in the performance of Y-junction lasers has been achieved as compared to previous studies in our group.

For high performance operation of the laser diodes, low ohmic contact resistance to GaSb is highly desirable to enhance the carrier injection and minimize the heat generation in the contact region, thus reducing the heat inside the laser structure. Such good ohmic contact requires an oxide-free surface of GaSb, which is in contact with the metallic layers. Prior to metallization, several plasma-assisted techniques were applied to remove the native oxide of GaSb. The effect of these techniques on the contact properties in comparison to the conventional chemical methods was evaluated via the specific contact resistivity between the metallic layers and p-type GaSb, obtained from transfer length method (TLM) and four-point probe measurements. Very low specific contact resistivities of less than 5×10^{-8} Ω cm^2 (the limit for accurate TLM

measurement results) were observed after pre-surface treatment by H_2/Ar sputtering etching and low-ion-energy Ar irradiation. By eliminating sample exposure to air prior to metallization, *in situ* Ar irradiation is a promisingly reliable technique for fabrication of high performance GaSb-based semiconductor devices.

Aluminum (Al)-based metallizations to n- and p-type GaSb were demonstrated as an alternative for gold (Au)–based contacts in laser applications. Measurement of specific contact resistivities between metallic layers and n-/p-type GaSb showed that the Al-based contacts performed as good as the conventional Au-based contacts. The contact property between Al and p-type GaSb was even better after annealing. The potential reliability problem of this type of contact revealed by reliability test when used in some devices, due to interdiffusion, can be reduced by using a diffusion barrier. The good performance of GaSb-based straight waveguide edge emitting lasers using Al-based contacts shows the applicability of this type of contact in GaSb-based semiconductor devices.

Characterizations of FP laser diodes at room temperature (RT) and in continuous wave (cw) mode showed their good output performance in term of electrical, optical and spectral characteristics. The ridge waveguide lasers with 25 µm width and 1 mm length had maximum output power per facet of 20 mW, threshold current density of 200 A/cm^2 (67 A/cm^2 per quantum well), internal loss of 9.83 cm^{-1}, internal quantum efficiency of 40.6 % and characteristic temperature of 84.3 K. The laser diodes exhibited low operation voltage of 1 V which helped to reduce the heat generation inside the laser structure. Single mode behavior emission with full width at half maximum of ~ 0.1 nm and side mode suppression ratio (SMSR) > 14 dB were obtained for 5 µm wide (and below) straight waveguide. To improve the output performance and long-term stability of the GaSb-based laser diodes, optical coatings on the laser facets have been demonstrated. Different optical coatings including high reflection (HR) coating, anti-reflection (AR) coating, and partial HR were characterized by simulation and experimental works. At the desired wavelength of 2.33 µm, the reflectivities of the HR coating, AR coating and partial HR coating were measured to be 99 %, 7 % and 50 %, respectively. The effect of optical coatings on the performance of the GaSb-based edge emitting laser diodes has been examined. Significant improvement of the output performance of the laser diodes in terms of optical power, threshold current and differential quantum efficiency has been observed after applying one facet with HR coating and the other with AR coating.

Based on the optimization of laser growth and fabrication process, tunable Y-junction laser diodes of different configurations have been successfully fabricated and characterized at RT in cw mode. Y-junction structures with large bend radius and small length difference between the two cavities have been chosen to maximize the output power and wavelength tunability while having sufficient SMSR. Using a large bend radius of 1000 µm and a length difference of 20 µm between the two cavities, widely continuous tuning ranges up to 50 nm with the SMSR > 23 dB were achieved by adjusting the injected current ratio between different sections of the Y-junction lasers. The promising results show the applicability of the Y-junction lasers for trace-gas sensing applications.

Preface

This thesis is submitted as a partial fulfilment of the requirements for the Degree Philosophiae Doctor (Ph.D.) at the Norwegian University of Science and Technology (NTNU). This work has been carried out at the Department of Electronic Systems, Faculty of Information Technology and Electrical Engineering, under the supervision of Professor Bjørn-Ove Fimland and co-supervision of Professor Astrid Aksnes.

This work was funded by the Research Council of Norway under Grant No. 177610/V30, the Norwegian Micro- and Nano-Fabrication Facility under Grant No.197411/V30, and the Norwegian University of Science and Technology (from the Strategic Area Materials program).

The main objective of this work was fabrication and characterization of tunable Y-junction laser diodes for trace-gas sensing applications. The successful realization of the Y-junction laser diodes benefited from the optimization of laser growth and fabrication process. The results of optimization of carrier concentration in the doped cladding layers are presented in the first paper in chapter 5. An overview of the laser fabrication and testing is depicted in chapter 3 and chapter 4. The results of process optimization for fabrication of GaSb-based laser diodes are presented in the next three papers in chapter 5. Output performance of the tunable Y-junction lasers is presented in the last paper of chapter 5.

Acknowledgements

My sincere gratitude goes to my supervisor, Professor Bjørn-Ove Fimland, for giving me the opportunity to pursue my adventure in science and become a PhD in the process. I greatly appreciate his valuable guidance and suggestions and his diligent work on editing and revising manuscripts as well as this thesis. Moreover, his patience and encouragement gave me new hope when I felt lost and helped me to complete the PhD. I am also thankful to my co-supervisor, Professor Astrid Aksnes for her assistance during the thesis writing process.

I feel honored to have worked with talented people in my research group. Dr. Magnus Breivik mentored me every single step of fabrication and characterization of laser diodes and I learned a lot from his expertise. He is the one who laid the foundation for this work. Dr. Saroj Kumar Patra supplied all MBE materials I needed for my researches. Without him, all of my works could not be accomplished. Fruitful discussions with Magnus and Saroj always provided me with valuable perspectives to improve my work. I hope both of them succeed in their careers. I also enjoyed supervising and collaborating with two master students, Olav Myrvang and Kjetil Haddeland. Their enthusiasm and efforts brought positive energy for my PhD journey. I would also like to thank Renato, Geir, and Eva at Intopto for their discussions relating to fabricating and characterizing laser diodes.

NTNU Nanolab was my second "office" where I spent most of my time to fabricate laser diodes. This work could not be accomplished without the assistance of Nanolab staff (Mark, Kay, Espen, Ida, Ken Roger, Trine). They worked tirelessly to keep the equipment up and running, so I could to do my job successfully.

On my PhD journey, it was a pleasure time having numerous lunch, coffee and beer times with my officemates (Lukas and Matija) and IES colleagues (Dheeraj, Mazid, Gaurav, Tron Arne, Dingding, Andreas, Jonas, Armend…). They gave me valuable insights, both on scientific and social issues, through our discussions. Special thanks to my Vietnamese friends in Trondheim, Oslo and Horten for dinner, party and karaoke times, that made me feel like home.

Last, but not least, I would like to thank my family for all support during my PhD. My parents, who devoted their whole lives to me and my brother, would be very proud of me for getting a PhD. To my wife and my son, you are the lights of my life, always standing by my side no matter what and making me a better man and a better father. This PhD degree is for you.

List of abbreviations

Notation	Description
1-D	one-dimensional
3-D	three-dimensional
AFM	Atomic Force Microscopy
AR	anti-reflection
BCB	benzocyclobutene
BH	buried heterostructure
COMD	catastrophic optical mirror damage
cw	continuous wave
DBR	distributed Bragg-reflector
DFB	distributed feedback
DIW	deionized water
DLTS	deep level transient spectroscopy
EBR	edge bead removal
ERIM	effective refractive index method
FP	Fabry-Perot
FSR	free spectral range
FTIR	Fourier transform infrared
FT-PL	Fourier Transform PhotoLuminescence
FWHM	full width at half maximum
GG	gain-guided
HICRW	high-index-contrast ridge-waveguide
HR	high reflection
ICL	interband cascade lasers
ICP-RIE	inductively-coupled plasma reactive ion etching
IG	index-guided
IPA	isopropanol
IR	infrared

LASER	Light Amplification by the Stimulated Emission Radiation
MBE	molecular beam epitaxy
MQW	multiple quantum well
MZ	Mach-Zehnder
NA	numerical aperture
PECVD	plasma-enhanced chemical vapor deposition
PR	photoresist
QCL	quantum cascade lasers
QIG	quasi-index-guided
QW	quantum well
QWOT	quarter-wavelength optical thickness
RHEED	reflection high-energy electron diffraction
RIE	reactive ion etching
RT	room temperature
RTP	rapid thermal processing
RW	ridge-waveguide
SCL	separate confinement layer
SIMS	secondary ion mass spectrometry
SMSR	side mode suppression ratio
SRH	Shockley-Read-Hall
TDLAS	tunable diode laser absorption spectroscopy
TE	transverse electric
TEC	thermoelectric cooler
TLM	transfer length method
TM	transverse magnetic
UV	ultraviolet
VBO	valence band offset
VCSEL	vertical cavity surface-emitting lasers
XRD	X-ray diffraction
ZB	zinc-blende

List of Contents

Chapter 1

INTRODUCTION

Industrial development has raised many problems for human life, amongst them hazardous gas risks. Many toxic gases, such as phosphine, silane, ozone and chlorine are dangerous to health in concentrations as low as 1 ppm [1]. Therefore, systems to monitor and warn of dangerous emissions of toxic gases are required. Laser spectroscopy using laser diodes is a highly suitable method due to its high sensitivity and specificity. Laser diodes operating in the mid-infrared (mid-IR) wavelength region of 2 – 5 µm are desirable for laser spectroscopy since a lot of polluting gases and combustion products have absorption lines in this regime, see Fig. 1.1, such as NH_3 (2.1 µm), HF (2.5 µm), CH_4 (2.35 µm and 3.3 µm), HCHO (3.5 µm), HCl (3.5 µm), N_2O (3.9 µm and 4.5 µm), SO_2 (4 µm), CO_2 (4.25 µm), and CO (2.3 µm and 4.6 µm) [2]. Gas detection, however, is not the only application that laser diodes are suitable for in this wavelength regime. Other applications are laser surgery, fiber amplifier pumping, free space communications and military countermeasures.

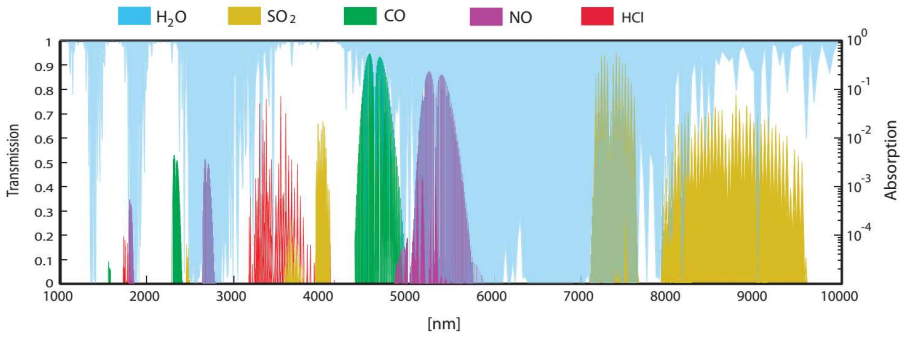

Figure 1.1: Absorption bands of gases common in combustion control applications [3] (© 2011 SPIE)

First introduced in the mid-1960s [4], tunable diode-laser absorption spectroscopy (TDLAS) is now the most common technique for quantitative measurement of trace gases due to its high compactness and ability to detect accurately predefined gases even at low gas concentrations on the order of ppbv [4]. The working principle of TDLAS relies on the absorption of gas species of interest at one of their specific absorption wavelengths. By tuning the wavelength of the laser source across the absorption line, the gas concentration N can be found by measuring the attenuation of the laser beam intensity given by Beer's law

$$I(\omega) = I_0(\omega)\, e^{-\sigma(\omega)LN} \qquad (1.1)$$

where ω is the laser frequency, I_0 is the transmitted intensity in the absence of the absorbing gas, L is the optical path length, $\sigma(\omega)$ is the absorption coefficient and N is the concentration of the absorbing gas in molecules per unit volume.

A working TDLAS system consists of a laser diode, a sample cell containing the gas of interest, a detector and a setup for signal processing. Laser diodes as light sources for TDLAS need to fulfill the following conditions: single-frequency emission with a side mode suppression ratio (SMSR) better than 20 dB, emission power on the order of 1 mW, and room temperature (RT) operation in continuous wave (cw) mode [5].

Among material systems that can be used for mid-IR lasers, the III-V semiconductors are best suited for practical devices operating in cw mode at RT [6]. Especially, the so-called III-arsenide-antimonides, III-AsSb, are highly suited materials to develop mid-IR lasers and other devices such as hyper-frequency transistors, imaging IR photodetectors, IR-THz lasers, and high frequency solar cells. The properties that make III-AsSb compounds unique among III-V semiconductors are: large variety of band alignment, very large band offsets, in particular, in the conduction band, large bandgap range from 0.17 eV up to 2.17 eV of III-AsSb multinary materials lattice-matched to GaSb, and high carrier mobilities.

The mid-IR III-V semiconductor laser diodes are usually classified into three categories: (1) diode lasers with type I active region, (2) interband cascade lasers (ICL) with both type-I and type-II (conventional type-II and type-II broken gap) active regions, and (3) intersubband quantum cascade lasers (QCL). The working principle of these types of laser structures is illustrated in Fig. 1.2 via their band diagrams. The performance data of the representative devices for these three categories of mid-IR laser diodes [7-31] are presented in Fig. 1.3.

In type-I diode lasers, the electrons and holes are confined in the same material, typically using quantum wells (QW) separated by barriers, which are usually thick enough to prevent the coupling between the wells. First growth by Kobayashi et al. [32] in 1980, the type-I GaInAsSb/AlGaAsSb laser diodes exhibit excellent performance in the 2 – 2.5 µm wavelength range such as low threshold current density, typically below 100 A/cm^2, cw operation up to 124 ^{o}C [33], and output power up to 1.6 W [34]. For $\lambda > 2.5$ µm, the valence band offset (VBO) becomes small and thus leading to the thermionic excitation of holes from the quantum well into the barrier where they recombine [35], leading to a loss of lasing performance. Several approaches have been studied to overcome this issue, such as (1) increasing the VBO by exploiting highly compressive strained QWs [11] or using high Al-content in the barrier [6], or (2) adding nitrogen into InGaAsSb QW to extend the wavelength while keeping the hole confinement barrier unchanged [35]. These approaches, however, could not completely solve the problem. In 2005, Grau et al. [36] introduced the quinternary AlGaInAsSb as the barrier layer which opened a new path for laser structure engineering. Using the quinternary AlGaInAsSb barrier, the type-I laser diodes have been demonstrated to operate at RT up to 3.44 µm in cw mode [17] and up to 3.73 µm in pulsed mode [37]. However, the type-I GaInAsSb/AlGa(In)AsSb material system has probably reached its limit due to the significant Auger recombination at long wavelengths.

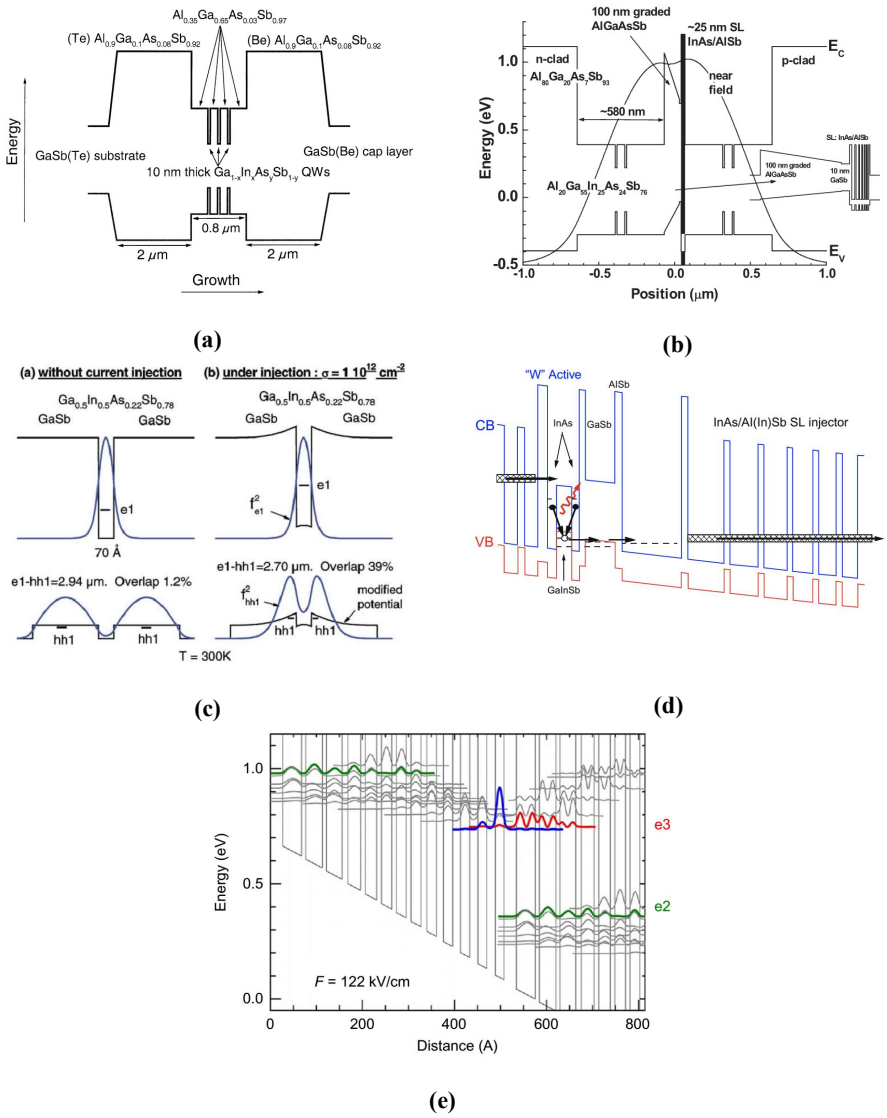

Figure 1.2: Schematic band diagram of (a) type-I GaInAsSb/AlGaAsSb diode laser under flat band condition [38] (© 2003 Académie des sciences), (b) type-I ICL under flat band condition [39] (© 2013 AIP Publishing LLC), (c) type-II ICL with carrier probability density of presence at equilibrium and under carrier injection [38] (© 2003 Académie des sciences), (d) single stage of the type-II broken gap ICL structure [40] (© 2009 IOP Publishing and Deutsche Physikalische Gesellschaft), and (e) conduction band of a typical active region of an InAs/AlSb QCL, the solid curves represent the moduli squared of the relevant electron wave functions [6] (© 2012 Elsevier Inc.).

At longer wavelengths, it is difficult for diode lasers to reach the threshold condition due to lower gain. First proposed by Yang [41], ICLs using a cascade scheme with multiple active regions connected in series employ electron recycling to enhance the optical gain. By combining the advantages of the electron recycling of the cascade injection scheme and the high optical gain of type-I QWs, the results obtained by Belenky's and Gupta's groups [27, 29, 31] show the significant improvement of the type-I ICLs in terms of output power and efficiency. Research on this type of laser diode is still ongoing with the expectation of achieving high-performance laser diodes at wavelengths beyond 3 μm. Meanwhile, in the ICLs with type-II active regions, electron-hole recombination occurs due to the interband transition between electrons localized in one layer (GaInAsSb QW) and holes localized in another layer (GaSb barrier), as illustrated in Fig. 1.2 (c). The weak overlap of electron and hole wavefunctions in normal type-II ICLs can be overcome by employing the type-II broken gap ("W" shape) band alignment shown in Fig. 1.2 (d). In this type of laser diodes, the effect of Auger recombination is strongly suppressed with the RT Auger coefficients as small as 3-5 × 10^{-28} cm^6/s for devices emitting at wavelengths from 2.9 to 4.1 μm [42]. By changing the thickness of the QWs, the type-II broken gap ICLs can cover a wide spectral range up to 10.4 μm [43], and especially be well-suited for the 3-4 μm wavelength regime.

In contrast to the type-I laser diodes and the ICLs, the photon emission in QCLs is achieved by the transition of electrons between subbands in the conduction band of a multiple quantum well (MQW) structure, which means the conduction band electron is the only charge carrier. Undergoing multiple lasing transitions in multiple cascades of QWs, typically 30 stages in the active region [6], each electron can create many photons thus making possible devices of very high output power (up to 5.1W in cw mode) and high wall-plug efficiency (up to 21 % at RT in cw mode) [18, 44]. In QCLs, the intersubband transition frees the devices from the effects of Auger recombination, thus allowing this type of laser diodes operating at long wavelengths up to 4.9 μm at RT in cw mode [18]. Another advantage of the QCLs is that the photon emission is not due to the material bandgap and the emitting wavelength can be adjusted by changing the thickness of the active layers. This also allows the QCLs to be grown on well-developed substrates such as InP and GaAs. The limitation of the QCLs is that the optical gain is quite low due to short upper state lifetime of the electrons resulting in high threshold current density, typically 1000 A/cm^2.

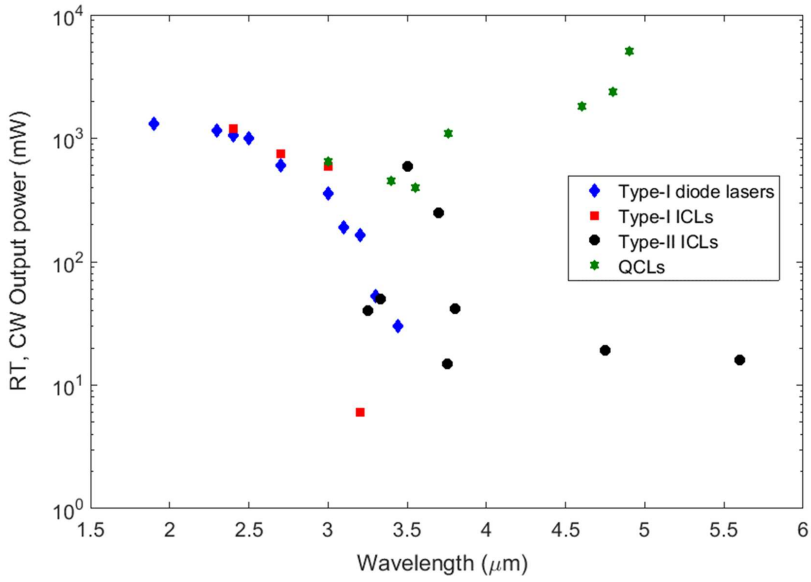

(a)

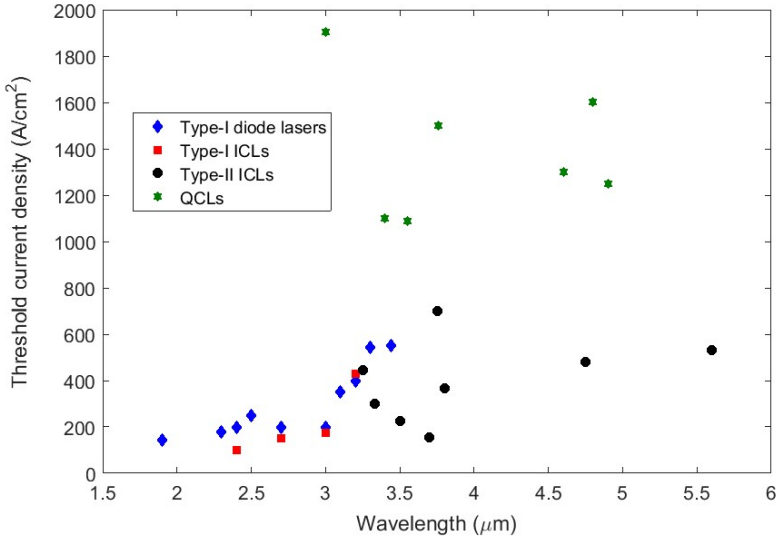

(b)

Figure 1.3: Performance data of type-I diode lasers [8-11, 15-17, 19], type-I ICLs [27-29, 31], type-II ICLs [12, 21-24, 30], and QCLs [7, 13, 14, 18, 20, 25, 26] emitting in the wavelength region of 2 – 5 μm: (a) output power and (b) threshold current density, measured at RT in cw mode.

Beside the excellent works in growth of laser materials to allow operation of the devices at RT in cw mode as mentioned above, the processing of laser materials is also important for realization of tunable laser diodes. Single-mode behavior and wavelength tunability of laser diodes can be obtained by utilizing special structure designs such as distributed Bragg-reflector (DBR), distributed feedback (DFB), vertical cavity surface-emitting lasers (VCSELs) and interferometric lasers in which case the latter three structures are the most interesting candidates. Mode selection in DFB lasers is based on the index modulation mechanism. The index grating is designed to reflect only a narrow band of wavelength, thus allowing single longitudinal mode operation. DFB lasers usually exhibit single mode behavior with a SMSR of more than 30 dB [45-47]. However, the precise periodic structure requires complicated fabrication steps such as electron beam lithography, resulting in high cost and low yield. On the other hand, single longitudinal mode behavior of VCSELs is easy to obtain due to the nature of the structure (very short cavity length and thus large longitudinal mode spacing). VCSELs also offer numerous advantages compared to the conventional edge-emitting lasers, such as low power consumption, high beam quality (low beam divergence, circular beam profile) and wafer-scale fabrication. However, to achieve lasing, a complex growth procedure is required to perfectly match the properties of the active regions to those of the cavity.

The main focus of this work is on fabricating type-I GaSb-based tunable laser diodes using Y-junction interferometric structure. For laser diodes working in the wavelength regime of 2 – 3 μm, type-I GaSb-based laser diode is a promising candidate due to the high optical gain (low threshold current density), the simplicity of growth design and the easy approach to cw operation at RT. For tunable lasers, the Y-junction structure considered as "half of a Mach-Zehnder interferometer" has been studied by Fattah and Wang [48, 49] and later developed by Hildebrand's [50-53] and Kuznetsov's group [54, 55] focusing on optical communication applications. Recently, related structures such as full Mach-Zehnder interferometer [56, 57], V-coupled cavity [58] and modulated grating Y branch [59] have been developed for gas sensing and optical communication applications. In our group, the Y-junction lasers have been studied for several years [60, 61]. The merit of this approach is the fabrication simplicity and the ability for realization of tunable laser diodes.

Our work:

Optimization of laser growth and laser processing is crucial for high-performance tunable laser diodes. Even though the laser fabrication procedure has been studied in our group for several years, there are still many challenges and still fabrication steps to be optimized. The main goal of this work is optimizing the growth and processing of type-I GaSb-based laser diodes in order to develop tunable Y-junction lasers for trace-gas sensing applications.

Carrier concentration in the doped cladding layers play a key role in the electrical properties of the laser diodes. Thus, optimization of carrier concentration is required with regards to dopant density. In section 5.1, the carrier concentration and Hall mobility of both n- and p-doped AlGaAsSb cladding layers for different dopant density values have been determined using Hall effect measurements with high accuracy.

A large part of this work has focused on the processing of the laser diodes and the results are presented in chapter 3, chapter 4 and from section 5.2 to 5.4. To confine light in a high loss waveguide such as the Y-junction structure (due to bend structure), a well-defined ridge waveguide structure is needed as simulated in section 5.2. To create such structures, the optimal waveguide profile obtained from photolithography processes and precise control of etching processes using *in situ* reflectance monitored inductively-coupled plasma reactive ion etching (ICP-RIE) has been demonstrated, see chapter 3 and section 5.2. For high performance laser diodes, low ohmic contact resistance between metal contacts and laser materials is highly desirable to enhance the carrier injection and minimize the heat generation in the contact region, thus reducing the heat inside the laser structure. To obtain such good ohmic contacts, it is essential to remove the GaSb native oxide prior to metallization. In section 5.3, different plasma-assisted oxide removal techniques have been studied in comparison with the conventional chemical methods. As an alternative to the conventional Au-based contact, the metallization systems based on aluminum with good ohmic contact and high reliability have been demonstrated for use in GaSb-based diode lasers in section 5.4. Another method to improve the performance of the GaSb-based laser diodes is applying optical coatings on the laser facets. In chapter 4, the reflectance spectra of different optical coatings are simulated for material selection and reflectance optimization. The optical coatings are then deposited and their reflectance spectra are measured and compared to the simulation results. Finally, different optical coatings are applied on laser facets to study the effect of optical coatings on the performance of the GaSb-based laser diodes.

Tunable Y-junction laser diodes have been successfully fabricated in this work. The performance of the Y-junction lasers of different configurations at RT in cw mode has been characterized in section 5.5. As the bend radius of the Y-junction structure increases, the optical loss reduces and the tuning range increases. Using a large bend radius of 1000 µm and a length difference of 20 µm between the two cavities, widely continuous tuning ranges up to 50 nm with the SMSR > 23 dB can be achieved by adjusting the injected current ratio between different sections of the Y-junction lasers. The promising results show the applicability of the Y-junction lasers for trace-gas sensing applications.

The outline of this thesis is as follow: In chapter 2, the basic theories of semiconductor laser diodes and Y-junction laser in particular are described, in addition to the mode confinement in the laser structure in order to obtain single mode operation. In chapter 3, the fabrication of GaSb-based laser diodes is presented from the starting point of GaSb substrate to the final characterized devices. The use of optical reflectance coatings to improve the laser performance is presented in chapter 4 from theory to the simulation of reflectance spectra and to the experimental results. The results obtained from the optimization of performance of the GaSb-based laser diodes and tunable Y-junction lasers, in particular, are presented in form of scientific papers in chapter 5. Finally, summary and future outlook of this work are presented in chapter 6.

Chapter 2

LASER THEORY

Optical physics is the study of generation, manipulation and control of electromagnetic radiation. The quantum of electromagnetic radiation is a photon. The emission of a photon results from the transition of an electron from a high-energy state to a low energy state. This transition can be random or stimulated. Random or spontaneous emission of photons shows variation in phase and polarization state of the emitted photons. This radiation is non-coherent, which contributes significantly to the noise characteristics of the optical devices. On the other hand, stimulated emission induced by another photon creates a new photon sharing the same properties as the incident initiator. This coherent radiation is the principle of LASER (Light Amplification by the Stimulated Emission Radiation) devices.

In general, the operation of a laser device has to satisfy two criteria: gain condition and phase condition. The first condition requires that the power gain exceeds the loss. To achieve this, the medium must be able to amplify the light transmitted through it by the stimulated emission process. In order to create coherent light, the rate of stimulated emission needs to far exceed the rate of absorption and spontaneous emission, requiring that the population of electrons in the higher energy state must be significantly larger than that of electrons in the lower energy state. This phenomenon known as the population inversion can be achieved by the excitation process called "pumping". The second lasing condition requires that the phase shift of light travelling back and forth in the resonator must be a multiple of 2π for a single round trip. In satisfying this condition, the light creates a standing wave inside the cavity allowing the mode to self-reproduce.

A semiconductor diode laser is a two-level system where the electron transition takes place between the conduction band and the valence band. The excitation of electrons from the valence band to the conduction band can be achieved by electrical or optical pumping. The later radiative recombination of electrons in the conduction band and holes in the valence band provides the optical gain inside the laser structure which is usually a p-i-n double-heterostructure as shown in Fig. 2.1. The condition of population inversion is satisfied if the inequality known as the Bernard – Duraffourg condition is fulfilled [62] :

$$F_n - F_p \geq hf = \frac{hc}{\lambda} \geq E_g \qquad (2.1)$$

where f is the frequency, λ is the wavelength, h is Planck's constant, c is the speed of light, E_g is the band gap of the semiconductor, and F_n and F_p are the quasi-Fermi levels of the conduction and valence bands, respectively. At $F_n - F_p = hf$, the transparency condition is fulfilled, allowing the transition from absorption to gain. It is worth noting that the separation of the

quasi-Fermi levels, $F_n - F_p$, becomes sufficient if the p- and n-layers are heavily doped to force the quasi-Fermi levels into the energy bands of the undoped layer, depicted in Fig. 2.1. In fulfilling the Bernard-Duraffourg condition, the semiconductor laser diode can be considered as a gain medium. However, the lasing operation requires certain optical feedback mechanisms for the onset of laser oscillation.

In this chapter, the operation of the semiconductor diode lasers with the simplest laser structure, the Fabry-Perot laser, and the tunable lasers with Y-junction structure are presented. In addition, the laser modes and the mode confinement inside the laser structure to achieve single mode behavior are discussed.

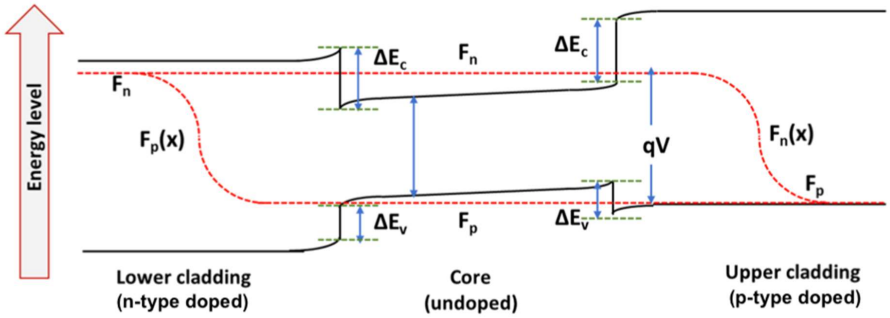

Figure 2.1: Energy band diagram of the double-heterostructure p-i-n junction under forward-biased regime ($qV > 0$, where q is the charge and V is the applied voltage) [63]. The valence band offset (ΔE_v) and the conduction band offset (ΔE_c) are important for the electrical confinement in this structure.

2.1. Fabry-Perot lasers

As discussed above, optical feedback is necessary to sustain the laser oscillation. For semiconductor laser diodes, the simplest laser structure is Fabry-Perot (FP) laser as illustrated in Fig. 2.2, which is also the most common type of diode lasers [64]. In this section, some of the main properties of this laser are discussed which are based on the theory presented in Buus et al. [62]. The optical field travelling along the cavity length in the z direction can be expressed as

$$\boldsymbol{E} = \boldsymbol{E}_0 \exp(i\beta^* z) \qquad (2.2)$$

where E_0 is the time-dependent amplitude and β^* is the complex propagation constant given in the form

$$\beta^* = k_0 n_{eff} + i\,\frac{\alpha}{2} \qquad (2.3)$$

where $k_0 = 2\pi/\lambda$, n_{eff} is the effective refractive index and α is the net absorption coefficient ($\alpha > 0$ for the medium where light is absorbed and $\alpha < 0$ for the medium where light can be amplified). The effective refractive index is related to the carrier density and the amount of light in the active region. In the gain medium such as semiconductor laser materials, the net absorption coefficient is given in the form

$$\alpha = -g = -\Gamma g_a + \alpha_i \qquad (2.4)$$

where g is the net gain coefficient, g_a is the gain of the active medium, Γ is the confinement factor and α_i is the internal loss. The confinement factor Γ defines how strongly the light is confined inside the active region, which is discussed in detail in section 2.2.

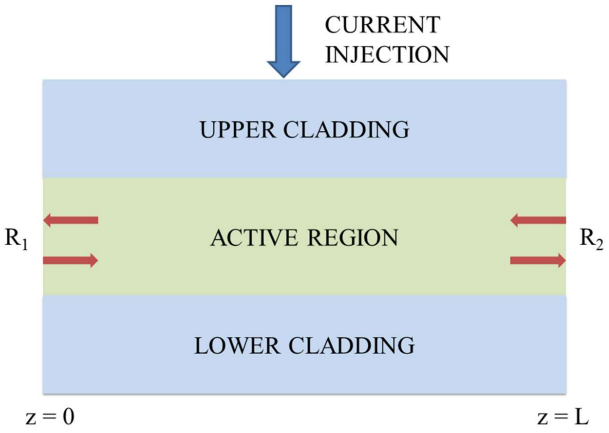

Figure 2.2: Schematic illustration of a FP semiconductor laser diode with a length L. Induced by the injected current, photons are generated and are confined inside the active region, travelling back and forth between two mirrors (or facets) with the reflectivity of R_1 and R_2.

As mentioned above, the mode can self-reproduce after each round trip if the phase shift is a multiple of 2π. If R_1 and R_2 are the reflectivities of the laser facets and the net change in the amplitude after each round trip is set to unity, Eq. (2.2) leads to

$$(R_1 R_2)^{1/2} \exp(-2i\beta^* L) = 1 \qquad (2.5)$$

Equating the real and imaginary parts of Eq. (2.5), we have

$$(R_1 R_2)^{1/2} \exp(-\alpha L) = 1 \qquad (2.6)$$

$$\sin(2n_{eff} k_0 L) = 0 \qquad (2.7)$$

At the threshold condition where the gain equals the total losses α_t (the net coefficient equals zero), we obtain

$$\Gamma g_a = \alpha_t = \alpha_m + \alpha_i \tag{2.8}$$

where

$$\alpha_m = \frac{1}{2L} ln\left(\frac{1}{R_1 R_2}\right) \tag{2.9}$$

is the mirror loss which defines how much light is escaping from the FP cavity due to the finite facet reflection.

From Eq. (2.7) one can determine the lasing wavelengths of the longitudinal modes

$$\lambda_N = \frac{2n_{eff}(\lambda_N)L}{N} \tag{2.10}$$

where λ_N is the wavelength of the N^{th} longitudinal mode of an FP cavity (N is an integer). The longitudinal mode spacing in the comb-mode spectrum can be obtained from Eq. (2.10). However, it is worth noting that in semiconductor lasers the effective refractive index varies with the wavelength due to the dispersion in the material and waveguide. Therefore, the term "group refractive index" of the dispersive semiconductor material is introduced

$$n_{g,eff}(\lambda_N) = n_{eff}(\lambda_N) - \lambda_N \frac{\partial n_{eff}(\lambda_N)}{\partial \lambda} \tag{2.11}$$

Thus, the longitudinal mode spacing which is called the free spectral range (FSR) is given by

$$\Delta\lambda_m = \lambda_N - \lambda_{N+1} \cong \frac{\lambda_N^2}{2n_{g,eff}L} \tag{2.12}$$

Generally, it seems that the number of longitudinal modes becomes very large when N increases. However, in practice, the number of longitudinal modes is limited by the material gain spectrum as depicted in Fig. 2.3. Typically, with the mode spacing being below 1 nm, the gain curve of several tens of nanometers width covers several tens of longitudinal modes. The semiconductor laser diodes have, however, a unique property in that the longitudinal-mode wavelengths and their separation vary with the external pumping level, because the refractive index of the gain medium is dependent on the density of the charge carriers. This is the principle of tunable laser diodes which is discussed in section 2.3.

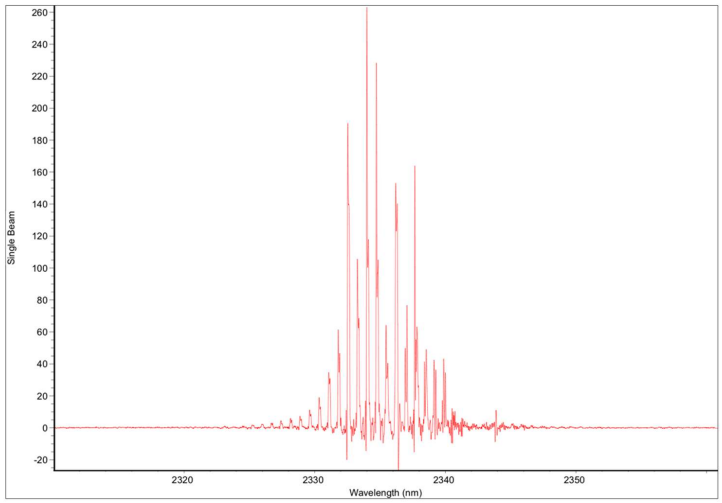

Figure 2.3: Lasing spectrum of a 2 mm long and 25 µm wide FP laser based on $Ga_{0.67}In_{0.33}As_{0.1}Sb_{0.9}/Al_{0.9}Ga_{0.1}As_{0.06}Sb_{0.94}$ active/cladding material (details of the laser structure are discussed in chapter 3). The gain curve is nearly Gaussian in shape.

2.2. Mode confinement in laser structures

A laser mode is the electromagnetic field distribution across the laser beam which has a stable and well-defined form. It must satisfy all the boundary conditions imposed by the laser structure. The confinement of the laser modes in the laser structure is important to achieve high performance laser characteristics. Semiconductor laser diodes are often desired to emit light predominantly in a single mode, especially for gas sensing and communication applications.

In heterostructure semiconductor lasers, the optical field is usually confined by the index guiding mechanism for which the refractive index discontinuity between layers confines modes through the total internal reflection, as shown in Fig. 2.4. The mode confinement strength is usually characterized by the confinement factor Γ which is defined by the ratio of the mode power in the active layer to the total mode power. The confinement factor in two-dimensional structures can be approximated by the product of the confinement factor in the transverse direction Γ_T and in the lateral direction Γ_L

$$\Gamma \approx \Gamma_T \Gamma_L \qquad (2.13)$$

The confinement factor plays an important role for semiconductor laser diodes which accounts for the mode energy confined within the active region being available for the photon-electron interaction. A lower confinement factor will result in a lower rate of stimulated emission and a lower modal gain. For high loss waveguides such as S-bend, Y- junction and Mach-Zehnder

structures, this factor is even more critical. In this section the confinement of laser modes in both transverse and lateral directions is discussed to aim for achieving single mode operation of the laser devices.

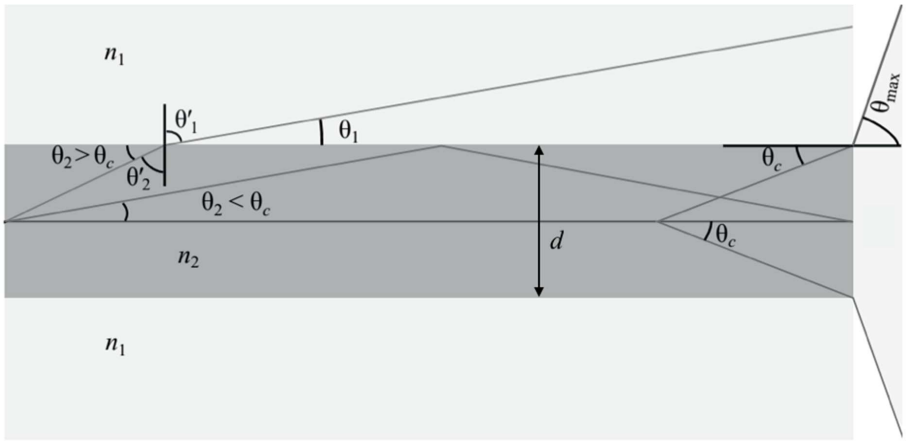

Figure 2.4: Light reflection in a three layer slab waveguide [61], where d is the thickness of the active region (dark color), n_1 and n_2 are the refractive indices of the cladding layers and the active region, respectively ($n_2 > n_1$). Total internal reflection occurs when the angle θ_2 of incident light is less than the critical angle θ_c where $\cos \theta_c = n_1/n_2$.

2.2.1. Transverse laser modes

In semiconductor laser diodes, the mode confinement in the transverse direction can be easily obtained by growth of a double-heterostructure. The thicknesses and refractive indices of the active region and the cladding layers can be controlled to provide single transverse mode operation. For symmetric dielectric slab waveguides, as shown in Fig. 2.4, to support only the lowest-order fundamental mode, the thickness, d, of the active region needs to satisfy the condition [62, 65]

$$d < \frac{\lambda}{2}(n_2^2 - n_1^2)^{-1/2} \qquad (2.14)$$

The confinement factor in transverse direction can be approximated [65] by

$$\Gamma_T \cong \frac{D^2}{2 + D^2} \qquad (2.15)$$

where

$$D = k_0(n_2^2 - n_1^2)^{\frac{1}{2}}d \qquad (2.16)$$

is the normalized thickness. It is found that the confinement factor for the fundamental transverse electric (TE) mode is larger than that of the transverse magnetic (TM) mode [62, 65]. Therefore, the TE mode exhibits higher modal gain that makes it favorable in operation of semiconductor laser diodes.

For the GaInAsSb/AlGaAsSb laser diode emitting in the range of 2 – 3 μm, a typical example for the thickness of the active region at 2.33 μm wavelength is $d < 0.644$ μm given by Eq. 2.14. Here, the refractive indices of GaInAsSb and AlGaAsSb are given by [66, 67]. For all the laser structures grown in this project, the thickness of the active region is 366 nm, allowing achievement of single mode behavior in the transverse direction. It is also demonstrated by Hosoda et al. [68] that a decrease in the width of the active region from 1470 nm to 470 nm by adjusting the thickness of the separate confinement layer (SCL) can lead to improvement of laser characteristics in term of output power, differential gain, internal quantum efficiency, and quantum well optical confinement factors.

2.2.2. Lateral laser modes

In contrast to transverse modes, the mode confinement in the lateral direction is more difficult to obtain. In principle, it can be performed by creating a lateral dielectric waveguide structure, which requires etching processes and even multiple epitaxial steps in some cases. Based on the index guiding strength, the lateral waveguide structure is classified as index-guided (IG) (strong index guiding) or quasi-index-guided (QIG) (weak index guiding) structure. Examples of IG structure are buried heterostructure (BH) [69, 70] and high-index-contrast ridge-waveguide (HICRW) [71-73]. Meanwhile, rib waveguide [74], channeled-substrate planar waveguide [75], and ridge-waveguide (RW) devices are examples of QIG structures in which case the RW structure is the most popular choice due to simple fabrication processing. In addition to the index guiding mechanism, the lateral confinement of the field can also be achieved by gain-guided (GG) mechanism. In GG devices, the optical gain changes along the lateral direction due to non-uniform carrier diffusion that leads to the confinement of the lateral modes. Although the fabrication of the GG devices is simple, this guiding mechanism is not of interest because of less stable waveguiding and multimode behavior. Illustration of the IG, QIG and GG structures and the comparison of the lateral field confinement in these structures are shown in Fig. 2.5.

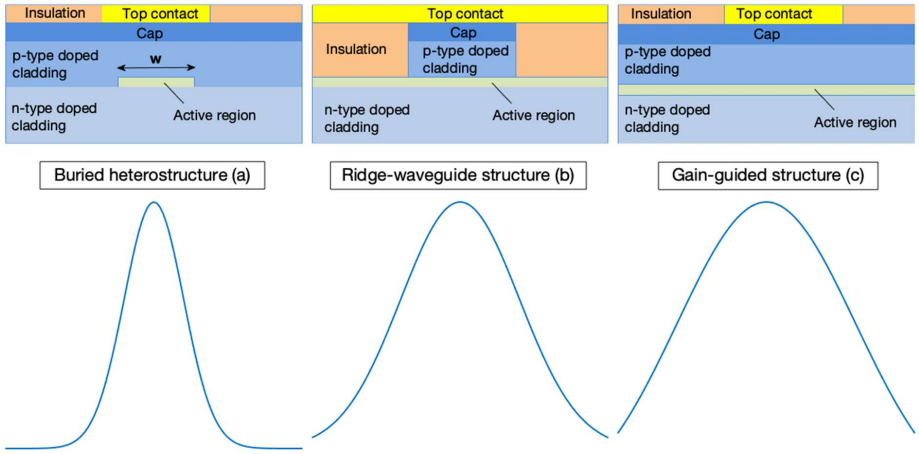

Figure 2.5: Three types of structures for lateral mode confinement and the approximated lateral field distribution in these structures.

In the case of the IG structure, only the lowest-order lateral mode is supported if the width of the active region, w shown in Fig. 2.5 (a), satisfies the condition [65]

$$w \leq \frac{\lambda}{\left(8 n_{eff} \Delta n_L\right)^{1/2}} \tag{2.17}$$

where Δn_L is the lateral index step. The confinement factor can be approximated as

$$\Gamma_L \cong \frac{W^2}{2 + W^2} \tag{2.18}$$

where W is the normalized waveguide width given by

$$W = k_0 w \left(n_{eff}^2 - n_{out}^2\right)^{\frac{1}{2}} \tag{2.19}$$

where n_{out} is the refractive index of the medium outside the active region in the lateral direction. Although the modes are well-confined in the IG structures, their fabrication process is complicated and the devices may suffer from reliability problems. For example, the fabrication procedure of the BH structure involves multiple epitaxial steps interrupted by etching processes to build the active strip. Or in the case of the HICRW structure, it requires etching through the active region which can introduce a lot of defects at the sidewalls of the active region. Creating the active strip by multiple epitaxial steps interrupted by etching processes or etching through the active region can also lead to the diffusion of impurities from outside regions into the active layer during the processing [76], which can cause critical problems for the long-term operation of the semiconductor laser diodes.

The RW laser structure as shown in Fig. 2.5 (b) and Fig. 2.6 (a) is much easier to fabricate, involving only one epitaxial step and one etching step. This waveguide structure can be classified as pure GG or pure IG or part GG-part IG depending on the etching. It will be pure GG if the etching is shallow, whereas pure IG if the etching is through the active region. The RW structure is formed by etching the upper cladding layer (and the active layer in case of pure IG) in region B. The waveguide sidewalls and the surfaces in region B are then covered by an insulation layer with the refractive index of n_0. The index contrast between region A and region B to provide the lateral waveguiding can be calculated using the effective refractive index method (ERIM) [77, 78], depicted in Fig. 2.6 (b) and (c).

For a four-layer slab waveguide such as region B in Fig. 2.6 (a), the effective refractive index of this region, n^B_{eff}, is given by

$$n^B_{eff} = \frac{\beta_B}{k_0} = \frac{\sqrt{k_0^2 n_2^2 - \gamma_B^2}}{k_0} \tag{2.20}$$

where β_B is the propagation constant in region B, n_2 is the refractive index of the active region and γ_B can be calculated from the mode equation for the TE mode as following [78]

$$d \times \gamma_B = tan^{-1}\sqrt{\frac{k_0^2(n_2^2 - n_1^2)}{\gamma_B^2} - 1} + tan^{-1}\left\{\eta\sqrt{\frac{k_0^2(n_2^2 - n_0^2)}{\gamma_B^2} - 1}\right\} + m\pi \tag{2.21}$$

(m = 0, 1, 2, …)

where d is the thickness of the active region, n_1 and n_0 are the refractive indices of the cladding layer and the insulation layer, respectively, and

$$\eta = \frac{\sigma_2}{\sigma_4} \times \frac{1+T}{1-T} \tag{2.22}$$

$$T = \frac{\sigma_4 - \sigma_2}{\sigma_4 + \sigma_2}.\exp(-2\sigma_2.t) \tag{2.23}$$

$$\sigma_2 = \sqrt{k_0^2(n_2^2 - n_1^2) - \gamma_B^2} \tag{2.24}$$

$$\sigma_4 = \sqrt{k_0^2(n_2^2 - n_0^2) - \gamma_B^2} \tag{2.25}$$

where t is the remaining thickness of the upper cladding layer in region B. Without etching, region A becomes a three-layer slab waveguide whose effective refractive index, n^A_{eff}, can also be determined from these above equations by replacing n_0 with n_1 in Eq. 2.21 and Eq. 2.25. Fig. 2.7 shows the dependence of the effective index contrast between region A and B ($\Delta n_{eff} = n^A_{eff} - n^B_{eff}$) on the remaining thickness t of the upper cladding layer in region B for a given layer structure and wavelength.

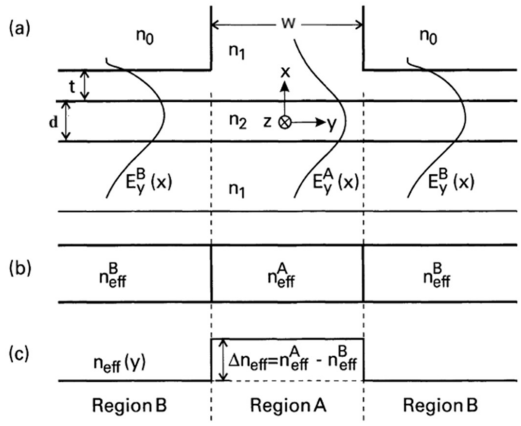

Figure 2.6: (a) Ridge-waveguide laser structure with the waveguide width w, the thickness d of the active region, and the remaining thickness t of the upper cladding layer in region B. Here, n_2, n_1, and n_0 are the refractive indices of the active region, the cladding layers and the insulation layer, respectively. (b) Regions A and B are represented in terms of their effective refractive indices. (c) The lateral index profile of the ridge-waveguide structure with the effective refractive index step Δn_{eff} to provide the lateral waveguiding [62]. (© 2005 Wiley-IEEE Press)

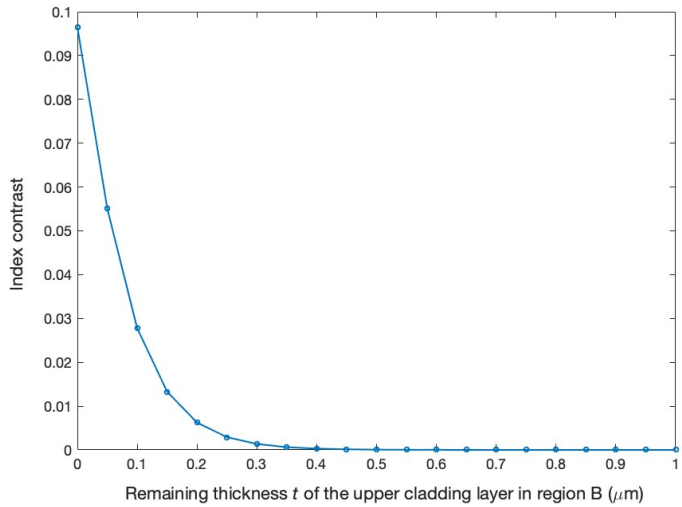

Figure 2.7: The dependence of the effective refractive index contrast Δn_{eff} between region A and B on the remaining thickness t of the upper cladding layer in region B, calculated by ERIM. The ERIM simulation is applied for $\lambda = 2.33$ µm, $n_2 = n_{core} = 3.523$, $n_1 = n_{cladding} = 3.25$, $n_0 = n_{insulation} = 1.5$, and $d = 0.366$ µm. In this case, the RW structure becomes pure IG if the etching is shallow ($t > 0.4$ µm).

The maximum waveguide width, w_{max}, for single lateral mode operation is given by [78]

$$w_{max} = \frac{\lambda_0}{2n_2\sqrt{2\Delta n_{eff}}} \qquad (2.26)$$

For guiding light in a straight waveguide, the effective refractive index contrast Δn_{eff} can be as small as 0.01, as shown in Breivik's simulation [61]. For the numerical example in Fig. 2.7, typical value of w_{max} in this case is 2.3 µm. Fabricating a narrow RW structure is also essential for reducing the number of longitudinal modes and enhancing the dominant longitudinal mode, as shown for an example in Fig. 2.8.

The RW structure, however, still has some limitations. In the RW laser, the injected carriers can spread to region B, see Fig. 2.6 (a), leading to incomplete carrier confinement in the active region. This makes it impractical to accurately determine the current density values in cases of narrow stripe ridge lasers [79]. In addition, the lateral optical confinement of the RW structures may not be sufficient for waveguiding in high bend loss structures such as S-bend, Y-junction and Mach-Zehnder devices.

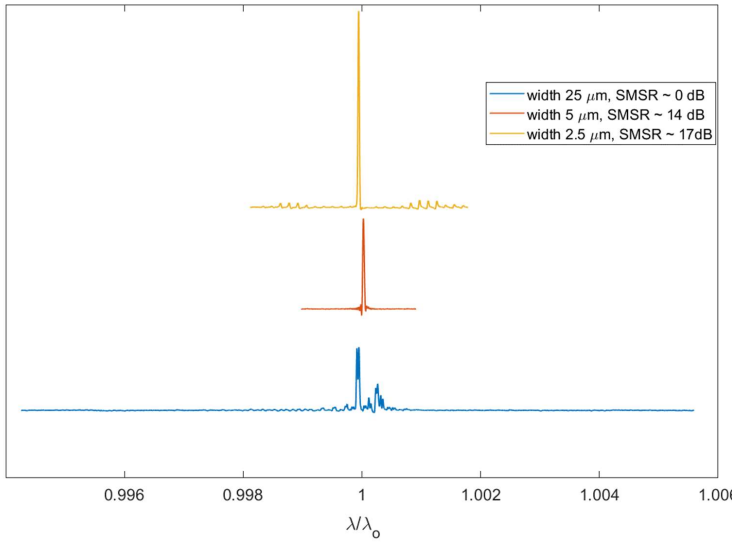

Figure 2.8: Lasing spectra of 2 mm long ridge-waveguide lasers with different ridge-waveguide widths, where all lasers are fabricated based on $Ga_{0.67}In_{0.33}As_{0.1}Sb_{0.9}/Al_{0.9}Ga_{0.1}As_{0.06}Sb_{0.94}$ active/cladding material, emitting at λ_0 = 2.33 µm.

2.3. Tunable semiconductor laser diodes

Tuning of the laser wavelength can be achieved if either the peak of the cavity gain curve or the comb-mode spectrum or both together are spectrally shifted [62]. The shift of both factors is related to the change in the effective refractive index of the active region (the tuning layer). As mentioned above, the effective refractive index of the active region is dependent on the carrier density. For semiconductor laser diodes, tuning is usually obtained by varying the injected currents into the tuning layer. This induces a change in the refractive index leading to change of optical length and thus the mode wavelength and FSR. The physics behind the change in the refractive index induced by the injected currents are the free-carrier plasma effect and the quantum confined stark effect [62]. In addition to the carrier injection, temperature is also a control parameter for the refractive index. Therefore, one needs to account for the effect of heating at high injected current to the change of the refractive index during tuning. Note that the tuning time due to carrier injection is only limited by the lifetime of the carrier which is in the ns range [62].

Although varying the current injection results in a continuous change in the effective refractive index [80], the wavelength tuning can be either continuous or discontinuous or quasi-continuous depending on the shift of the peak cavity gain and the comb-mode spectrum. A continuous tuning scheme is desirable for TDLAS, in which case the wavelength is tuned smoothly in arbitrarily small steps without mode changes. This requires the peak cavity gain and the comb-mode spectrum adjusted simultaneously in the proper proportion [81]. That makes this scheme less practical and limited to a small tuning range of 15 nm at 1550-nm wavelength. On the other hand, the discontinuous tuning scheme is mainly due to the mode hopping, which means the mode jumps from one longitudinal mode to another. The tuning, therefore, is only limited by the tuning range of the cavity gain characteristic which can be up to 100 nm at 1550 nm wavelength. However, this tuning scheme is less favorable because it cannot access all wavelengths within the tuning range. An intermediate tuning behavior can also be achieved in the quasi-continuous scheme, where small overlapping continuous tuning regimes can be joined to achieve a large wavelength coverage.

2.3.1. Y-junction laser

The Y-junction laser is a laser structure which is considered as a folded Mach-Zehnder (MZ) interferometer. This structure consists of two FP cavities, a relatively straight and an S-bend cavity, sharing a common section, as shown in Fig. 2.9. The geometrical path difference ΔL allows the selection of the overlapped modes (supermodes or MZ modes) between two mode-combs of these two cavities, called the Vernier effect as illustrated in Fig. 2.10, thus enabling the interferometric tuning behavior of the Y-junction lasers with the mode-comb of one cavity shifting relative to the other. The MZ modes, therefore, become dominant modes and the new FSR of the whole structure is given by [62]

$$\Delta\lambda_Y = \frac{\lambda^2}{2n_{g,eff}\Delta L} \tag{2.27}$$

which introduces a modulation to the cavity gain by a factor $C_Y(\lambda)$ [62]

$$C_Y(\lambda) = cos^2\left(2\pi \frac{n_b(\lambda)L_l - n_s(\lambda)L_s}{\lambda}\right) \tag{2.28}$$

where the lengths L_l and L_s are illustrated in Fig. 2.9 (a).

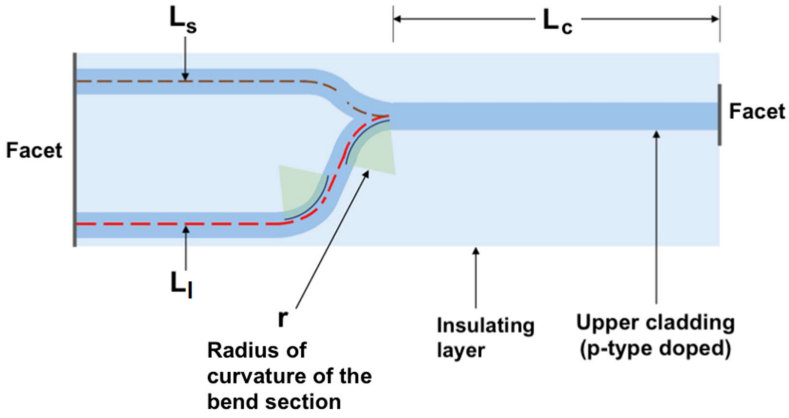

(a)

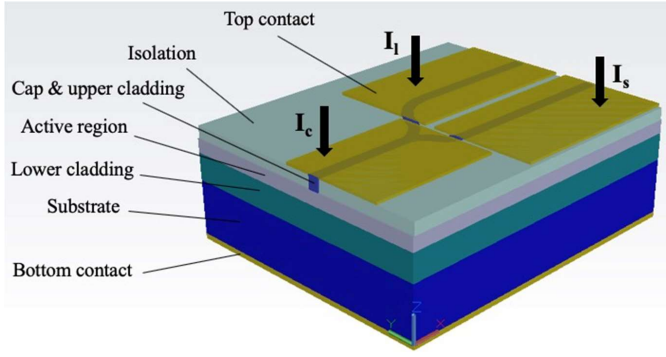

(b)

Figure 2.9: Schematic of Y-junction laser structure, showing (a) top view and (b) 3-D structure with different injected currents.

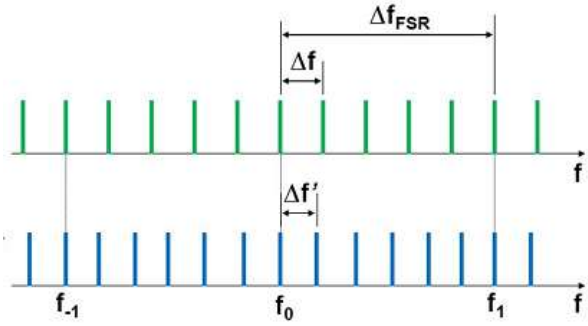

Figure 2.10: Vernier effect for mode selection in the Y-junction laser, where Δf and $\Delta f'$ are the longitudinal mode spacing of the short FP (L_s + L_c) and the long FP (L_l + L_c) cavities, respectively. Here, the f_{-1}, f_0 and f_1 are the MZ modes.

Tuning of the wavelength in a Y-junction laser can be achieved by adjusting injected currents into each section of the Y-junction, see Fig. 2.9 (b). The emitted wavelength can be tuned in two different ways which allow the largest variety of controllable applications [52]. The first tuning scheme is based on the variation of the MZ filter across the Fabry-Perot (FP) modes. By varying the ratio of the injection currents into the relatively straight section (I_s or I_2) and the S-bend section (I_l or I_3), a sawtooth-shaped tuning behavior can be observed as shown in Fig. 2.11(a) when the position of the MZ loss minimum is tuned across the allowed FP modes (continuous tuning) until the neighboring minimum reaches the same low level (step-like tuning). By combining with variations of the injected current into the common section (I_c or I_1), a wide tuning range of up to 50 nm can be obtained [53]. This would be advantageous as it can enable several gases to be detected by one single laser. The second tuning scheme is achieved by changing all the injected currents simultaneously (usually equal) to shift the whole gain curve across the MZ filter. Step-like tuning behavior can be observed, as shown in Fig. 2.11(b), resulting from the switch of the supermode when the level of the next MZ loss minimum has reached the value of the previous one. Together with the fabrication simplicity of the Y-junction structure which only requires a single epi-growth step as well as conventional photolithography and standard cleanroom processes, the tuning scheme of the Y-junction laser is advantageous for a large variety of applications, especially for TDLAS.

The Y-junction lasers still have some limitations. To enable the tuning function of the Y-junction laser, it requires three control currents that make it less favorable from a practical viewpoint. Moreover, the Y junction laser has an inherent tradeoff between its tuning range and the SMSR [54]. For a large value of $\Delta\lambda_Y$, the SMSR provided by the Y-junction structure may be not sufficient to ensure single mode operation. To improve SMSR of the Y-junction laser, one can add a grating structure similar to the DFB structure. Another solution is to use a three-branch (Y3) junction laser [55, 82]. The Y3-junction lasers improve over the conventional Y-junction laser by achieving simultaneously a better SMSR and a wider tuning range, up to 25 dB and 45 nm, respectively [82]. Waveguiding in the high-loss bend section of the Y-junction is also a big issue which requires high enough lateral index contrast. According to Breivik [61],

the index contrast should be as high as 0.04-0.05 to guide light in such waveguide structures, especially with small bend radius.

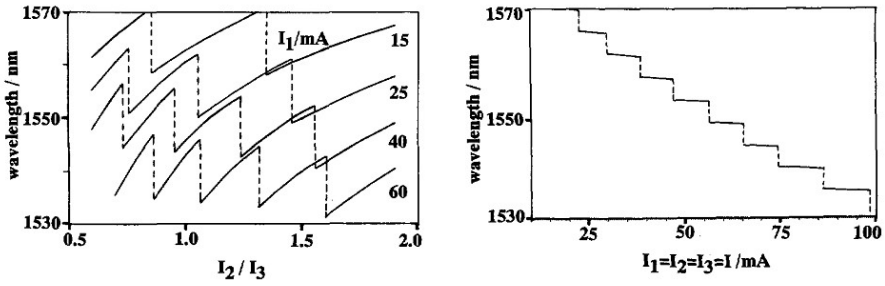

(a) (b)

Figure 2.11: Tuning scheme in a Y-junction laser diode. (a) Variation of the MZ filter across the Fabry-Perot (FP) modes exhibits a sawtooth-shaped tuning behavior. (b) Shifting the whole gain curve across the MZ filter exhibits a step-like tuning behavior [52]. (© 1994 IEEE)

Optical loss in Y-junction lasers

The optical loss in Y-junction lasers is dominated by the loss in the bend section. Similar to for the straight waveguide, the total optical loss α_t in the bend waveguide can be calculated from the condition of mode self-reproduction after each round trip, as shown in Eq. 2.29 [71].

$$\exp(-2\alpha_t L) = R_1 R_2 . \exp(-2\alpha_i L) . \exp(-4\theta . \alpha_{bend}) . T_{m1}^4 . T_{m2}^2 \qquad (2.29)$$

where α_{bend} is the radiation bend loss coefficient (loss per radian) and θ is the bend angle in radians. Here we introduce two loss factors T_{m1}^4 and T_{m2}^2, where T_{m1} represents the mode mismatch transition loss between the straight and curved waveguide segments (four transitions per round trip), and T_{m2} represents the mode mismatch transition loss between two oppositely curved waveguide segments (two transitions per round trip), as shown in Fig. 2.12. We also assume that the internal losses in the straight and bend waveguide segments are similar.

In the case of HICRW, the radiation loss due to bending is negligible, so the optical losses due to mismatch transition between different segments of the bend waveguide, as a function of bend radius, become dominant. Thus, the total optical loss in the bend waveguide is

$$\alpha_t = \alpha_m + \alpha_i + \frac{2}{L} ln \frac{1}{T_{m1}} + \frac{1}{L} ln \frac{1}{T_{m2}} \qquad (2.30)$$

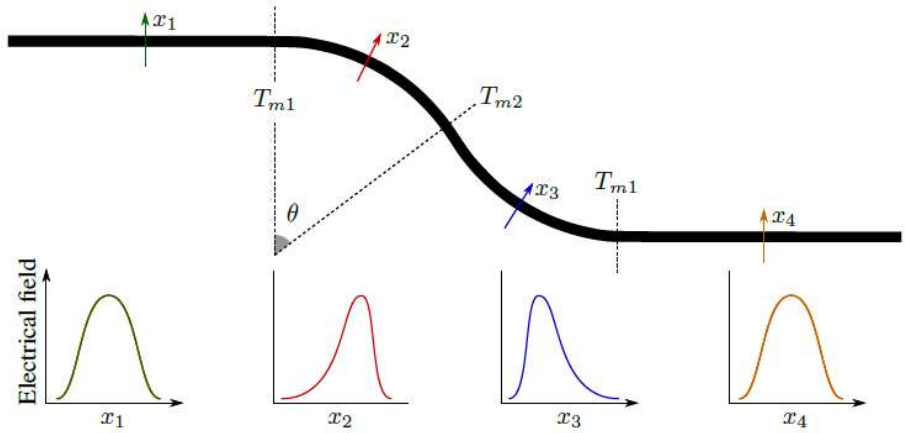

Figure 2.12: Sketch of an S-bend waveguide with the electric field mode shape in each waveguide segment [83]. The amplitude of the loss factors T_{m1}, T_{m2} is determined by the overlap between the modes in different waveguide segments. Simulation results show that the overlap between the bend and straight segment modes decreases with decreased bend radius [71].

2.3.2. Other tunable laser structures

Other interesting tunable laser structures are DFB and VCSEL. Due to the nature of the structure (single-mode behavior and large FSR), the DFB and VCSEL lasers can be tuned continuously without mode hopping. However, the tuning range is limited by the tuning range of the cavity gain characteristic. For DFB lasers, the wavelength tuning is in the range of several nanometers and is usually controlled by temperature induced by electric current with the typical tuning rate of 0.2 - 0.3 nm/^{o}C [3, 84, 85]. Meanwhile, the VCSEL lasers are usually tuned by electric current with a tuning range up to 15 nm at 2.3 µm [86]. In order to extend the tuning range of these laser structures, one can exploit external structures, e.g., a VCSEL using a top movable DBR mirror can be tuned up to 102 nm at 1.55 µm [87].

Chapter 3

LASER FABRICATION AND CHARACTERIZATION

Fabrication of semiconductor laser diodes is a complicated process, involving the growth of laser structures, the laser processing using cleanroom facilities and the laser characterization. Epitaxial growth of high quality multi-layer laser structures is critical for the performance of the laser diodes, in terms of electrical and optical properties. The growth defines the laser structure as a diode by doping for electrical purpose as well as provides the transversal optical confinement. The purpose of laser processing is to confine light in lateral direction, to create the resonator cavity and to provide the electrical contacts. Finally, the laser characterization ensures that the lasers perform as expected or/and provides feedback to the growth and processing of the lasers. In this chapter, the fabrication of GaSb-based laser diodes is presented from the starting point of GaSb substrate to the fully-characterized devices.

3.1. Laser growth

The growth of the laser structure requires a precise control of the growth conditions to minimize the presence of defects and impurities inside the laser structure. Noting that defects and impurities are the recombination centers which can significantly affect the performance of the optical devices. In order to obtain a low-defect structure, the laser structure must be in a single crystalline phase. That means every layer needs to be epitaxially grown on each other. The term "epitaxial growth" refers to the deposition of a crystalline layer, called epilayer, on a crystalline substrate, where the deposited atoms or molecules continuously build layers sharing the same crystallographic orientation with the existing substrate. Since the laser structure is a stack of different epilayers with abrupt interfaces, these epilayers in general need to be lattice-matched. However, sometimes a slight lattice mismatch is used to engineer the band parameters, e.g., a compressive-strained GaInAsSb QW is favorable to enhance the laser characteristics of GaSb-based laser diodes. Last but not least, the laser growth should be carried out in a high vacuum environment to minimize the incorporation of impurities.

3.1.1. Material systems

Direct band gap III-V semiconductors are highly suited materials in electro-optical applications. Especially for semiconductor laser diodes, the recombination of electrons and holes without involving phonon emission in direct band gap materials is crucial for the predominantly radiative recombination of the electron-photon interaction. Most of the III-V compounds have a zinc-blende (ZB) crystal structure in bulk form. This type of structure can be considered as

two interpenetrating face-centered-cubic structures of group III and V atoms, where the group V unit cell is translated ¼ {111} relative the group III unit cell as shown in Fig. 3.1.

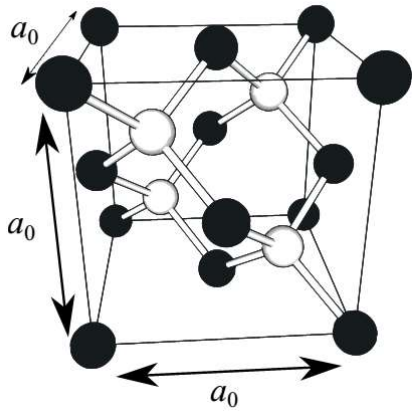

Figure 3.1: ZB crystal structure [61] created by group III elements (black) and group V elements (white).

The semiconductor laser diodes emitting light in the mid-IR region (2 – 5 µm) are strongly needed for light sources of TDLAS. In this wavelength regime, the III-V semiconductor material system (AlGaIn)(AsSb) is of particular interest. The quaternary alloy GaInAsSb grown on GaSb substrate is an important material for gain medium to emit light in the wavelength range from 1.5 µm up to 3.73 µm [37, 88]. Meanwhile, the quaternary AlGaAsSb and quinternary AlGaInAsSb are well suited for the barrier and cladding layers.

GaInAsSb For the quaternary $Ga_{1-x}In_xAs_ySb_{1-y}$ active layer, the bandgap and lattice constant can be adjusted by changing its composition. The lattice constant of this compound can be matched to that of GaSb if the requirement y = 0.913x is satisfied [89]. That leads to the bandgap of $Ga_{1-x}In_xAs_ySb_{1-y}$ active layer lattice-matched to GaSb at 300 K [90] to be

$$E_g(x, 300\ K) = 0.725 - 1.035\ x + 0.6\ x^2 \qquad (3.1)$$

In laser band engineering, the compressively strained GaInAsSb QW is favorable to enhance the laser characteristic. The compressive strain up to 2.4 % [91, 92] induces a separation of the light hole and heavy hole band, reducing the band-edge density of states and increasing the effective barrier height for the quantum-confined hole states. This leads to a reduction of the non-radiative Auger recombination, which is the dominant non-radiative mechanism at long wavelength regime [90]. Another advantage of compressive-strained materials is that the in-plane effective mass of the heavy hole is very small [93], resulting in the reduction of threshold current density and the increase of the differential gain of the active region [94].

AlGa(In)AsSb Thanks to the large band gap and low refractive index compared to GaInAsSb, the quaternary compound AlGaAsSb lattice-matched to GaSb is the ideal material to provide both optical and electrical confinement in type-I GaSb-based laser diodes. The hole confinement, however, is less sufficient when the wavelength is above 2.7 µm due to very low VBO of the AlGaAsSb/GaInAsSb material system [38]. By adding indium and increasing the As-content in the AlGaAsSb compound, the VBO can be increased, allowing better confinement of holes for laser diodes emitting above 3 µm [36, 95]. Besides, doping of AlGa(In)AsSb cladding layers is crucial in order to create a region capable of injecting carriers into the active region and reduce the resistivity of the laser structures.

3.1.2. Growth technique

Among growth techniques, molecular beam epitaxy (MBE) is versatile, advantageous and preferable for laser growths, thanks to the low growth temperature and low growth rates at ultra-high vacuum conditions. Because of the low temperature and deposition in vacuum, MBE growth is carried out under non-equilibrium thermodynamic condition, allowing the growth of complex structures with abrupt interfaces and even metastable states. $Ga_{1-x}In_xAs_ySb_{1-y}$ is a typical example since it is not miscible in its entire composition range. For alloys lattice-matched to GaSb, the miscibility gap occurs when $0.2 < x < 0.85$ [96]. Using MBE, it is possible to grow the composition of $Ga_{0.46}In_{0.54}As_{0.52}Sb_{0.48}$ lying in the center of the miscibility gap [33]. With the low growth rate, typically one monolayer per second, MBE is a suitable technique for the growth of nano-structures, such as nanodots, nanowires and quantum wells. In the MBE process, the materials are grown in ultra-high vacuum, thus, high quality structures with very low impurity concentration can be achieved.

In this study, all laser samples were grown in a Varian Gen II Modular MBE system, illustrated in Fig. 3.2, at the Department of Electronic Systems at NTNU. The base pressure of 10^{-10} Torr allows a very long mean free path of evaporated particles towards the substrate and very low impurity incorporation. The growth temperature is typically in the range 370 – 520 °C depending on materials. The system has five sources (or effusion cells) of III or V elements including Al, Ga, In (group III), and As, Sb (group V). Besides, there are three other sources for doping purpose: Be (p-type dopant), GaTe (n-type dopant) and Si (either p- or n-type dopant depending on materials and growth conditions). In the MBE process, the group III and dopant source materials are heated and evaporate towards the substrate, and the flux of the evaporated particles is controlled by the sources' temperature. The group V source materials are contained in valved cracker effusion cells which can combine the evaporation of tetramers (As_4 or Sb_4) and cracking process for producing dimeric molecules (As_2 or Sb_2) or even monomers (As or Sb). Each source is associated with a mechanical shutter to interrupt the material beam towards the substrate. To ensure high structural quality with low defect density, the laser growth should be carried out in a group V rich flux condition with a typical V/III flux ratio of more than 1.3 [97]. Therefore, the growth rate of the III-V epilayers is determined by the flux of the group III elements.

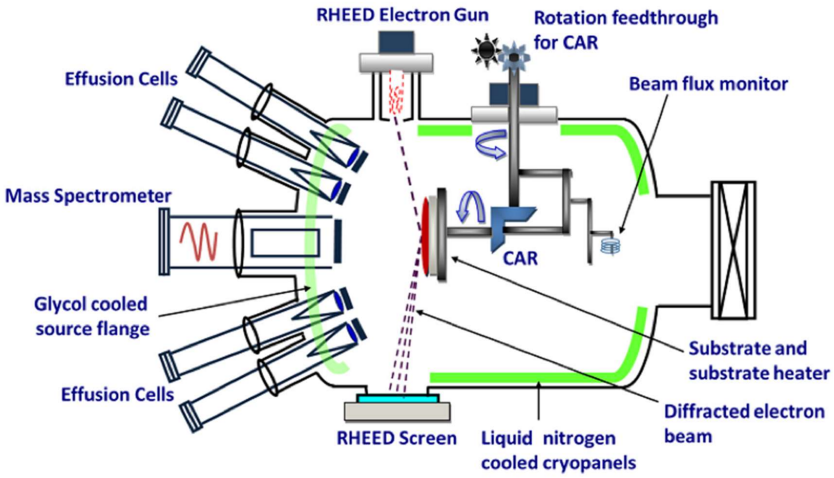

Figure 3.2: Schematic of the MBE system used in this work [63]. Inside the MBE chamber, the *in-situ* reflection high-energy electron diffraction (RHEED) is used to monitor the oxide desorption and the surface reconstructions of the substrate, as well as to calibrate growth rates. The beam flux monitor, which is a pressure gauge, can be rotated into the sample position to measure the molecular beam fluxes.

3.1.3. Growth of laser structures

From the electrical point-of-view, the laser structure grown on n-type doped GaSb substrate is a p-i-n diode where the intrinsic active region is sandwiched between n-type and p-type doped cladding layers. The n-type doped substrate is the starting point of the laser structure, thus requiring wafer material of very high quality. In this work, double side polished Te-doped GaSb (001) wafers with a nominal carrier concentration of 5×10^{17} cm^{-3}, an etch pit density of less than 500 cm^{-2} and a thickness of 500 µm provided by Wafer Technology Ltd. have been used for growth of laser structures. Prior to the actual laser structure growth, a Te-doped GaSb buffer layer is grown to improve the surface quality, followed by a Te-doped graded bandgap transition layer to smoothen the barrier for electrons. Within the buffer layer, a Te-doped GaSb/AlSb superlattice structure is introduced to minimize the propagation of any dislocation defects toward the active region of the lasers. For the typical laser structure growth in this work – sample Sb307, the active region consists of three 12 nm wide compressive-strained InGaAsSb QWs separated by 20 nm wide AlGaAsSb barriers and sandwiched between two 145 nm wide SCLs. The SCLs have similar composition to the barrier and act as a core for optical waveguiding and confinement of the charge carriers since the QWs are too thin. Being sandwiched between the doped AlGaAsSb cladding layers, the active region is nominally undoped and therefore is weakly p-type due to the native acceptors in GaSb-based materials. With high Al-content up to 90%, the cladding layers are designed for optical confinement in the transverse direction due to lower refractive index, as depicted in Fig. 3.3, and for additional

electronic barriers for the charge carriers due to larger bandgap. The lower cladding layer is n-type doped with Te and the upper cladding layer is p-type doped with Be. The dopant concentration in the cladding layers should be sufficient to achieve good electrical conductivity while minimizing the defect levels as investigated in section 5.1. Towards the waveguide layer it is advantageous to lower the doping concentration to reduce losses due to the free carrier absorption [63, 96]. The topmost layer of the laser structure is a heavily doped GaSb cap layer with a doping concentration of up to 2×10^{19} cm^{-3}, protecting the laser structure from air and providing the low specific contact resistivity with the metal contacts. Between the upper cladding and the cap layer, Be-doped graded bandgap transition layer is introduced to smoothen the barrier for holes. Details of bandgap profile and layer information of the nominal laser structures of sample Sb307 are given in Fig. 3.4 and Tab. 3.1. More information about the laser growth process can be found in Patra's [63] and Selvig's works [97].

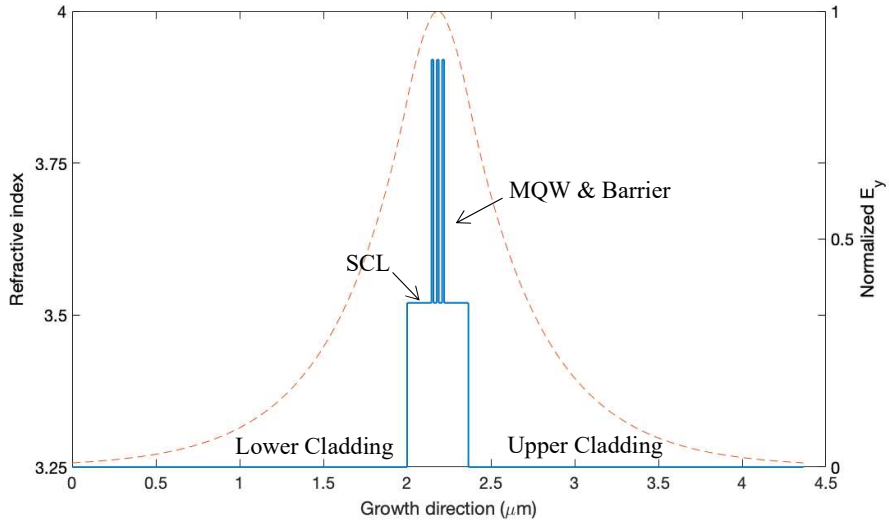

Figure 3.3: Refractive index profile (solid line) of the AlGaAsSb/GaInAsSb based laser structure (sample Sb307) for lasing at 2.33 µm wavelength [63]. Here, the effect of graded doping in cladding layers on the refractive index profile has been neglected. The active region has a thickness of 366 nm and an effective refractive index of 3.523 calculated by ERIM. These parameters are used in all simulations in chapter 2. The dashed line shows the normalized electric field profile E_y of the fundamental TE mode confined in 1-D slab waveguide. This simulation was performed using the 1-D mode solver for dielectric multilayer slab waveguides [98].

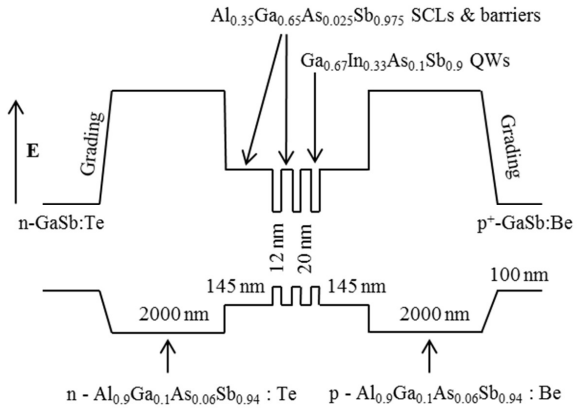

Figure 3.4: Bandgap profile of the laser structure Sb307 emitting at 2.33 μm wavelength. Note that the band bending due to doping is not shown in this figure.

Table 3.1. Layer information for the nominal laser structure of sample Sb307 emitting at 2.33 μm.

Layer	Material composition	Thickness (nm)	Type of doping / Carrier concentration (cm^{-3})	Growth temp. (°C)
Substrate	GaSb	5.0×10^5	n-type / 5.0×10^{17}	-
Buffer	GaSb	130	n-type / 5.0×10^{17}	520
30×superlattice	AlSb/GaSb	0.1/0.3	n-type / 4.1×10^{17}	520
Buffer	GaSb	250	n-type / 5.0×10^{17}	520
Grading	AlGaAsSb/GaSb	42	n-type / 5.0×10^{17} → 1.6×10^{17}	520
Lower cladding	$Al_{0.9}Ga_{0.1}As_{0.06}Sb_{0.94}$	2.0×10^3	n-type / 1.6×10^{17} → 1.0×10^{17}	520
SCL	$Al_{0.35}Ga_{0.65}As_{0.025}Sb_{0.975}$	145	Intrinsic	430
MQW × 3	$Ga_{0.67}In_{0.33}As_{0.1}Sb_{0.9}$	12	Intrinsic	430
Barrier × 2	$Al_{0.35}Ga_{0.65}As_{0.025}Sb_{0.975}$	20	Intrinsic	430
SCL	$Al_{0.35}Ga_{0.65}As_{0.025}Sb_{0.975}$	145	Intrinsic	430
Upper cladding	$Al_{0.9}Ga_{0.1}As_{0.06}Sb_{0.94}$	2.0×10^3	p-type / 2.0×10^{17} → 5.0×10^{18}	370
Grading	AlGaAsSb/GaSb	42	p-type / 5.0×10^{18} → 5.0×10^{19}	370
Cap	GaSb	100	p-type / 2.0×10^{19}	370

3.1.4. Characterization of laser growth

X-ray diffraction

X-ray diffraction (XRD) is a versatile *ex situ* method for identification and characterization of crystalline materials. For laser structures, important conditions such as lattice matching and strain can be determined by XRD. The XRD technique is based on the diffraction effects that occurs when the wavelength of the impinging X-ray is on the length scale of the crystal lattice constant. Accordingly, the constructive and destructive interference should be observable when exposing the crystal structure to X-rays. The diffraction of X-rays by crystal planes is described by Bragg's law

$$2d \sin\theta = \lambda \tag{3.2}$$

where λ is the wavelength of the X-rays, θ is the angle between the X-ray beam and the crystal plane, and d is the distance between two adjacent planes specified by Miller indices hkl of the appropriate lattice planes given by Eq. 3.3.

$$d_{hlk} = \frac{1}{\sqrt{\frac{h^2}{a_x^2} + \frac{k^2}{a_y^2} + \frac{l^2}{a_z^2}}} \tag{3.3}$$

where a_x, a_y are the in-plane lattice constants corresponding to the Miller indices h, k while a_z is the out-of-plane lattice constant corresponding to the Miller index l. For a strained ZB layer, a_x and a_z are related to the bulk lattice constant a_0 by the following relation [99]

$$a_0 = \frac{a_z + \frac{2C_{12}}{C_{11}} a_x}{1 + \frac{2C_{12}}{C_{11}}} \tag{3.4}$$

where C_{12} and C_{11} are the elastic constants of the epilayer material. By measuring the Bragg diffraction angle θ for different sets of planes in the crystal, the lattice constants a_x and a_z can be obtained, which also leads to determination of in-plane strain. The Bragg diffraction angle θ can be found by Bond's [100] and Fatemi's method [101] which are described in detail by Breivik [61]. XRD characterization of all laser material growth in this work is carried out by a Bruker AXS D8 Discover X-ray diffractometer with X-ray wavelength of 1.5406 Å and maximum operational temperature up to 900 °C.

Fourier Transform PhotoLuminescence (FT-PL)

FT-PL is a common technique to measure the optical properties of the grown materials, such as the bandgap and optical quality. In this technique, electrons are excited from the valence band to the conduction band by optical pumping, typically using a laser source with photon energies $h\upsilon > E_g$. In this work, a 980 nm laser operating up to 500 mW is used for this purpose. The photoexcited electrons live some time before making a transition back to the valence band to

recombine with a hole. In a direct bandgap semiconductor of high crystal quality, the electron-hole recombination is predominantly radiative which results in luminescence. To obtain the PL spectrum, the emitted photons are directed to a Fourier transform spectrometer. For all PL measurements in this work, a Nicolet 8700 Fourier transform infrared (FTIR) spectrometer from Thermo Scientific equipped with an InSb detector having a detection range of 1 – 5 µm is used.

The energy of the emitted photon is close to the value of E_g, irrespective of the incident photon energy. The wavelength of the emitted light obtained from the PL spectrum, therefore, provides important information about the bandgap of the grown materials or the confinement energy of the quantum wells. This is crucial for designing lasers for gas detection, where the emitted wavelength must match the absorption line of the gas to be measured. Photoluminescence is also used to detect the presence of impurities and crystal defects in the semiconductor structures, thus providing information about the quality of the grown structures. A high-intensity peak with small full width at half maximum (FWHM) in the PL spectrum indicates a low impurity concentration and high crystal perfection of the grown laser materials [102]. Fig. 3.5 shows the PL spectra of some high quality grown laser samples as compared to a reference sample. The reference sample is a sample with good quality structure grown for comparison of other epi-grown samples.

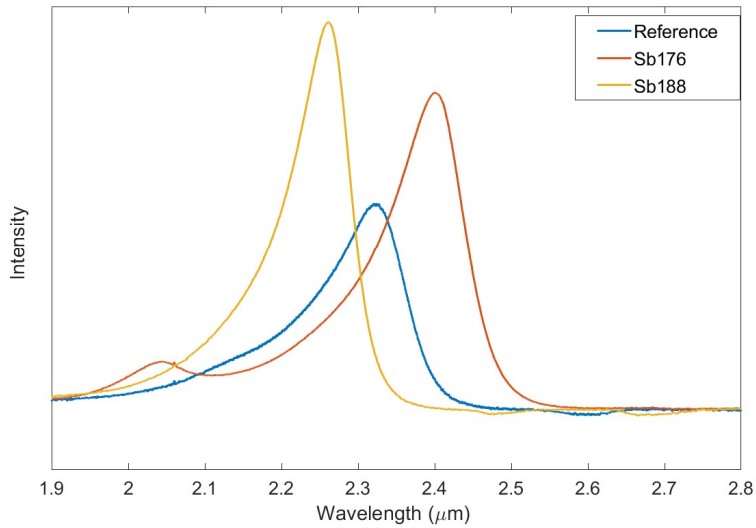

Figure 3.5: PL spectra of some high-quality laser materials – samples Sb176 and Sb188 (see detailed growth structure in Appendix B) – in comparison to that of a reference sample. For example, the PL peak of sample Sb188 at 2.25 µm wavelength has twice the intensity and a FWHM of 93.3 nm compared to the PL peak at 2.33 µm wavelength of the reference sample which has a FWHM of 133.3 nm, indicating a very high quality grown laser material of sample Sb188.

Hall measurement

Hall effect measurement is a popular method to determine the carrier concentration and carrier mobility in semiconductors. This technique plays a key role to characterize the dopant incorporation in the cladding layers as presented in section 5.1. For a Hall effect measurement, the doped layer of the semiconductor being analyzed must be grown on a semi-insulating substrate and be processed into a Hall bar structure as shown in Fig. 3.6. Under the effect of an external magnetic field B_z, a current flow with a current density of J_x induced by an electric field E_x will be subjected to the action of a Lorentz force F. The Lorentz force is a combination of two separate forces: an electric force and a magnetic force. The magnetic force exerted by the magnetic field B_z on moving charge carriers in the x-direction will drift these charge carriers in the y-direction, inducing an electric field E, known as Hall electric field, across the Hall bar. The resulting Lorentz force is therefore [103]

$$\mathbf{F} = q(\mathbf{E} + \mathbf{v} \times \mathbf{B}) \tag{3.5}$$

where q is the elementary charge (q equals to $-e$ for electron and $+e$ for hole), **E** is the Hall electric field, **v** is the velocity of the charge carriers and **B** is the magnetic field. In the y-direction, the force is

$$F_y = q\left(E_y - v_x B_z\right) \tag{3.6}$$

For electrons, the speed v_x and the electric field E_x are in opposite directions whereas for holes v_x is in the same direction as E_x. In the steady-state condition, the electric field E_y equals to $v_x B_z$ and can be determined by measuring the voltage V_y across the Hall bar

$$E_y = v_x B_z = \frac{V_y}{w} \tag{3.7}$$

where w is the width of the bar. The sign of V_y can be used to determine the doping type of the doped semiconductor, positive sign for p-type and negative sign for n-type. In the case of the p-type semiconductor, the current density is $J_x = v_x e p$ where p is the hole carrier concentration [103]. Thus,

$$p = \frac{J_x B_z w}{e V_y} \tag{3.8}$$

If the resistance R along the Hall bar is measured, the sample conductivity σ can be calculated

$$\sigma = \frac{L}{Rwt} \tag{3.9}$$

where L is the length of the Hall bar and t is the thickness of the doped layer. Since the conductivity is $\sigma = e\mu_h p$ for p-type semiconductors, where μ_h is the hole mobility [103], we get

$$\mu_h = \frac{L}{epRwt} \tag{3.10}$$

By using a known current density J_x and a known magnetic field B_z, the carrier concentration and the carrier mobility of the doped semiconductors can be determined precisely. All the Hall effect measurements in this work were performed by a Lakeshore 7504 Hall effect transport measurement system with a varying magnetic field from 0 to 0.5 T in both directions.

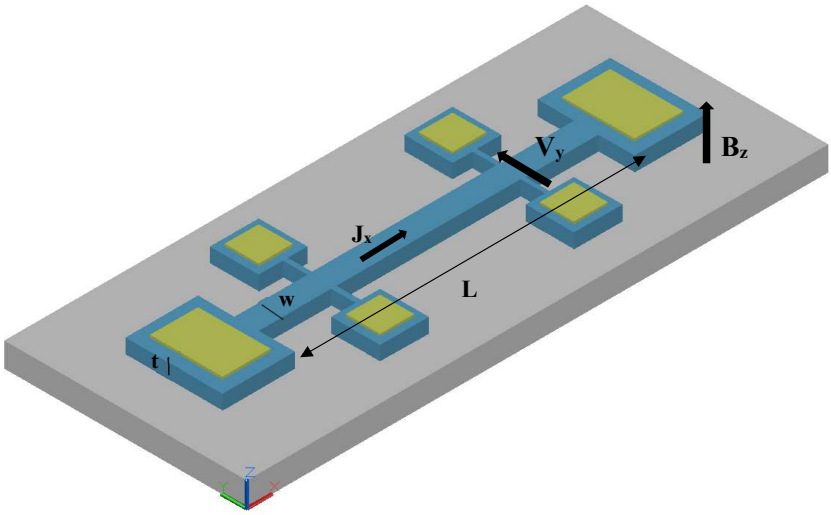

Figure 3.6: Illustration of the 1-2-2-1 Hall bar structure with the length of L and the width of w. The doped semiconductor (blue) has a thickness of t grown on top of an insulating substrate (grey). The yellow pads are the metal contacts for electrical measurement purpose.

3.2. Processing of laser devices

To obtain the final laser devices, the grown laser materials need to be processed to fulfill the requirements of the laser diodes. This work is a multi-step procedure, as depicted in Fig. 3.7, using various instruments at the NTNU Nanolab cleanroom facilities. The recipe was first developed by Breivik [61] and later optimized during my PhD time, see Appendix C. The optimization of the processing steps is a large part of this thesis, and the results are presented in sections 5.2 to 5.4 and chapter 4.

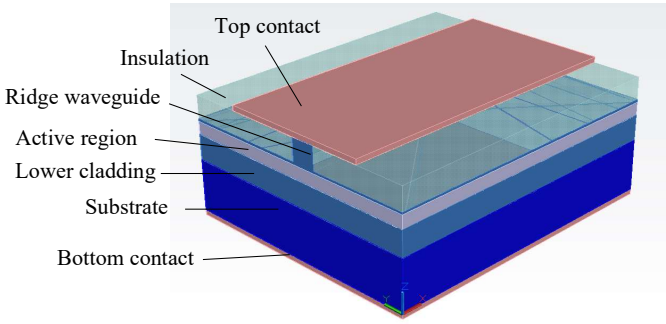

Figure 3.7: Illustration of a ridge-waveguide laser diode fabricated by multiple-step process.

3.2.1. Waveguide formation

As discuss in Chapter 2, a ridge waveguide structure can improve the beam quality of the semiconductor lasers. The formation of the ridge waveguide is based on the waveguide patterning and the etching process. With a critical dimension of the waveguide width in the range of few microns, the conventional ultraviolet (UV) lithography is sufficient to pattern the waveguide structure. A vertical profile of the waveguide is preferable for electrical and optical confinement. Thus, the profile of the patterned photoresist is also required to be vertical. In this study, different positive photoresists were characterized to achieve optimal parameters (e.g., thickness, exposure dose …) for a steep profile of photoresist. Besides, the use of edge bead removal (EBR) technique is important in the photolithography process to minimize the gap between mask and sample in order to improve the resolution as well as the resist profile [61]. The optimal profile of the ridge waveguide is about 85°, achieved by using the photoresist AZ 5214E, as shown in Fig. 3.10.

The etching of the waveguide structure can be done by wet etching or dry etching methods. The anisotropic property of the dry etching makes it preferable for laser waveguide etching to create the vertical-profile waveguide with a smooth etched surface. The dry etching of III-V semiconductors is mostly based on the chlorine-based gas chemistry [104]. For GaSb and its related compounds (e.g., AlGaAsSb and InGaAsSb), typical reactive gases used for the etching process are BCl_3, Cl_2, $SiCl_4$, CCl_4, and CCl_2F_2 [105-108] where Cl_2, $SiCl_4$ and CCl_4 result in high etch rates while BCl_3 provides a smooth etched surface. Other gases are also added to enhance the physical etching (e.g., Ar) or to preserve good morphology of the etched surface (e.g., H_2) [105] or to increase the reactive ion concentration (e.g., N_2) [109]. In the reactive ion etching (RIE) process, the chlorine-based etchant radicals and ions are formed by electron collisions with the gas molecules in an oscillating electric field between a top electrode and the sample. The reactive radicals are absorbed by the surface of the sample and chemically react to create volatile products. Spontaneously, the ionized gases are accelerated by the electric field and bombard onto the sample surface, resulting in physical, anisotropic etching. The rate of chemical and physical etch can be controlled separately by using an oscillating magnetic field to ionize the gases without accelerating them towards the sample. This is referred to as ICP-RIE.

In this study, all lasers were etched following the etching recipe developed by Oxford Instruments using BCl_3/Ar gas chemistry in an Oxford Instrument Plasmalab System 100 ICP-RIE [110]. It is important to control the etch depth, which is the main focus of section 5.2. The ridge-waveguide etch depth plays a key role in the laser's characteristics, namely the optical confinement and surface recombination of injected carriers [111, 112]. By forming the ridge structure and isolating the ridge sidewall with a low index material, a large index contrast is created to well-confine light inside the waveguides. This is very critical for reducing high bend losses in waveguide structures such as S-bend, Y-branch and Mach-Zehnder interferometer. In section 5.2, our simulation outcome shows the effect of increased confinement in the waveguide when the etch depth is well-defined. To achieve the optimal optical and electrical confinement for the mid-infrared laser performance, it is desirable to stop etching at the interface between the upper cladding layer and the SCL layer. Using *in situ* reflectance monitoring with a 675 nm-wavelength laser, it was possible to determine the etch stop with high accuracy [113]. It was shown that, based on the simulations of laser reflectance from a reference sample, the etching process can be controlled to provide an endpoint depth precision within ± 10 nm.

3.2.2. Waveguide isolation

Due to the reactive nature of AlGaAsSb [114-116], as depicted in Fig. 3.8, the waveguide sidewall needs to be protected from oxidation in air. This procedure is critical for the long-term stability of the GaSb-based laser devices. The isolation material must also be insulating, such as ceramic or polymer. In this work, SiO_2 and photoresist ma-N440 were investigated for the isolation of the ridge waveguide sidewalls.

For the waveguide isolation using SiO_2, a 200 nm thick SiO_2 layer was deposited on the as-etched sample by the plasma-enhanced chemical vapor deposition (PECVD) technique. The sample then underwent an annealing process for metallization in the subsequent step of the laser processing. However, due to the stress caused by thermal expansion coefficient mismatch between SiO_2 and GaSb-based compounds [117, 118] after annealing, the SiO_2 layer was separated from the cladding layer as shown in Fig. 3.9. Therefore, it was concluded that SiO_2 is not applicable as an isolation material for the laser processing.

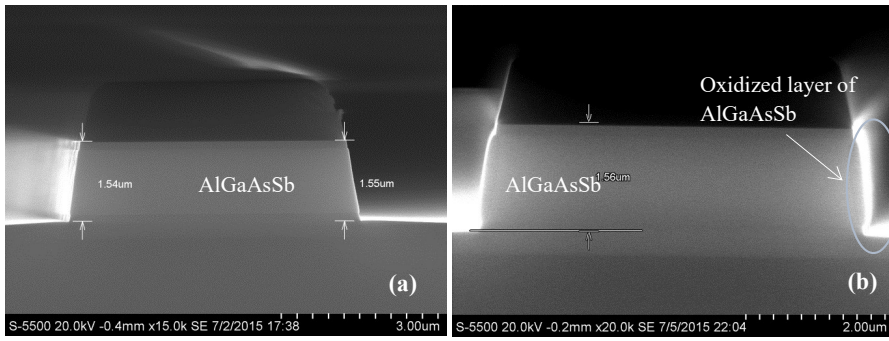

Figure 3.8: Ridge waveguide structure of AlGaAsSb/InGaAsSb laser diode (a) as-etched and (b) after 3 days in air.

On the other hand, the post-hardening photoresist ma-N440 provides a good chemical and mechanical protection for the ridge structure. The photoresist was first spin-coated on the as-etched sample and followed by hardening step at high temperature. It is worth noting that the photoresist needs to be completely cross-linked [119] to prevent the formation of voids due to the shrinkage in the subsequent steps as shown in Fig. 3.10 (a). It is desirable that the thickness of the isolation layer is the same as the height of the waveguide. This provides a planar platform for the metallization of the top contact. Using photoresist as the isolation material is advantageous since it can be etched until exposing the surface of the ridge. The resist was etched by O_2/CF_4 gas chemistry in the ICP-RIE chamber, where the CF_4 gas was added to improve the smoothness of the resist surface after etching [61, 120]. This part of the process in this work does not require a mask, but needs to be well-controlled. The surface of the ridge must be clean of the resist for contacting purpose and the height difference between the ridge's and the resist's surface should be small to avoid the break of the metallization layer shown in Fig. 3.10 (b).

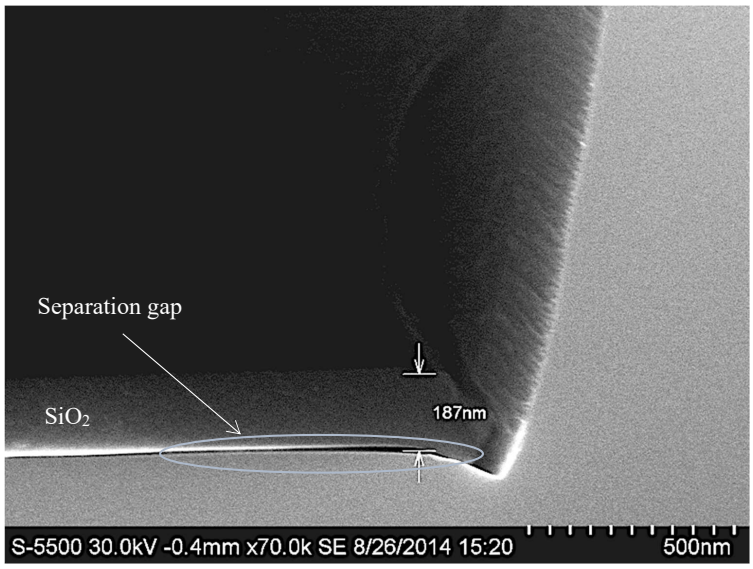

Figure 3.9: After annealing, the SiO_2 layer was partly separated from the cladding layer due to the mismatch of their thermal expansion coefficients.

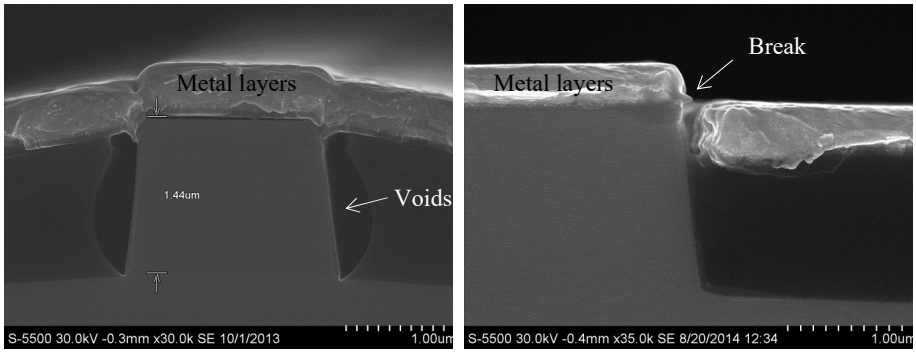

Figure 3.10: Problems with regards to the usage of photoresist ma-N440 for isolation of waveguide sidewall. (a) Void formation due to incomplete hardening of photoresist. (b) Break of the metal contact due to over-etching of photoresist.

3.2.3. Metallization and annealing

Metal contacts to the laser diode are required for the external power connections. To enhance the current injection and to minimize the heat generation in the laser structures, it is important to create good ohmic contacts to the laser diode. Prior to the metallization, the removal of the

GaSb native oxide layer is essential to obtain such good contact property. In section 5.3, the effect of several plasma-assisted oxide removal techniques prior to metallization of p-type GaSb was investigated in comparison to the conventional chemical methods. The specific contact resistivities obtained from transfer length method (TLM) measurements show a significant improvement of the contact properties after surface pre-treatment by H_2/Ar sputter etching or by *in situ* low-ion-energy Argon irradiation. It is noted that, by eliminating sample exposure to air, *in situ* Ar irradiation becomes a promising technique for high performance GaSb-based semiconductor diode lasers.

The contact separation in between neighboring lasers or in between the laser sections (in the case of Y-junction lasers) can be achieved by the photolithography and lift-off process. In the lift-off process, the negative profile (sidewall angle is greater than 90^0) of the photoresist, as shown in Fig. 3.11, is necessarily required to support the removal of the unwanted parts of the metal layers. An image reversal resist, such as AZ 5214E is best suited for this work, since it can be used as a positive photoresist for EBR and as a negative resist for creating the negative profile. The deposition of metals onto the sample surface is usually performed by evaporation or sputtering. The advantages of the evaporation over the sputtering are high deposition rate and less surface damages from impinging atoms. In this work, the metallization is performed by electron beam evaporation in a combined sputtering and e-beam evaporation system (AJA ATC-2200V) at a starting pressure of 10^{-7} Torr. To improve the contact properties, the samples after lift-off process undergo a rapid thermal anneal at 290 ºC for 45 s. The role of the annealing procedure is presented in the paper in section 5.4. In this paper, different metallization systems used for contact to p-type and n-type doped GaSb have been investigated. The electrical properties of the contacts were characterized via the measurement of the specific contact resistivity, the laser performance and the laser reliability. We also demonstrated that the aluminum-based contacts perform as good as the conventional gold-based contacts.

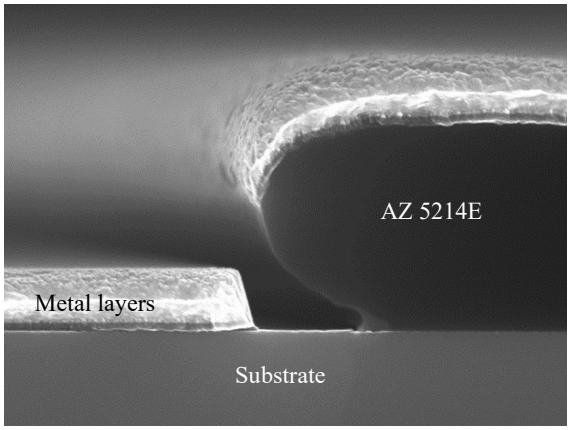

Figure 3.11: Negative profile of photoresist AZ 5214E for lift-off process.

3.2.4. Thinning and cleaving

A thick substrate is preferable in the fabrication process for handling, i.e., spin coating and etching. However, a typical thickness of 500 µm of the GaSb substrate will result in high electrical and thermal resistance of the laser diodes. Therefore, all laser samples need to be thinned to the target thickness of 100-150 µm before applying the backside metallization. This is an important procedure for mid-infrared semiconductor lasers where the heating is a big issue due to Auger recombination. Papis-Polakowska et al. [121] have investigated the chemical mechanical polishing process of GaSb to achieve good surface morphology. In this work, to avoid the use of chemicals, only mechanical polishing using grinding sand papers was used to thin laser samples. Poor surface morphology of the backside of the laser samples is often obtained, however, it does not affect the laser performance. It is worth noting that a GaSb substrate is much more brittle than a Si substrate. Thus, the normal thinning procedure of Si cannot be applied for GaSb.

A thin sample also supports the laser cleaving where a small cleaving force can be uniformly applied to achieve perfect laser facets. This is important to define the mirrors of the laser devices. The cleavage behavior of the III-V semiconductors depends on the ionic contribution to the bonding [122]. The ZB crystals break along the nonpolar (110) plane which consists of equal number of group III and group V atoms. For this reason, all laser waveguides from the (001)-oriented laser samples need to be perpendicularly or parallel aligned to the (110) plane. After thinning and backside metallization followed by the annealing step, the laser samples are cleaved into their proper lengths, depending on the measurement purpose. For example, different lengths of the laser devices are used for measurement of internal quantum efficiency, internal loss and transparent threshold current density. The cleaving process is usually performed in two stages. The samples are first scratched with a sharp diamond tip at the cleaving mark position, which induces structural defects on the samples' surface. Secondly, by applying a load to the samples, the crack propagation is initiated, starting from the scratched position and generates an atomically sharp crack [123]. To reduce the stress applied on the ridge waveguide during the cleaving process, support structures are introduced as shown in Fig. 3.12. The as-cleaved laser devices are now ready for being measured or being facet-coated by the optical coatings to improve output performance which is the main topic of chapter 4.

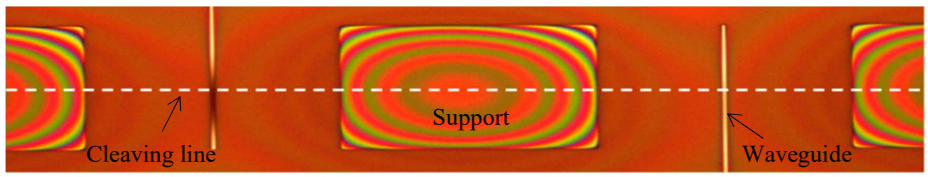

Figure 3.12: Ridge waveguides and support structures exposed after etching back the isolation material (section 3.2.2). The support structures are believed to reduce the stress applied on the ridge waveguide structure during the cleaving process, and thus reducing damages on the laser facets.

3.2.5. Contacting

For the measurements of laser devices, the connections between external current sources and laser contacts are required, see Fig. 3.13. In most of the cases, the lasers are mounted episide-up on copper heat sinks (or copper plate). The episide-down mounting is used to enhance the heat dissipation of the laser, especially for quantum cascade lasers and very high power lasers [124]. However, it is only applicable for a single laser, whereas the episide-up mounting can be applied for many lasers on the same bar. The mounting of laser diodes on copper heat sinks is usually obtained by silver glue or indium-soldering. In this procedure, the laser devices are stuck to the adhesive in the liquid form. The adhesive is then solidified and provide a good electrical and thermal connection. To control the operating temperature of the lasers, the copper plate can be actively cooled using a thermoelectric cooler (TEC), or Peltier element. In this work, the copper plate was mounted on the TEC and was secured by screws. A thermocouple was attached on the copper plate to measure the temperature and send the feedback to the temperature controller to control the TEC.

For the connection of the top laser contact, the two most common techniques used in this work are probing and wire-bonding. Probing is a technique where a thin metal probe lands on the metal pad of the device by x-y-z manipulators. It is quick and easy to attach and detach the probe to/from the laser diodes, allowing the measurement of many laser diodes in a short time. Wire-bonding technique, on the other hand, provides a permanent contact to the laser diodes by fusing a metal wire to the contact metal using ultrasonic vibrations at relative high temperature – above 100 °C. This technique can be applicable for very small contact area, e.g., the TLM pattern in section 5.3, and is applied when the laser measurements require stable contacts for long time measurements such as the reliability test. It is worth noting that the bonding force needs to be small to reduce damages to the underneath laser structure. We observed non-lasing behavior of the lasers when the bonding force exceeded 80 g. One of the main drawbacks of using the photoresist ma-N440 as the isolation material is poor adhesion to the top metal contact pads. Thus, the top metal contact pads can be peeled off during the wire-bonding process. One solution is adding a thin layer of SiO_2 between the isolation material and the metal contact pads to improve the adhesion.

3.3. Testing of laser devices

Last but not least, the measurements of the laser output characteristics are crucial to provide feedback to the growth and processing of the laser diodes. There are four main measurements conducted in this work which are able to extract all of important characteristics of the as-fabricated laser diodes. The experimental setup for those measurements is displayed in Fig. 3.13. In this section, some typical experimental results are presented for the overview of the laser characteristics.

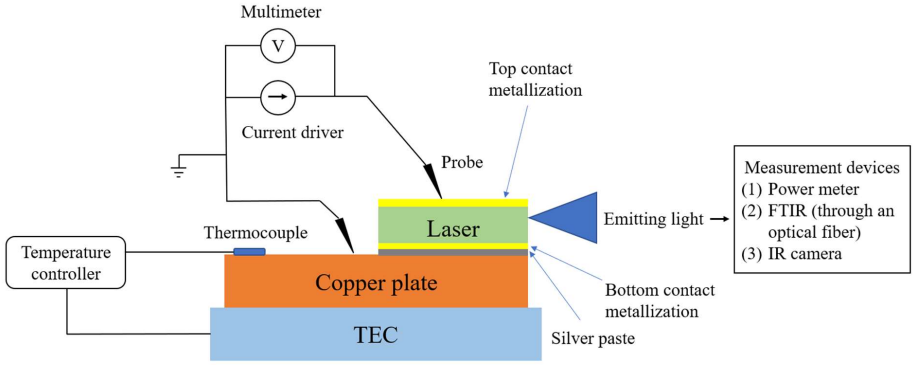

Figure 3.13: Experimental setup for the measurements of laser output characteristics. The injected current from the current driver was set manually or was automatically controlled by a National Instruments NI-9263 voltage source (NI-9263 DAC). For I-V measurement, a multimeter was used to measure the voltage between anode (laser top contacts) and cathode (copper plate). The emitting light from the laser device was guided to the measurement devices: (1) power meter for measuring the output power, or (2) FTIR (through a multimode optical fiber) for spectral measurements, or (3) IR camera for near- and far-field measurements.

3.3.1. P-I measurements

The P-I (often also denoted as "L-I") characteristic describes the relationship between the output light power and the injected current of the laser diodes, providing information on how effectively the injected carriers interact inside the laser structure and generate light through the electron-hole recombination. The following parameters can be extracted from the laser P-I diagrams, as shown in Fig. 3.14.

Maximum output power: For gas detection, the output power of the single mode laser source is desired to be in the order of 1 mW [4]. Power above 3 mW can saturate the photodiode used to analyze the transmitted signal in gas spectroscopy [5]. The typical output power of the fabricated Y-junction laser in this work is 1-2 mW which satisfies the requirement of output power of light source for TDLAS.

Threshold current density (J_{th}) is an important parameter of the laser diodes and is determined by

$$J_{th} = \frac{I_{th}}{wL} \qquad (3.11)$$

where I_{th} is the experimentally obtained threshold current, L is the laser cavity length and w is the width of the laser waveguide. A low threshold current density value is always desirable, indicating a high-quality laser material and a low loss fabricated waveguide. The typical value of the threshold current density of the ridge-waveguide laser diodes fabricated

from the laser material Sb307 in this work, as depicted in Fig. 3.14 (a), is 200 A/cm^2 (67 A/cm^2 per quantum well).

External differential quantum efficiency (η_d) is a figure of merit which indicates the efficiency of the laser diode in converting the injected current to photons emitted from the device. This quantity, calculated from Eq. 3.12, tells about the radiative and non-radiative recombination inside the laser structure as well as the loss of photons in the laser cavity [79].

$$\eta_d = 2\,\frac{\Delta P}{\Delta I}\left[\frac{q\lambda}{hc}\right] \qquad (3.12)$$

where $\Delta P/\Delta I$ is the slope of the P-I curve illustrated in Fig. 3.14 (a), P is the output power from each mirror facet, q is the elementary charge, λ is the emitting wavelength, h is Planck's constant and c is the speed of light. In this work, the typical value of the external differential quantum efficiency of a 1 mm long, 25 µm wide ridge-waveguide laser diode emitting at 2.33 µm wavelength at room temperature is 22.6 %, as calculated from Fig. 3.14 (a) and Eq. 3.12.

Internal quantum efficiency (η_i) is a parameter that measures the efficiency of the laser diode in converting the electron-hole pairs into photons within the laser diode structure. This quantity is independent of the geometry of the laser device and therefore is useful for comparison among the laser diodes.

Internal loss (α_i) is a parameter which corresponds to the loss of the optical wave in the laser waveguide. This quantity is particularly of interest in this thesis to characterize the performance of the S-bend and Y-junction lasers. The values of η_i and α_i can be found from the cavity length dependence of $1/\eta_d$ described in Eq. 3.13 (applicable for straight waveguide).

$$\frac{1}{\eta_d} = \frac{1}{\eta_i}\left[1 + \frac{\alpha_i}{\ln(1/R)}\,L\right] \qquad (3.13)$$

where L is the laser cavity length and R is the reflectivity of the laser facets. As shown in Fig. 3.14 (b), typical values of η_i and α_i of the ridge-waveguide laser diodes fabricated from the laser material Sb307 are 40.6 % and 9.83 cm^{-1}, respectively.

Characteristic temperature (T_0) is a parameter to measure the thermal sensitivity of the laser devices. This quantity can be obtained by experimentally measuring the P-I characteristic of a laser at different temperatures and being calculated by Eq. 3.14, as shown in Fig. 3.14 (c) and (d). A high value of T_0 implies that the laser is more thermally stable. The typical value of T_0 of the fabricated lasers in this work is 84.3 K, which is comparable to what is reported in the literature [8, 9, 11].

$$T_0 = \frac{\Delta T}{\Delta \ln(J_{th})} \qquad (3.14)$$

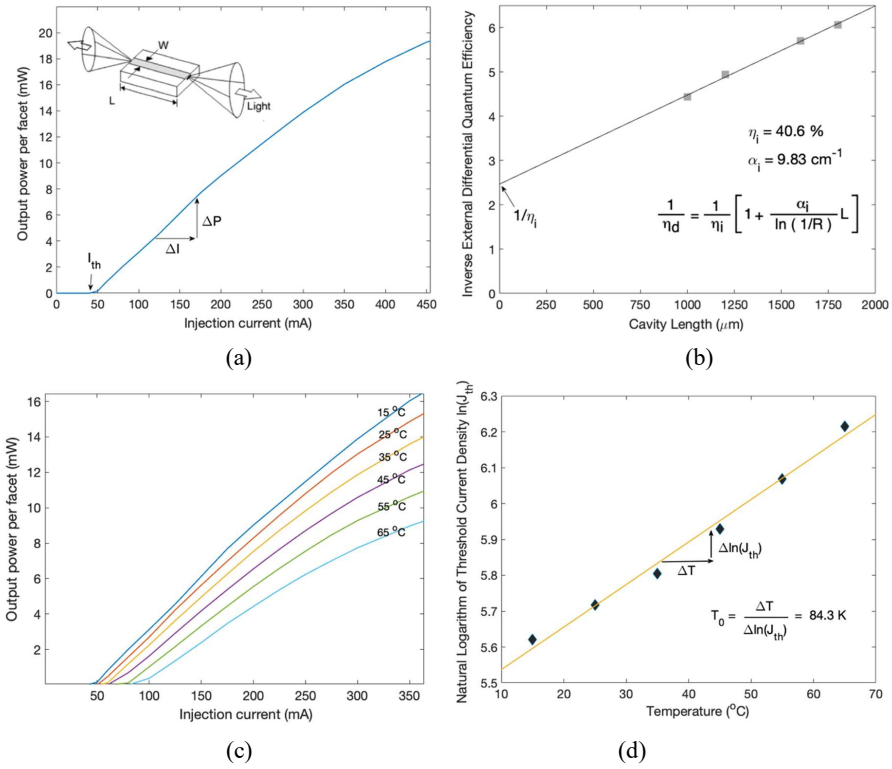

Figure 3.14: P-I characteristics of 25 μm wide ridge-waveguide laser diodes fabricated from laser sample Sb307. (a) P-I curve of a 1 mm long laser operating at 15 °C with a threshold current density of 200 A/cm^2 and an external differential quantum efficiency of 22.6%. The inset schematically shows a ridge-waveguide laser with cavity length L and waveguide width w. (b) The cavity length dependence of the inverse external differential quantum efficiency. The coefficients of the linear fit (straight line) to the set of data points are used to determine the internal quantum efficiency η_i and the internal loss α_i. (c) P-I curves of a 1 mm long laser operating at different temperatures. As the temperature increases, the performance of the laser diodes gets worse in term of output power, threshold current density and external differential quantum efficiency, which is attributed to the Auger recombination process [65]. (d) The variation of the threshold current density J_{th} with increasing temperature. The inverse of the slope of the linear fit (straight line) to the set of data points is the characteristic temperature T_0 of the laser diodes.

3.3.2. I-V measurements

The I-V characteristic of the laser diode determines its electrical properties. The obtained total resistance of the laser device is strongly attributed to the metal contacts, the p-i-n junction, the doping levels, and the sample thickness. Effects of the metal contacts and doping levels to the

laser I-V characteristics are investigated in section 5.4 and Patra's work [63]. For high performance laser diodes, a low voltage at the threshold current density and at operating current density is often desired to minimize the heat generation inside the laser structure. This is particularly important for mid-infrared semiconductor lasers operating at long wavelength. In this work, a low voltage of below 1 V at the threshold current density could be achieved, as depicted in Fig. 3.15, indicating high-quality grown laser structure and good metal contacts.

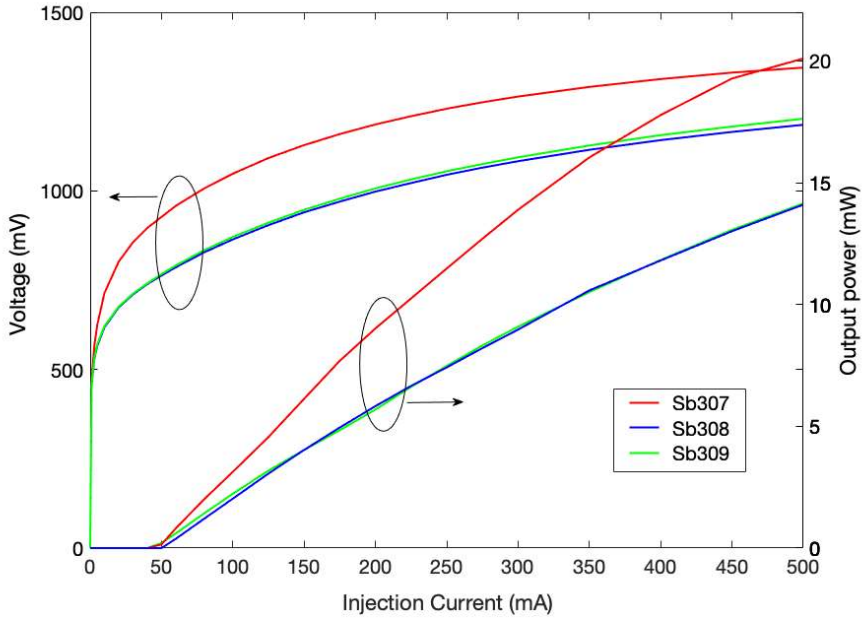

Figure 3.15: P-I and I-V characteristics of 1 mm long, 25 µm wide ridge-waveguide lasers fabricated from three different grown laser materials (Sb307, Sb308 and Sb309 – see details of grown laser structures in section 3.1.3 and in Appendix B). The laser materials Sb308 and Sb309 with high doping profile in the cladding layers show better I-V characteristic than that of the laser material Sb307.

3.3.3. Spectral measurements

The spectral measurements are crucial for lasers working as the light sources of TDLAS. The particular parameters of interest are wavelength, SMSR and FWHM, which can be extracted from the laser spectrum as shown in Fig. 3.16. To measure the laser spectrum, the laser light was coupled into a multimode optical fiber and guided to the FTIR spectrometer.

Wavelength For gas detection and optical communication applications, the wavelength of the laser source must be well-defined to match the assigned wavelength of the specific application. For example, in gas detection, the laser wavelength must match one of the

absorption lines of the gas to be detected. In the laser spectrum, the emitted wavelength corresponds to that of the dominating mode.

SMSR is defined as a photon density quotient of the dominating mode and the second most intense mode, usually given in logarithmic unit dB. This quantity determines the spectral purity of the laser source and is required as high as possible for single mode operation. For gas detection, SMSR values exceeding 20 dB is generally desirable [5].

FWHM is also an important parameter of the spectral characteristics. Even when a semiconductor laser diode operates in single mode behavior, the line width of the dominating mode can be broadened due the quantum fluctuation associated with the process of the spontaneous emission. For gas detection, the FWHM of the dominating mode should be smaller than that of the absorption line of the gases to be detected. Simulation results show that high accuracy gas detection can be achieved with a high spectral resolution of 0.1 nm FWHM [125].

Gain The dependence of gain on current and wavelength can be used to predict the performance of the laser diode below and above threshold condition. Below threshold, the gain can be used to determine the internal losses and also gives information about the diode behavior [126].

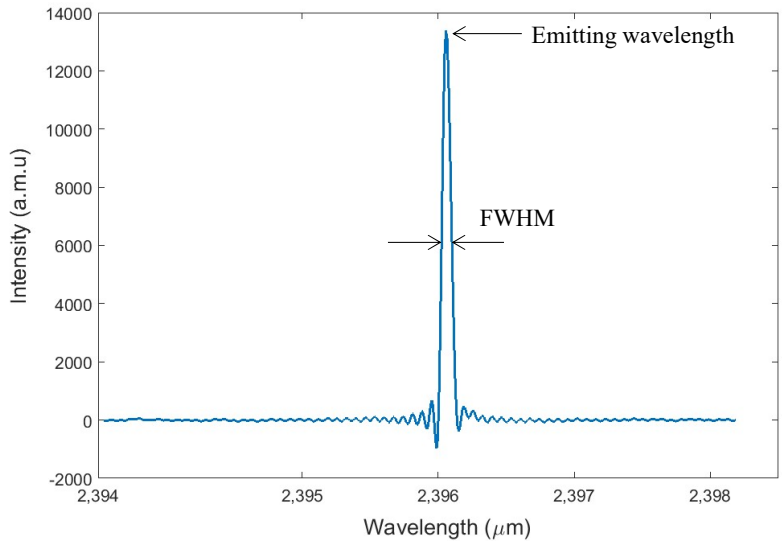

Figure 3.16: Spectral characteristics of a 5 µm wide straight waveguide laser diode: central wavelength λ_0 = 2.3961 µm, FWHM ~ 0.1 nm and SMSR ~ 14 dB.

3.3.4. Near- and far-field measurements

The measurements of laser near- and far-field provide the information about the profile and divergence of the laser beam.

Near-field is the spatial distribution of the emitted light near the laser facet. In general, several transverse and lateral modes may be excited and the resulting near-field is formed by the superposition of them. Single mode laser sources emit light in form of an elliptical spot of which the dimensions are strongly dependent on the optical confinement in transverse and lateral direction as mentioned in Chapter 2. Kinzer et al. [127] presents a method to image the near-field pattern of the quantum cascade lasers, and that is applied in this work.

Far-field is the angular intensity distribution far from the laser facet where the electro-magnetic wave-intensity pattern is essentially the same as the one observed at infinity. The far-field pattern indicates the angular spread of the laser mode and is important for coupling between the semiconductor laser and for example an optical fiber. In most cases, a laser source with low numerical aperture (NA) is desired. To measure the far-field pattern, an infrared camera was placed about 10 cm away from the laser facet.

In this work, the effects of etch depth to the beam profile and the far-field patterns were simulated and are presented in section 5.2. A measurement of near-field pattern of a 1 mm long FP laser is shown in Fig. 3.17. The far-field measurement, however, is difficult to achieve due to the interference inside the camera caused by an unwanted Fabry – Perot etalon [61], as shown in Fig. 3.18. One solution to measure accurately the far-field pattern of the laser diodes is using the scanning goniometric radiometer measurement technique [128] which is, however, not available at NTNU laboratories.

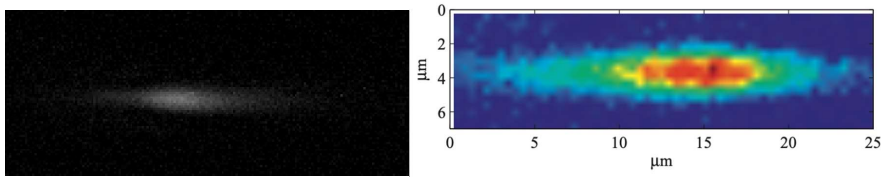

(a) (b)

Figure 3.17: Near-field pattern of a 1 mm long FP laser (a) as-captured by the infrared camera and (b) after visualizing by MATLAB [61].

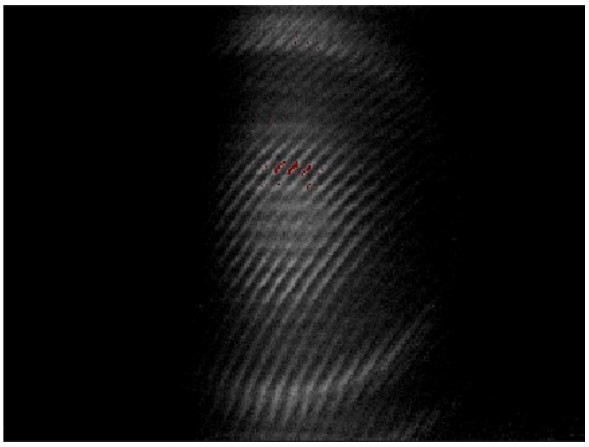

Figure 3.18: Far-field pattern of a 1 mm long FP laser overlapped by the interferometric ring pattern caused by an unwanted Fabry – Perot etalon inside the infrared camera.

3.4. Y-junction lasers – Fabrication and characterization

Fabrication and characterization of the tunable Y-junction lasers is the main goal of this thesis. In this work, Y-junction lasers of different configuration were fabricated and characterized following the procedure described in section 3.2, section 3.3 and in Appendix C. This section discusses several issues in the fabrication and characterization process of the Y-junction lasers. The output performance of Y-junction lasers in terms of emitted power, threshold current density, SMSR and wavelength tuning range is presented in section 5.5.

3.4.1. Mask design for Y-junction lasers

As mentioned in section 2.3.1, the Y-junction lasers consist of two FB cavities, a relatively straight and an S-bend cavity, sharing a common section. The geometrical length difference ΔL between these two cavities provides the basis for the interferometric tuning mechanism of the Y-junction lasers. In the asymmetric Y-junction structure, the bend radius r of the S-bend section, see Fig. 2. 9 (a), determines the length difference ΔL between two cavities for a given waveguide separation. The larger the bend radius, the smaller ΔL can be. In this work, a mask for Y-junction lasers with different bend radii of the S-bend cavities was designed for characterizing the characteristics of Y-junction lasers. Fig. 3.19 shows a part of this mask for Y-junction lasers of different configuration (i.e., different bend radii, waveguide widths, cavity lengths, and ΔL).

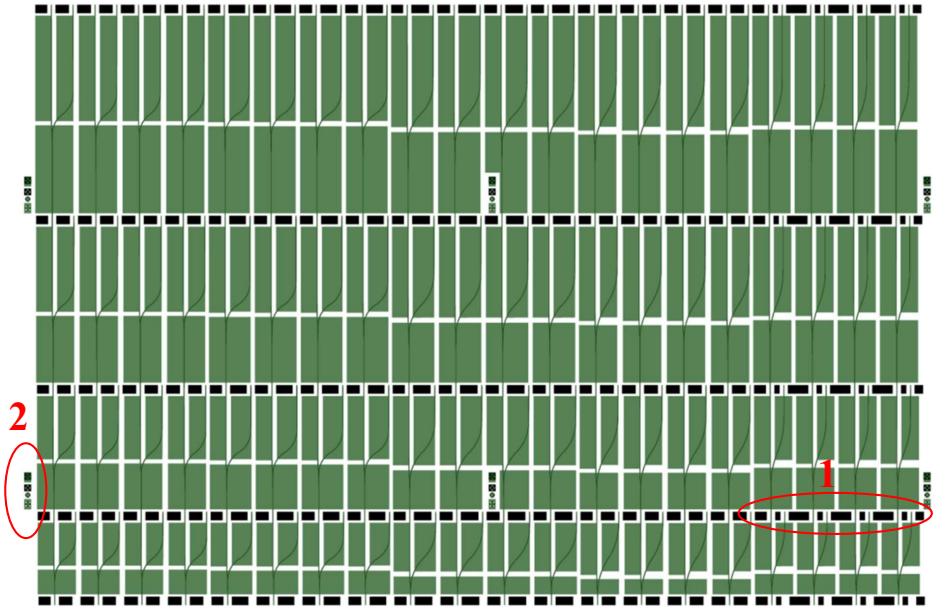

Figure 3.19: Part of mask for Y-junction laser. The black patterns were used for Y-junction waveguide formation, while the green patterns were used for top contact metallization. (The overlapping between black and green patterns are shown as dark green.) Design parameters: Cavity length L = (1.0, 1.5, 2.0, and 2.5) mm, waveguide width w = (1.5, 2.0 and 2.5) µm, bend radius r (µm) and ΔL (µm) (from left): 4 × ($r300\Delta L80$, $r300\Delta L100$, $r500\Delta L80$, $r750\Delta L50$ and $r1000\Delta L20$). Some special structures were also added to the mask: (1) support structures, (2) alignment mark.

3.4.2. Fabrication of Y-junction lasers

As the light beam propagates inside the Y-junction waveguide structure, the Y-junction is considered as a beam splitter, thus requires sharp corner to reduce the propagation loss. By applying the EBR technique, a sharp Y-junction photoresist pattern can be achieved as shown in Fig. 3.20 (a). However, the sharp corner of the Y-junction becomes rounded after the ICP-RIE process, as illustrated in Fig. 3.20 (b). This is attributed to the substantial increase of the overall ion current at the Y-junction due the edge-related effect of the plasma-surface interaction [129]. The rounded edge can become a contributing factor to the optical loss of the Y-junction waveguide.

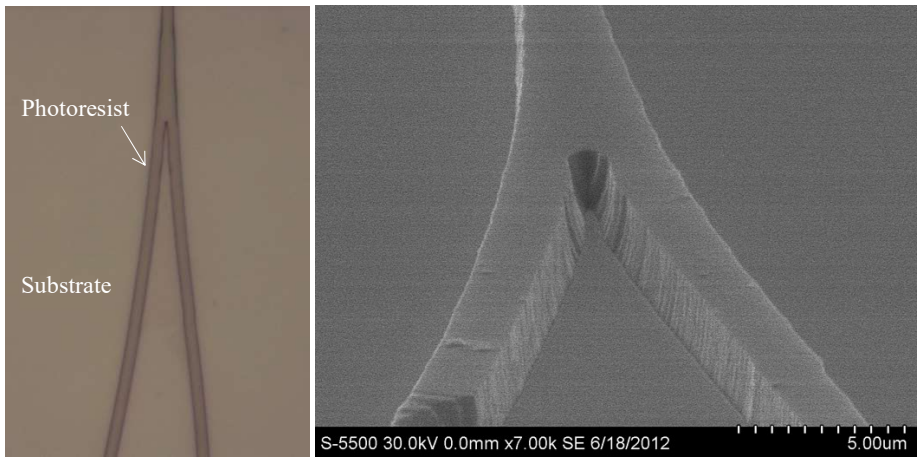

(a) (b)

Figure 3.20: (a) An image taken by optical microscopy of a sharp Y-junction photoresist pattern after the photolithography step for waveguide formation. (b) An as-etched Y-junction waveguide with a rounded Y corner and slightly rough sidewalls.

Another factor which could contribute to the internal loss of the Y-junction waveguide structure is the roughness of waveguide sidewalls, as shown in Fig. 3.20 (b). The sidewall roughness results from a replication of the initial morphology of the resist mask, which is not perfectly smooth due to light scattering during the photolithography process. According to simulation performed by Magnus Breivik [61], the waveguide sidewall roughness can significantly affect the propagation of light inside the Y-junction waveguide if its value is in the order of 1 μm but has little impact if its value is less than 100 nm. Based on the length scale bar in Fig. 3.20 (b), the sidewall roughness is estimated to be in the range of 100 to 200 nm, which can slightly affect the light propagation in the Y-junction waveguide. Note that the sidewall roughness could not be determined precisely due to the difficult approach of Atomic Force Microscopy (AFM) method.

After etching, the Y-junction waveguide was isolated by spin-coated photoresist followed by thermal hardening and O_2/CF_4 RIE etchback to provide a planar surface for the top contact metallization. The top metal contact is required to be well-aligned with the waveguide structure to provide the best contact for current injection. Thanks to the use of alignment marks on the mask, the top contact metallization was well-aligned with the Y-junction waveguides, as illustrated in Fig. 3.21. As seen in Fig. 3.21 (b), the gap separation between contact pads were well-defined to ensure the different current injections to different parts of the Y-junction laser for characterizing its tuning behavior.

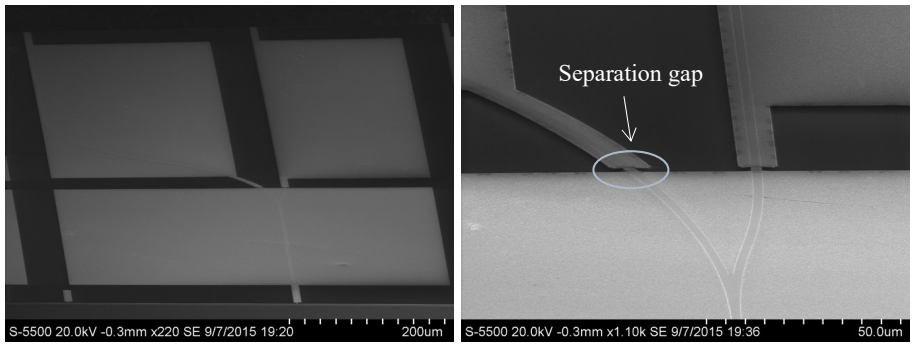

(a) (b)

Figure 3.21: Y-junction waveguide underneath top contact metal pads. (a) A top view. (b) A close view of the Y-junction and the separation gap between three different contact pads.

3.4.3. Characterization of Y-junction lasers

Fig. 3.22 shows the measurement setup for characterizing the tuning behavior of Y-junction lasers. Probes connected to different current drivers were placed onto metal pads to provide different current injections to different parts of the device. Here, the probing technique was chosen instead of the wire bonding technique in order to avoid the damage to Y-junction lasers during the wire-bonding process. The output light emission from the common section facet was coupled into a multimode optical fiber and was guided into an FTIR spectrometer for spectral measurements. Note that it is important to precisely couple the output emitting light of the lasers into the core of the optical fiber. This task can be difficult because the diameter of the core is much smaller than that of the optical fiber. Thus, the optical fiber core was exposed to the air by removing the outer layers of the optical fiber and was carefully placed in front of the common section facet to obtain an efficient light coupling, as shown in Fig. 3.22. To measure the P-I characteristics of Y-junction lasers, the optical fiber was replaced by a power meter.

To characterize the tuning behavior of Y-junction lasers, a large combination of different injected currents (i.e., I_l, I_c and I_s) was applied. Different sets of voltages (corresponding to different sets of injected currents) were programmed on a computer using Labview, and were sent to the NI-9263 DAC. The output voltages of the NI-9263 DAC were used as inputs for the current drivers to control the injected currents to the three different parts of the Y-junction lasers. After each set of injected currents was applied, the spectral measurement was performed by FTIR from which the emitting wavelength and the SMSR were extracted.

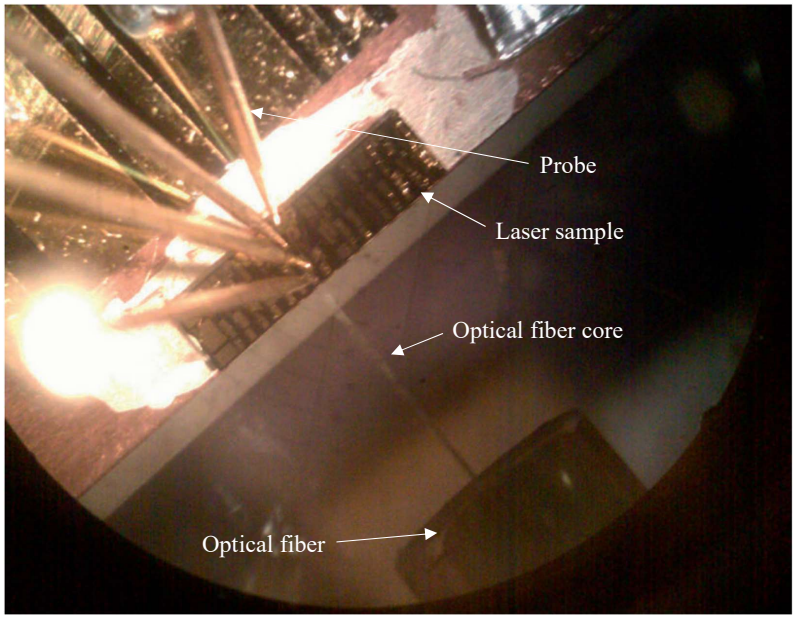

Figure 3.22: The measurement setup for characterization of tuning behavior of Y-junction lasers. This image was taken by a conventional camera through the optical microscopy by Breivik [61].

Chapter 4

FACET COATING FOR HIGH PERFORMANCE LASERS

Optical coatings have been widely used for a variety of optical and electro-optical applications in telecommunication, medicine, military and consumer products. By coating optical devices with different thin film materials, either single layer coating or multiple-layer coating, an interference effect can be created to enhance transmission or reflection properties of the optical systems. In laser optics, this method plays a key role to improve the output performance and stability of the laser devices.

According to Eq. 2.9, the mirror loss depends on the reflectivity of the laser facets. The facet reflectivity can be modified by optical coatings for improvement of laser characteristics in terms of output power, threshold current, differential quantum efficiency and operational reliability. The most common types of coating in laser optics are anti-reflection (AR) coating and high-reflection (HR) coating. The optical coatings can also protect the laser facet against catastrophic optical mirror damage (COMD), thus enhance the long-term stability of the devices. COMD is a dominant laser failure mechanism in high-power semiconductor lasers, occurring when the semiconductor laser facets generate much heat due to absorption and non-radiative recombination at high injected current. The heat will accelerate the degradation of the laser facet that leads to COMD. The typical values for COMD threshold power per aperture width are in the range of hundred mW/μm [130], which is far beyond the maximum output power of mid-IR semiconductor lasers [131]. Facet protection against oxidation, however, is crucial for the long-term stability of mid-IR GaSb-based laser diodes, especially when taking account of the reactive nature of AlGaAsSb, which is used for cladding layers and SCL, as mentioned in chapter 3.

4.1. Theory

The reflection and transmission of light through optical coating layers rely on the principles of interference. Light, that has passed vertically through a horizontal film and is reflected at the lower interface, interferes with the light reflected from the surface of the layer. When their phases match, they will combine and create larger total amplitude. This is known as constructive interference. On the other hand, when the beams are out of phase, their combination can result in a subtractive effect known as destructive interference, thus reducing the total amplitude as compared to the original waves.

The reflectance of light emitted from the laser active region through a stack of optical coating layers deposited on the laser facet can be calculated by the matrix method [132]. Assume that laser output emitted at the wavelength λ_0 with the field amplitude E_0 is incident normally on the stack of optical coating layers as shown in Fig. 4.1.

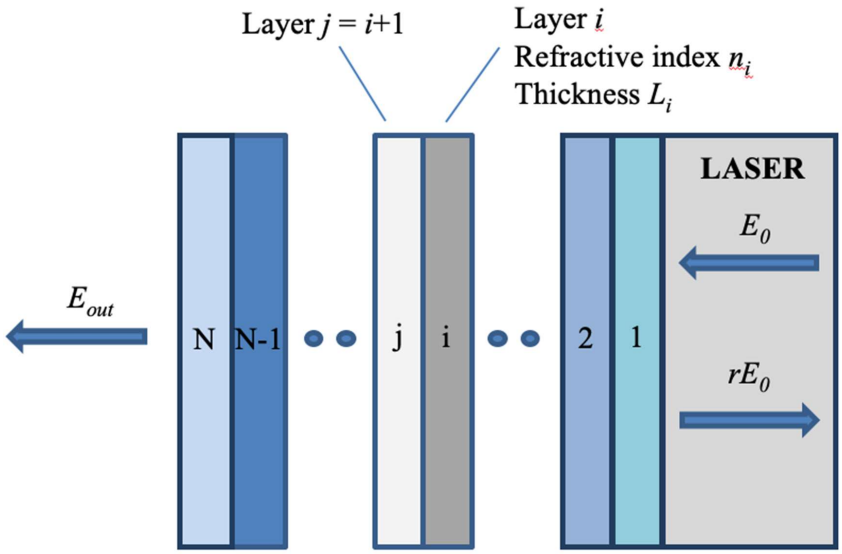

Figure 4.1: Laser light propagates through a multi-layer coating deposited on the laser facet. Layer i has refractive index n_i and thickness L_i.

When propagating through a layer i, the light suffers a propagation process within the layer and a transition process at the interface between layer i and j where j=i+1. These events are represented by the propagation matrix P_i and the transition matrix T_{ij} given by

$$P_i = \begin{bmatrix} v_i \, exp\left(i\frac{2\pi}{\lambda_0} n_i L_i\right) & 0 \\ 0 & \frac{1}{v_i} \, exp\left(-i\frac{2\pi}{\lambda_0} n_i L_i\right) \end{bmatrix} \quad (4.1)$$

$$T_{ij} = \frac{1}{t_{ij}} \begin{bmatrix} 1 & -r_{ij} \\ -r_{ij} & 1 \end{bmatrix} \quad (4.2)$$

where v is the loss factor, n is the layer refractive index, L is the layer thickness, and r and t are reflectance and transmission coefficients, respectively. The whole propagation process of the laser light through the stack of optical coating layers can be summarized in the following equation

$$\begin{bmatrix} rE_0 \\ E_0 \end{bmatrix} = T_{01}P_1 \dots T_{(N-1)N}P_N T_{N(N+1)} \begin{bmatrix} 0 \\ E_{out} \end{bmatrix} = S \begin{bmatrix} 0 \\ E_{out} \end{bmatrix} \quad (4.3)$$

where $n_0 = n_{laser}$, $n_{N+1} = n_{air}$ and S is the stack matrix.

The reflectance of the optical coatings is given by [132]

$$R = rr^* = \left|\frac{S_{12}}{S_{22}}\right|^2 \quad (4.4)$$

The basic building block for optical coating is the quarter-wavelength optical thickness (QWOT) layer where

$$L_i = \frac{\lambda_0}{4n_i(\lambda_0)} \quad (4.5)$$

where λ_0 is the light wavelength and $n_i(\lambda_0)$ is the refractive index of layer i at the wavelength of λ_0. With QWOT, the reflectance for a single layer coating will be [132]

$$R = \frac{(n_1^2 - n_{laser}n_{air})^2}{(n_1^2 + n_{laser}n_{air})^2} \quad (4.6)$$

In the case of AR coating, the reflectance vanishes to zero, yielding the refractive index of the required material

$$n_1 = \sqrt{n_{laser}n_{air}} \quad (4.7)$$

In practice, multi-layer coatings of alternating QWOT layers of two coating materials, a high index (n_H) material and a low index (n_L) material, are usually used in optical coating applications. For an N-dual-layer stack of high and low index materials, the reflectance of the optical coating is [132]

$$R = \frac{(n_L^N n_{air} - n_{laser}n_H^N)^2}{(n_L^N n_{air} + n_{laser}n_H^N)^2} \quad (4.8)$$

4.2. Simulations and experiments

In this work, optical coatings were investigated for optimization of laser performance. Three different types of coatings were chosen, including AR coating, HR coating and partial HR coating. The coatings were firstly simulated by MATLAB for material selection and reflectance optimization at the desired emission wavelength of 2.33 μm. The required materials must be optically suitable and be compatible with the laser processing. The latter requirement is

regarding physical properties of materials such as being dielectric, and having low absorption, good adhesion and high compatibility to the deposition method. The optimized coatings selected from simulation results were deposited on glass and on GaAs substrate using electron beam deposition, of which glass substrate is used for testing the deposition method and GaAs has the refractive index closest to those of the laser materials [61]. Although ion beam sputtered deposition technique is preferable for optical coatings [132, 133], the electron beam deposition technique was chosen in this work due to a high deposition rate and limitations with the ion beam sputtering system in the processing lab at the time. The reflectance spectra of the optical coatings were then measured by FTIR spectroscopy to compare with simulation results. Finally, different optical coatings were applied on laser facets to improve the laser characteristics. In this section, the simulation and experimental results were obtained from the work of a master student, Olav Myrvang, under my supervision [134].

4.2.1. Optical coating

4.2.1.1. AR coating

The application of AR coatings in the semiconductor industry has been widely investigated for over 30 years. AR coatings are used in a wide variety of optoelectronic devices such as superluminescent diodes, composite-cavity lasers, and distributed feedback lasers. By applying an AR coating on one of the laser facets, the optical output power is enhanced significantly, thus increasing the overall efficiency of the devices.

An AR coating consists typically of either a single layer coating or dual layer coatings. In the case of a single layer coating, the required refractive index of the material is given by Eq. 4.7. For mid-IR semiconductor lasers, this value typically lies between 1.7 and 2 depending on the emission wavelength. In practice, the performance of a single layer coating is limited by the narrow transmission band and the not-very-low reflectance.

On the other hand, the dual layer coating is more flexible in the design of the AR coating. It can yield broad reflection bands owing to the large difference in refractive indices between two layer materials. A very low reflectance due to maximum destructive interference can be achieved by optimizing materials, layer thickness and number of dual layers. TiO_2-SiO_2, one of the most widely used dual layer coatings, was chosen in this work. One dual layer of TiO_2 and SiO_2 with QWOT was used for our simulation and experiments. Fig. 4.2 shows the transmittance spectra of this dual coating on glass and on GaAs substrate in comparison to simulation results. The experimental transmittance spectrum of the AR coating on GaAs substrate shows the broad U shape with a reflectance of less than 7 % at the desired wavelength of 2.33 μm. There are several reasons that lead to the difficulty in achieving very low reflectance. The most important reason is that the refractive index of TiO_2 is hard to control and does not fit with the simulation. In order to achieve the required refractive index, the TiO_2 thin film needs to be annealed at high temperature [135, 136], above 300 °C, which is not compatible with the laser fabrication process. The results, however, are acceptable in the scope of this work.

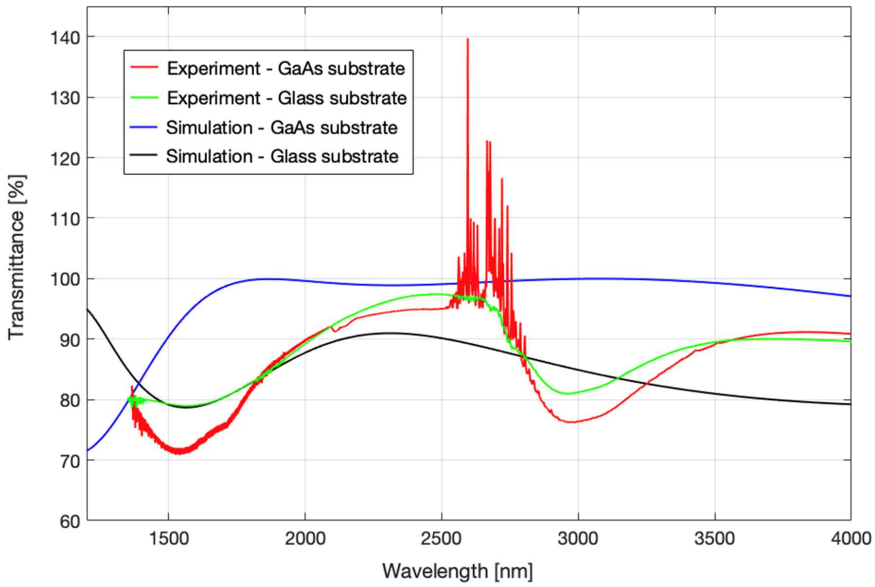

Figure 4.2: Experimental and simulated transmittance spectra of one dual layer (TiO_2-SiO_2) AR coating on glass and on GaAs substrate.

4.2.1.2. HR coating

For high performance of the semiconductor laser diode, it is desirable to maximize output power at one of the laser facets while blocking light at the other facet by HR coating. By reducing the mirror loss, the HR coating helps reduce the threshold current and increase the differential quantum efficiency of the lasers. For long-wavelength semiconductor lasers, increasing mirror reflectivity allows reduction of the cavity length, thus minimizing the heat generation in the laser structures. It is critical to reduce Auger recombination, which is the dominant nonradiative recombination processes that can significantly affect the performance of long-wavelength semiconductor lasers [65]. Moreover, reducing cavity length increases the longitudinal mode spacing and makes it easier to achieve single mode Fabry-Perot lasers.

HR coating is relatively easy to design. It consists of a stack of alternating high (H) and low (L) refractive index materials with QWOT. The number of dual layers (N) of high and low refractive index materials required to achieve high reflectance depends on the difference in their refractive indices. The design therefore is substrate / (L/ H) ^ N / air. In this work, a stack of 6 dual layers (L/H) of SiO_2-Ge was fabricated and characterized for the HR coating, of which SiO_2 is the low refractive index material and Ge is the high refractive index material. The experimental and simulated transmittance spectra of such a stack on both glass and GaAs substrate are depicted in Fig. 4.3. The experimental and simulated spectra are similar. The experimental reflectance of the HR coating on GaAs substrate at the desired wavelength of 2.33 µm is 99%, satisfying the goal of this work.

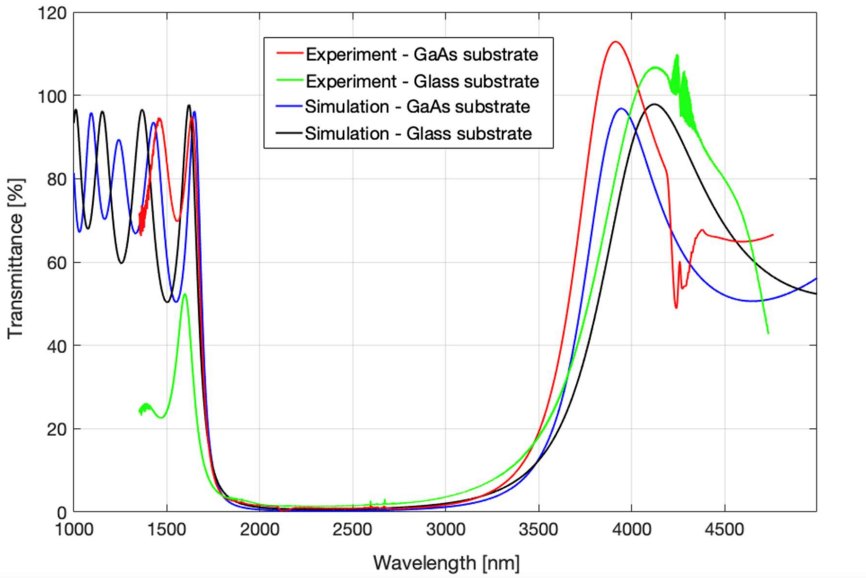

Figure 4.3: Experimental and simulated transmittance spectra of six dual layer (SiO_2-Ge) HR coating on glass and on GaAs substrate.

4.2.1.3. Partial HR coating

There are several applications requiring a controlled level of facet reflectivity, usually to optimize the resonance in the laser cavity. One example is partial HR coating which usually is used in beam-splitter applications [137]. The required reflectance for such coatings is 50 %. In this work, a single QWOT dual layer of SiO_2 and Ge was fabricated and characterized for the partial HR coating. Fig. 4.4 shows the transmittance spectra of this partial HR coating on glass and on GaAs substrate in comparison to simulation results. The experimental results show a fairly good agreement with those of simulation works in terms of the shape of the curvature, however, having a difference of up to 15% reflectance between the results in the wavelength range of 1500 – 3000 nm. This reflects the fact that it is hard to control the reflectance of the dual layer partial HR coating, which requires a proper thickness combination of each individual layer [138]. As seen in Fig. 4.4, the experimentally determined reflectance at the desired wavelength of 2.33 µm of the partial HR coating on glass and on GaAs substrate is 50 ± 5 %.

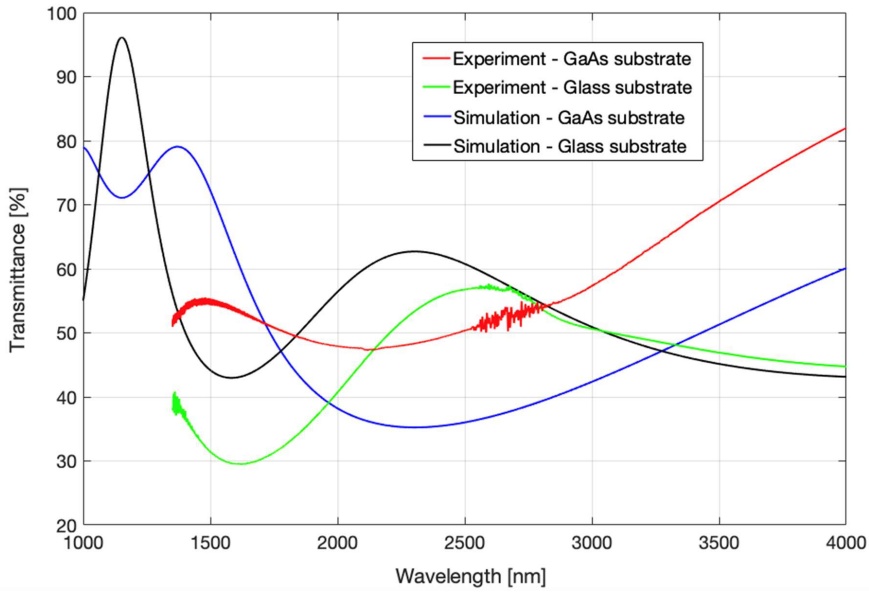

Figure 4.4: Experimental and simulated transmittance spectra of one dual layer (SiO_2-Ge) partial HR coating on glass and on GaAs substrate.

4.2.2. Optical coating on laser facets

4.2.2.1. Experiments

Ridge-waveguide lasers with 25 µm wide strips were processed using laser material sample Sb159, emitting at 2.23 µm, following the procedure described in chapter 3. The sample Sb159 (see Appendix B for the detailed growth structure) was chosen to test the optical coating on laser facets, since the experimental results for the GaAs substrate at 2.23 and 2.33 µm were similar, as shown in Fig. 4.2 – 4.4. The thicknesses of the optical coatings for the laser material Sb159 were adjusted to match the 2.23 µm emission wavelength.

The final lasers were cleaved into 1.5 mm long laser bars. For optical coating on laser facets, the laser bars were sandwiched between two pieces of Si using photoresist as the adhesive as follows: Si / Photoresist / Laser / Photoresist / Si. This was to protect the top and bottom contacts from deposition of dielectric materials. This stack was mounted on a special holder made for the e-beam evaporation process. No treatment was applied to remove the oxide on the laser facet. Three different lasers with different facet coatings, as summarized in Tab. 4.1, were fabricated to investigate the effect of optical coating on the laser performance in comparison with the uncoated reference laser sample. The lasers were mounted episide-up on copper heat sinks and characterized in continuous wave operation at 15 °C.

Table 4.1: Lasers with four different facet coating combinations.

Laser	Facet 1	Facet 2
1 (Reference)	Uncoated	Uncoated
2	HR coating	Uncoated
3	HR coating	AR coating
4	HR coating	Partial HR coating

4.2.2.2. Laser characterizations

To characterize the effect of different facet coatings on the laser performance, P-I measurements were performed on five lasers of each facet coating combination of the fabricated lasers. The results, including mean value and standard deviation, are summarized in Tab. 4.2. Fig. 4.5 shows the P-I curves for representative lasers of each facet coating combination.

Table 4.2: P-I characteristics (mean value ± one standard deviation) of the fabricated lasers with different facet coatings.

Laser	Estimated mirror loss (cm^{-1})	Threshold current (mA)	Max output power (mW)	External differential quantum efficiency η_d (%)
1	8.03	112 ± 15.5	16.5 ± 2.8	11.94 ± 0.42
2	4.01	101 ± 6.6	23.9 ± 1.5	15.89 ± 1.03
3	8.86	131.6 ± 1.1	31.1 ± 1.7	28.64 ± 0.88
4	2.31	102 ± 8.4	4.0 ± 0.5	3.26 ± 0.76

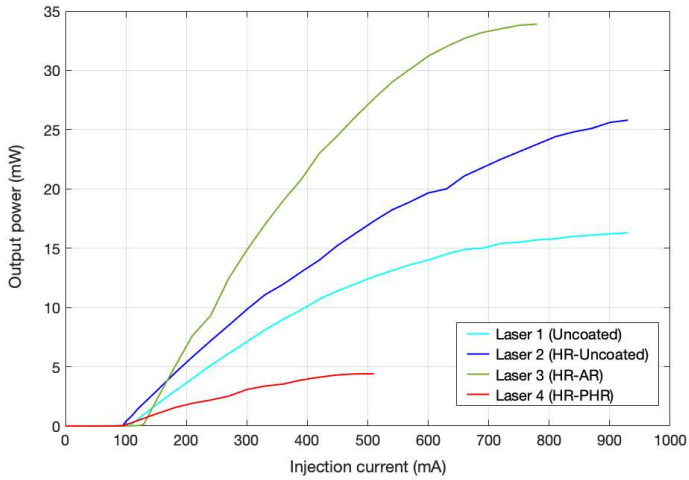

Figure 4.5: Light – current characteristics of representative laser diodes with different facet coatings.

By reducing the mirror loss by a factor of two with the HR coating, laser 2 shows significant improvement in terms of threshold current and output power compared to the uncoated reference laser (laser 1). On the other hand, the combination of AR coating and HR coating deposited on facets of laser 3 slightly increases the threshold current of the laser diodes due to the higher mirror loss. However, significant increase of the output power and the overall efficiency of the device is observed, as expected. We note that the performance of laser 4 is worse than the uncoated reference laser, with lower output power and lower differential quantum efficiency. This is attributed to the heat generation inside the laser structures since the light is heavily trapped between the laser facets. When the laser structures become “hot”, the Auger recombination increases, which results in the reduction of light emission from the lasers [139].

Chapter 5

PUBLICATIONS

5.1. Paper 1 - Dopant incorporation in doped $Al_{0.9}Ga_{0.1}As_{0.06}Sb_{0.94}$ grown by molecular beam epitaxy

Authors: Saroj Kumar Patra, **Thanh-Nam Tran**, Lasse Vines, Ilia Kolevatov, Edouard Monakhov and Bjørn-Ove Fimland

First published in: Journal of Crystal Growth, Vol. 463, p. 116-122 (2017)

DOI: 10.1016/j.jcrysgro.2017.01.035

Contributions: SKP planned the study under supervision of BOF. SKP performed the experimental works related to epitaxial growth of doped samples, characterization using X-ray diffraction measurements and Hall effect measurements. **TNT** performed the fabrication of Hall bar and DLTS structures. LV performed the SIMS measurements and IK performed the DLTS measurements. SKP drafted the first version of the manuscript and finalized it after input from all co-authors. All co-authors participated in discussions related to results and manuscript.

Abstract

Incorporation of beryllium (Be) and tellurium (Te) dopants in epitaxially grown $Al_{0.9}Ga_{0.1}As_{0.06}Sb_{0.94}$ layers was investigated. Carrier concentrations and mobilities of the doped layers were obtained from room temperature Hall effect measurements, and dopant densities from secondary ion mass spectrometry depth profiling. An undoped $Al_{0.3}Ga_{0.7}As$ cap layer and side wall passivation were used to reduce oxidation and improve accuracy in Hall effect measurements. The measurements on Be-doped samples revealed high doping efficiency and the carrier concentration varied linearly with dopant density up to the highest Be-dopant density of 2.9×10^{19} cm^{-3}, whereas for Te-doped samples the doping efficiency was in general low and the carrier concentration saturated for Te-dopant densities above 8.0×10^{18} cm^{-3}. The low doping efficiency in Te-doped $Al_{0.9}Ga_{0.1}As_{0.06}Sb_{0.94}$ layer was studied by deep-level transient spectroscopy, revealing existence of deep trap levels and related DX-centers which explains the low doping efficiency.

I. INTRODUCTION

Mid-infrared lasers emitting in the 2-3 μm wavelength range are very important for trace gas sensing using tunable diode-laser absorption spectroscopy (TDLAS) [1]. GaSb-based III-V semiconductor quantum well diode lasers cover this particular wavelength range. CH_4 has a very strong absorption line at 2.3 μm wavelength, and therefore GaInAsSb/AlGaAsSb-based lasers emitting at that particular wavelength are of high interest [2]. For such diode lasers, $Al_{0.9}Ga_{0.1}As_ySb_{1-y}$ lattice-matched to GaSb is used as cladding layers [2-4]. Lattice-matching at growth temperature, i.e. $Al_{0.9}Ga_{0.1}As_{0.06}Sb_{0.94}$, is preferred to have dislocation free layers [3]. Te and Be are used as n-type dopant and p-type dopant, respectively, in the cladding layers. Characteristics of these diode lasers are dependent on parameters used during growth of laser materials and fabrication of diode lasers. For example, composition, thickness and strain in the quantum wells and barriers affect the emission wavelength of the diode laser [2]. The resistance and threshold current density of the diode depend strongly on the carrier concentration in the cladding layers and the thickness of the undoped core. Increase in resistance gives rise to heating, which leads to increase in Auger loss [5] and thus reduction in laser output power. Therefore, the output power of the laser depends on the doping in the cladding layers. Optimization of the output power of the diode laser requires calibrations of incorporated dopant density and corresponding carrier concentration in the cladding layers. However, there has been limited work reported on the dopant incorporation in AlGaAsSb [6-8].

In this paper, we present new data on carrier concentration versus dopant incorporation in $Al_{0.9}Ga_{0.1}As_{0.06}Sb_{0.94}$ layers grown by molecular beam epitaxy (MBE). A number of Be- and Te-doped $Al_{0.9}Ga_{0.1}As_{0.06}Sb_{0.94}$ layers were grown on undoped GaAs(001) substrates, using different Be and GaTe source temperatures. A 100 nm thick undoped $Al_{0.3}Ga_{0.7}As$ cap layer was grown on top of the doped $Al_{0.9}Ga_{0.1}As_{0.06}Sb_{0.94}$ layer to reduce oxidation and errors in Hall effect measurements. Carrier concentrations and Hall mobilities of the doped $Al_{0.9}Ga_{0.1}As_{0.06}Sb_{0.94}$ layers were obtained from room temperature Hall effect measurements for different Be and Te dopant densities, as measured by secondary ion mass spectrometry

(SIMS) depth profiling. Deep-level transient spectroscopy (DLTS) was performed on $Al_{0.9}Ga_{0.1}As_{0.06}Sb_{0.94}$/GaSb diodes to study the low doping efficiency in Te-doped cladding layers. The low doping efficiency can be explained by the existence of acceptor-like DX-centers due to deep level defects.

II. EXPERIMENTAL

1. Material growth

Two different types of test structures were grown in a Varian GEN II Modular MBE system equipped with Te and Be dopant furnaces, an Al dual crucible furnace, a Ga dual filament furnace, and Veeco As and Sb valved cracker furnaces. GaTe and Be sources were outgassed for 30 min at a temperature 20 ºC higher than the maximum used temperature and stabilized at the required temperature prior to growth.

The first type of test structures, for Hall effect and SIMS measurements, were grown at 520 ºC on epi-ready undoped GaAs(001) 2" quarter wafers. Prior to growth, native oxide was desorbed at 585 ºC followed by wafer annealing at 610 ºC for 15 min under an As_2 pressure of 1.0×10^{-6} Torr. 2 µm thick doped $Al_{0.9}Ga_{0.1}As_{0.06}Sb_{0.94}$ layer followed by a 100 nm thick undoped $Al_{0.3}Ga_{0.7}As$ cap layer were grown at 1 ML/sec growth rate. $Al_{0.3}Ga_{0.7}As$ was chosen as the cap layer in order to prevent both oxidation of the doped $Al_{0.9}Ga_{0.1}As_{0.06}Sb_{0.94}$ layer as well as formation of a conducting 2-dimensional sheet at the interface between the doped $Al_{0.9}Ga_{0.1}As_{0.06}Sb_{0.94}$ layer and the undoped cap layer. $Al_{0.3}Ga_{0.7}As$ has an appropriate band gap and band gap alignment with respect to the doped $Al_{0.9}Ga_{0.1}As_{0.06}Sb_{0.94}$ layer for our experiment. Ten Be-doped $Al_{0.9}Ga_{0.1}As_{0.06}Sb_{0.94}$ samples with different Be source temperature (925 – 1150 ºC) and seven Te-doped $Al_{0.9}Ga_{0.1}As_{0.06}Sb_{0.94}$ samples with different GaTe source temperature (415 – 495 ºC) were grown.

The second type of test structures, for DLTS measurements, were grown at 520 ºC on epi-ready n-type (Te) doped GaSb(001) 2" quarter wafers. Native oxide desorption and wafer annealing prior to growth were performed at 550 ºC under an Sb_2 pressure of 1.3×10^{-6} Torr. 1 µm thick Te-doped $Al_{0.9}Ga_{0.1}As_{0.06}Sb_{0.94}$ layer followed by a 100 nm thick Be-doped GaSb layer were grown at a growth rate of 1 ML/s. Three samples with different Te-doping in the $Al_{0.9}Ga_{0.1}As_{0.06}Sb_{0.94}$ layer and fixed Be-doping in the GaSb layer were grown as summarized in Table 1.

Table 1. Be-doped GaSb/Te-doped $Al_{0.9}Ga_{0.1}As_{0.06}Sb_{0.94}$ PN-diode samples for DLTS measurements. Listed dopant densities are based on experimental SIMS data.

Sample ID	Be dopant density in GaSb (cm^{-3})	Te dopant density in $Al_{0.9}Ga_{0.1}As_{0.06}Sb_{0.94}$ (cm^{-3})
Sb 284	5.0×10^{18}	3.0×10^{18}
Sb 285	5.0×10^{18}	2.0×10^{18}
Sb 286	5.0×10^{18}	1.0×10^{18}

2. Device fabrication

Hall bar samples with six-contact 1-2-2-1 geometry were fabricated from the first type of test structures. Pattern for six metal contact pads were created by conventional photolithography using the photoresist ma-N 440. Prior to metallization, the surface oxide layer was removed by wet chemical etching using NH_4OH:H_2O_2:H_2O (1:1:200) for 30 s and NH_4OH: H_2O (1:30) for 1 min. 1.5 µm thick Au layer was deposited using an e-beam metal deposition system followed by a metal lift-off in acetone for ~10 min to define the contact pads. The Hall bar was defined by a second photolithography process followed by a wet chemical etching with etch depth of 3 µm using citric acid (2.5M):H_2O_2:H_2O (1:1:20) for 90 s. To prevent oxidation of the sidewall of Hall bar samples, photoresist ma-N 440 was used as passivation layer. Rapid thermal annealing (RTA) of the Au contacts at 400 ^oC for 20 s lead to the diffusion of Au through the $Al_{0.3}Ga_{0.7}As$ cap layer, as confirmed from energy-dispersive X-ray (EDX) analysis (micrographs not shown), and form ohmic contact to the doped $Al_{0.9}Ga_{0.1}As_{0.06}Sb_{0.94}$ layer. The final contacts to the Hall bar samples were performed by wire bonding to a printed circuit board using Au wire.

Be-doped GaSb/ Te-doped $Al_{0.9}Ga_{0.1}As_{0.06}Sb_{0.94}$ PN junction diodes were fabricated from the second type of test structures for DLTS measurements. 800 µm × 800 µm patterns for metal contact pads were created on the front side (i.e. Be-doped GaSb) of the sample using conventional photolithography. Prior to metallization, GaSb surface oxide was removed *in situ* by Ar sputtering at 325 eV in the combined sputtering and e-beam evaporation system (AJA ATC-2200V) [9]. A Ti/Pt/Au (50 nm/25 nm/ 325 nm) metal stack was deposited using e-beam metal deposition followed by a metal lift-off by acetone to define front contact pads. Using a photoresist mask covering the front contact pads, the diode structures were defined by dry etching using BCl_3 to an etch depth of 3 µm (i.e. etching into the Te-doped GaSb substrate). A sidewall-passivation layer was formed using photoresist to prevent surface oxidation. A Pd/Ge/Au/Pt/Au (8.7 nm/56 nm/23.3 nm/47.6 nm/200 nm) metal stack [10] was deposited on the back side of the sample to form an ohmic bottom contact. The metal contacts were annealed at 290 ^oC for 45 s using RTA.

3. Characterization

Carrier concentration and Hall mobility for the doped $Al_{0.9}Ga_{0.1}As_{0.06}Sb_{0.94}$ samples were measured using a Lakeshore 7504 Hall effect electronic transport measurement system. Room temperature Hall effect measurements were performed with varying magnetic field from 0 T to 0.5 T in both directions.

SIMS measurements were employed using a Cameca IMS7f microanalyzer. Depth profiles for Te-doped $Al_{0.9}Ga_{0.1}As_{0.06}Sb_{0.94}$ samples were obtained using 15 keV Cs^+ ions as primary beam; depth profiles for Be-doped $Al_{0.9}Ga_{0.1}As_{0.06}Sb_{0.94}$ samples were obtained using 10 keV O_2^+ ions as primary beam. For Cs^+ primary beam, ^{27}Al, ^{69}Ga, ^{75}As, ^{121}Sb and ^{128}Te of the secondary species were monitored. ^{128}Te was used since it appeared to have the least interferences with respect to species/molecules with similar mass, or mass to charge ratio, based on mass spectra taken from different samples. For O_2^+ primary beam, ^{9}Be, ^{75}As and $^{71}Ga_2$ were monitored. The $^{71}Ga_2$ molecule was used to monitor the matrix as the signal from single ^{71}Ga was too strong. Crater depths were measured with a Dektak 8 stylus profilometer, and a constant erosion rate was assumed when converting sputtering time to sample depth. From measuring the depths of several craters, an average sputter rate of 2.1 nm/second was found for both of the primary beams, and this sputter rate is assumed for all presented depth profiles for Be and Te. Concentration calibrations were performed using an ^{56}Fe implanted reference sample. The reference sample had the same epilayer structure as the other doped samples, except that an undoped $Al_{0.9}Ga_{0.1}As_{0.06}Sb_{0.94}$ layer was grown instead of a Be- or Te-doped $Al_{0.9}Ga_{0.1}As_{0.06}Sb_{0.94}$ layer. The SIMS intensity (counts/s) to concentration (cm^{-3}) calibrations were performed by measuring the implanted profile with the same SIMS parameters before and after the measurements of the doped samples. The relative sensitivity factor (RSF) for the Te calibration was 2.2×10^{15} and that for the Be calibration was 1.0×10^{14}.

The DLTS measurements were performed in the temperature range of 30 K - 300 K with a reverse bias voltage of –1 V and –0.5 V, and a pulse voltage of 1 V and 0.5 V (50 ms duration) using a refined version of the setup described elsewhere [11]. The DLTS signal was extracted applying a lock-in weighting function with different rate windows in the range $(20\ ms)^{-1}$ – $(640\ ms)^{-1}$.

III. RESULTS AND DISCUSSIONS

Carrier concentration and Hall mobility values from Hall effect measurements and average dopant density values from SIMS measurements for Be-doped $Al_{0.9}Ga_{0.1}As_{0.06}Sb_{0.94}$ samples and for Te-doped $Al_{0.9}Ga_{0.1}As_{0.06}Sb_{0.94}$ samples are summarized in Table 2 and in Table 3, respectively.

Table 2. Be-doped $Al_{0.9}Ga_{0.1}As_{0.06}Sb_{0.94}$ samples: Carrier concentration and Hall mobility values from Hall effect measurements and average dopant density values from SIMS measurements.

Sample ID	Be source temperature (°C)	Carrier concentration (cm^{-3})	Hall mobility ($cm^2/V.s$)	Average dopant density (cm^{-3})
As 642	925	5.5×10^{16}	111	1.0×10^{17}
As 641	950	1.2×10^{17}	122	2.2×10^{17}
As 640	975	3.2×10^{17}	107	4.1×10^{17}
As 634	1000	7.2×10^{17}	102	8.4×10^{17}
As 635	1025	1.4×10^{18}	88	1.6×10^{18}
As 636	1050	3.0×10^{18}	74	2.9×10^{18}
As 637	1075	6.1×10^{18}	61	5.1×10^{18}
As 638	1100	1.2×10^{19}	51	9.6×10^{18}
As 639	1125	2.2×10^{19}	45	1.8×10^{19}
As 644	1150	3.7×10^{19}	42	2.9×10^{19}

Table 3. Te-doped $Al_{0.9}Ga_{0.1}As_{0.06}Sb_{0.94}$ samples: Carrier concentration and Hall mobility values from Hall effect measurements and average dopant density values from SIMS measurements.

Sample ID	GaTe source temperature (°C)	Carrier concentration (cm^{-3})	Hall mobility ($cm^2/V.s$)	Average dopant density (cm^{-3})
As 606-1	415	$< 1.0 \times 10^{17}$	-	3.7×10^{17}
As 608-4	430	1.1×10^{17}	41	5.7×10^{17}
As 602-2	450	1.3×10^{17}	30	2.3×10^{18}
As 608-3	465	1.6×10^{17}	24	8.3×10^{18}
As 606-2	475	1.6×10^{17}	20	1.4×10^{19}
As 606-4	485	1.6×10^{17}	19	2.4×10^{19}
As 606-3	495	1.6×10^{17}	21	3.8×10^{19}

The change in average dopant density in Be-doped $Al_{0.9}Ga_{0.1}As_{0.06}Sb_{0.94}$ with temperature of the Be source is presented in Fig. 1. The average dopant density was determined from the SIMS depth profile by finding the average of dopant density values in the 200-2000 nm depth range. The exponential fit to the data is also in conformity with the conventional Arrhenius behavior. Variations of carrier concentration and Hall mobility with average dopant density for Be-doped $Al_{0.9}Ga_{0.1}As_{0.06}Sb_{0.94}$ samples are shown in Fig. 2. The carrier concentration varies linearly with Be-dopant density and does not saturate up to the Be density of 2.9×10^{19} cm^{-3}. As expected, the Hall mobility for holes decreases with increasing Be dopant density and is in general lower as compared to that of p-type AlSb [12].

Due to a lattice mismatch of 7.9% at the growth temperature of 520 ºC, the $Al_{0.9}Ga_{0.1}As_{0.06}Sb_{0.94}$ epilayer grown on the GaAs(001) substrate is compressively strained and will start relaxing beyond its critical thickness of a few monolayers. We expect this to leave an array of periodic dislocations at the interface, similar to what is shown for AlSb grown on GaAs(001) substrate [13] (8.5% lattice mismatch at 520 ºC) and for GaSb grown on GaAs(001) substrate [14] (7.9% lattice mismatch at 520 ºC). However, Vaughan et al. [13] reported that the threading dislocation density for AlSb epilayer grown on GaAs(001), albeit large near the interface, reduces significantly as the AlSb growth progresses. Raisin et al. [14] found that after 25 nm of GaSb growth on GaAs, 99% of the lattice mismatch strain had relaxed. They explained the low density of threading defects in the GaSb epilayer (at least two orders of magnitude smaller at the level of the interface than in the 4.3% (at 580 ºC) mismatched GaAs/Si system) as being due to the high quality of misfit dislocation network in the GaSb/GaAs system. Likewise, there will be defects at the interface between the $Al_{0.9}Ga_{0.1}As_{0.06}Sb_{0.94}$ epilayer and the $Al_{0.3}Ga_{0.7}As$ cap layer, as the latter will relax due to tensile strain. Carrier concentration and mobility are in general sensitive to growth conditions, defects and impurity levels. In our case, the favorable band bending near the interfaces between the doped $Al_{0.9}Ga_{0.1}As_{0.06}Sb_{0.94}$ and the undoped GaAs and $Al_{0.3}Ga_{0.7}As$ should reduce the interaction between the majority carriers and the defects. The linear variation of hole concentration versus Be dopant density shown in Fig. 2 also indicates that the interaction between majority carriers and defects does not dramatically affect the carrier concentration. We should here also mention that Bennett et al. [12] found that the doping efficiencies of Be in GaAs on undoped GaAs(001) substrate and AlSb on undoped GaAs(001) substrate were equal in the $10^{16} – 10^{19}$ cm^{-3} range (using 5 nm undoped GaSb cap on the doped AlSb epilayer), consistent with previous measurement results in our group [15].

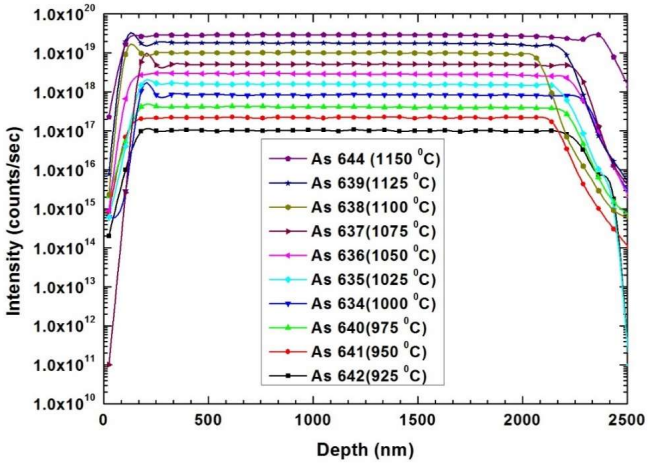

(a)

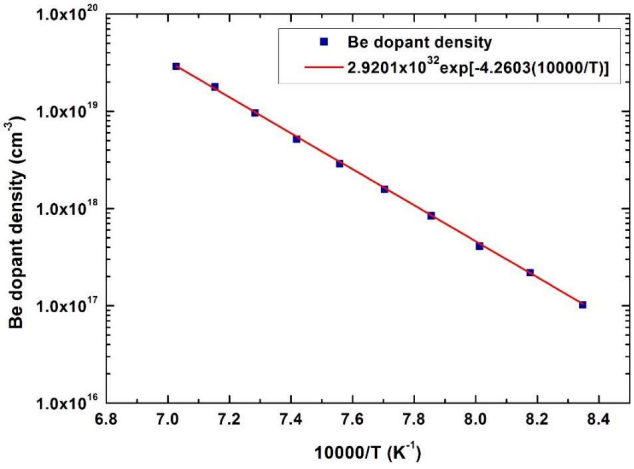

(b)

Figure 1. Variation in Be dopant density in $Al_{0.9}Ga_{0.1}As_{0.06}Sb_{0.94}$ with temperature of the Be source. **(a)** SIMS depth profile in Be-doped $Al_{0.9}Ga_{0.1}As_{0.06}Sb_{0.94}$ samples with undoped $Al_{0.3}Ga_{0.7}As$ cap layer. **(b)** Variation in Be dopant density in $Al_{0.9}Ga_{0.1}As_{0.06}Sb_{0.94}$ with inverse of absolute temperature (T) of the Be source.

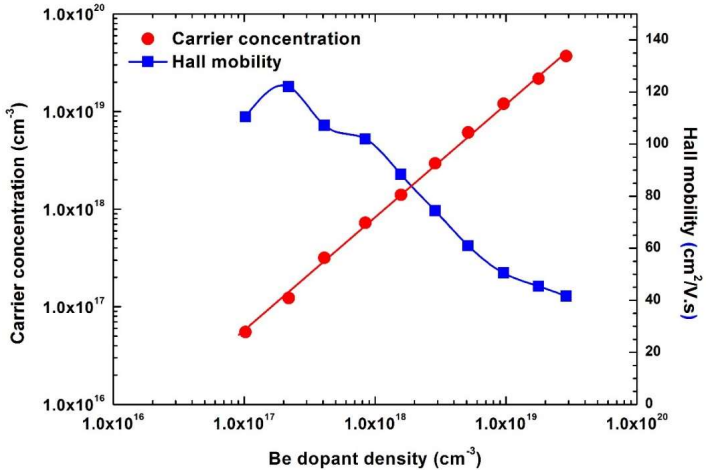

Figure 2. Variation in carrier concentration and Hall mobility with Be dopant density in Be-doped $Al_{0.9}Ga_{0.1}As_{0.06}Sb_{0.94}$. Drawn lines are guides to the eye only.

The change in average dopant density in Te-doped $Al_{0.9}Ga_{0.1}As_{0.06}Sb_{0.94}$ with temperature of the GaTe source is presented in Fig. 3. The average dopant density was determined from the SIMS depth profile by finding the average of dopant density values in the 200-2000 nm range. The variations of free carrier concentration and Hall mobility with average dopant density for Te-doped $Al_{0.9}Ga_{0.1}As_{0.06}Sb_{0.94}$ samples are shown in Fig. 4. The free carrier concentration saturates at 1.6×10^{17} cm^{-3} for Te dopant density 8.0×10^{18} cm^{-3} and hence the doping efficiency is only 2% at dopant density of 8.0×10^{18} cm^{-3}. Due to saturation in carrier concentration, addition of dopants beyond 8.0×10^{18} cm^{-3} only creates more defects as the dopants possibly stay at the interstitial sites in the crystal structure or/and form complexes. Possibly, annealing at a temperature higher than the growth temperature could enhance the doping efficiency and hence increase carrier concentration [16]. However, Te-doped $Al_{0.9}Ga_{0.1}As_{0.06}Sb_{0.94}$ is used as the cladding layer in mid-infrared lasers and annealing of lasers at high temperature is not preferred to avoid interdiffusion effects in the quantum wells and barriers and hence change in emitted wavelength [17, 18].

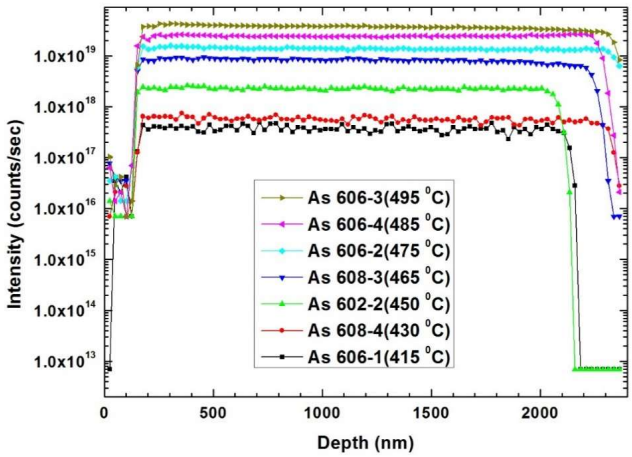

(a)

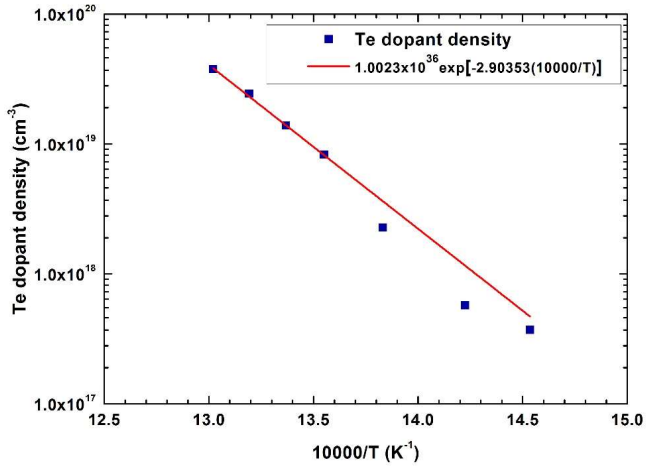

(b)

Figure 3. Te dopant density in $Al_{0.9}Ga_{0.1}As_{0.06}Sb_{0.94}$ versus temperature of the GaTe source. **(a)** SIMS depth profile in Te-doped $Al_{0.9}Ga_{0.1}As_{0.06}Sb_{0.94}$ samples with undoped $Al_{0.3}Ga_{0.7}As$ cap layer. **(b)** Variation in Te dopant density in $Al_{0.9}Ga_{0.1}As_{0.06}Sb_{0.94}$ with inverse of absolute temperature (T) of the GaTe source.

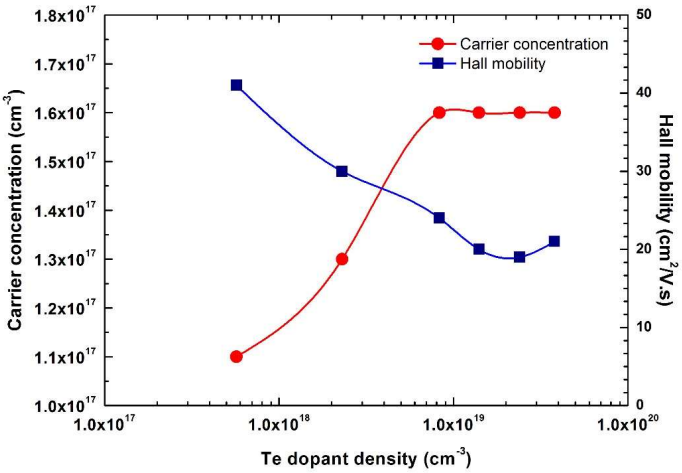

Figure 4. Variation in carrier concentration and Hall mobility with Te dopant density in Te-doped $Al_{0.9}Ga_{0.1}As_{0.06}Sb_{0.94}$. Drawn lines are guides to the eye only.

Chiu et al. [19] found from Hall effect measurements on 2 μm thick Te-doped GaSb epilayers on undoped GaAs(001) substrates that, for growth temperatures below 540 ºC, the free carrier concentration was very close to the Te dopant concentration (determined from SIMS) for Te concentrations in the 1×10^{17} cm^{-3} – 1×10^{18} cm^{-3} range. This shows that the dislocation and threading defects in the GaSb/GaAs system do not significantly affect the doping efficiency of Te in the GaSb epilayer in this range and we expect the same to be the case for our Te-doped $Al_{0.9}Ga_{0.1}As_{0.06}Sb_{0.94}$ samples. Chiu et al. [19] also found that the free carrier concentration saturates at around 1.5×10^{18} cm^{-3} for Te dopant density around 2-3 $\times 10^{18}$ cm^{-3} and that the free carrier concentration decreases for higher Te dopant densities. These findings are consistent with previous measurement results in our group [15] where we found the free carrier concentration to saturate at 1.8×10^{18} cm^{-3}.

The low doping efficiency effects in Te-doped $Al_{0.9}Ga_{0.1}As_{0.06}Sb_{0.94}$ are further investigated by DLTS measurements. DLTS signals for three Be-doped GaSb/ Te-doped $Al_{0.9}Ga_{0.1}As_{0.06}Sb_{0.94}$ PN diode samples with rate window (640 ms)$^{-1}$ are shown in Fig. 5. $\Delta C/C$ represents the ratio of trap concentration to total dopant concentration. Two dominant deep level defects are observed in all the samples: a shallower level with a peak DLTS signature around 120 K and a deeper level around 220 K. However, the peak temperature of both defects levels vary between samples. This may indicate that (i) the origin of the observed defects levels are not the same in Sb 284 – Sb 286; (ii) the observed defects are donors and the emissions rates are influences by Poole-Frenkel effect [20]; (iii) the tunneling leakage is high enough to affect the DLTS signatures of the observed defects [21]. Hence, further investigations are needed to elucidate the origin of the defect levels. The high concentration of the electrically active centers

in the Sb 284 sample also demonstrates that they have a strong impact on the carrier concentration, and may partially explain the reduced dopant activation in these samples.

According to Bourgoin and Mauger [22], the donor impurities in III-V semiconductors introduce two states, viz. a shallow state associated with the Γ-band and a deep state associated with the L-band and hence the introduction of DX-centers. Nakagawa et al. [23] have reported the presence of deep DX-center-like electron traps in AlSb. According to Baraldi et al. [24], these DX-centers have deep energy levels below the conduction band absolute minimum. The density of DX-centers depends exponentially on the energy difference between the Fermi energy (E_F) and the energy of the DX-center (E_{DX}) and the carrier concentration decreases with an increase in density of these DX-centers. Therefore, low doping efficiency in Te-doped $Al_{0.9}Ga_{0.1}As_{0.06}Sb_{0.94}$ is most likely due to presence of DX-centers.

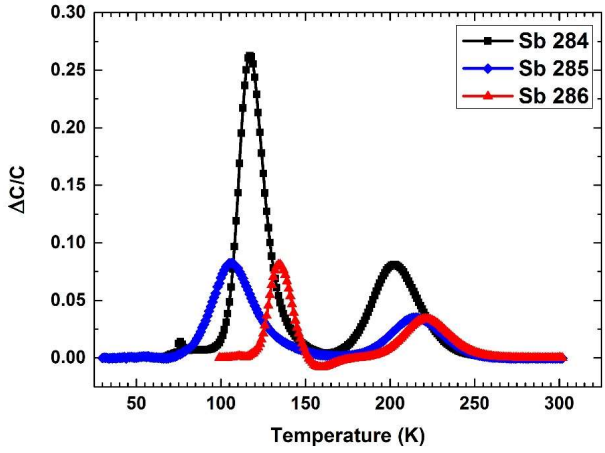

Figure 5. DLTS signal for three Be-doped GaSb/Te-doped $Al_{0.9}Ga_{0.1}As_{0.06}Sb_{0.94}$ PN- diode samples with rate window $(640\ ms)^{-1}$. Te dopant densities were 3.0×10^{18} cm^{-3} (Sb 284), 2.0×10^{18} cm^{-3} (Sb 285) and 1.0×10^{18} cm^{-3} (Sb 286).

IV. CONCLUSIONS

In this work, dependence of carrier concentration and Hall mobility on dopant density for both Be- and Te-doped $Al_{0.9}Ga_{0.1}As_{0.06}Sb_{0.94}$ was investigated. Use of undoped $Al_{0.3}Ga_{0.7}As$ cap layer and photoresist passivation layer helped in reducing oxidation and hence improving accuracy in measurements for carrier concentration and Hall mobility. Carrier concentration was found to vary linearly with dopant density for Be-doped $Al_{0.9}Ga_{0.1}As_{0.06}Sb_{0.94}$, whereas it saturates at 8.0×10^{18} cm^{-3} dopant density for Te-doped $Al_{0.9}Ga_{0.1}As_{0.06}Sb_{0.94}$. As per DLTS

measurements, low doping efficiency in Te-doped $Al_{0.9}Ga_{0.1}As_{0.06}Sb_{0.94}$ is due to presence of deep trap levels.

ACKNOWLEDGMENTS

The authors would like to acknowledge the funding from the Research Council of Norway under Contract No. 177610/V30 and the Norwegian PhD Network on Nanotechnology for Microsystems (financial support to PhD students) and to the Norwegian Micro- and Nano-Fabrication Facility, NorFab (Grant No. 197411/V30)

REFERENCES

[1] L.S. Rothman, D. Jacquemart, A. Barbe, D. Chris Benner, M. Birk, L. Brown, M. Carleer, C. Chackerian Jr, K. Chance, L. Coudert, et al., The HITRAN 2004 molecular spectroscopic database, Journal of Quantitative Spectroscopy and Radiative Transfer, 96 (2005) 139-204. DOI:10.1016/j.jqsrt.2004.10.008

[2] E. Tournié, A.N. Baranov, Mid-Infrared Semiconductor Lasers: A Review, in: J. J. Coleman, B. Catrina, C. Jagadish (Eds.) Advances in Semiconductor Lasers, Academic Press, 2012, pp. 183-226. ISBN:9780123910660

[3] M. Breivik, T.A. Nilsen, G. Myrvågnes, E. Selvig, B.-O. Fimland, Temperature dependent lattice constant of $Al_{0.9}Ga_{0.1}As_ySb_{1-y}$, Journal of Vacuum Science & Technology B, 28 (2010) C3I1-C3I5. DOI:10.1116/1.3414830

[4] D. Donetsky, G. Kipshidze, L. Shterengas, T. Hosoda, G. Belenky, 2.3 µm type-I quantum well GaInAsSb/AlGaAsSb/GaSb laser diodes with quasi-cw output power of 1.4 W, Electronics Letters, 43 (2007) 810-812. DOI:10.1049/el:20071320

[5] R.G. Bedford, G. Triplett, D.H. Tomich, S.W. Koch, J. Moloney, J. Hader, Reduced auger recombination in mid-infrared semiconductor lasers, Journal of Applied Physics, 110 (2011) 073108- 073106. DOI:10.1063/1.3646552

[6] S.J. Eglash, H.K. Choi, G.W. Turner, MBE growth of GaInAsSb/AlGaAsSb double heterostructures for infrared diode lasers, Journal of Crystal Growth, 111 (1991) 669-676. DOI:10.1016/0022-0248(91)91061-E

[7] A.Z. Li, J.X. Wang, Y.L. Zheng, G.P. Ru, W.G. Bi, Z.X. Chen, N.C. Zhu, The behavior of dopant incorporation and internal strain in $Al_xGa_{1-x}As_{0.03}Sb_{0.97}$ grown by molecular beam epitaxy, Journal of Crystal Growth, 127 (1993) 566-569. DOI:10.1016/0022-0248(93)90684-O

[8] H. Ehsani, N. Lewis, G.J. Nichols, L. Danielson, M.W. Dashiell, Z.A. Shellenbarger, C.A. Wang, Effect of substrate surface defects and Te dopant concentration on crystalline quality and electrical characteristics of AlGaAsSb epitaxial layers, Journal of Crystal Growth, 291 (2006) 77-81. DOI:10.1016/j.jcrysgro.2006.02.054

[9] T.-N. Tran, S.K. Patra, M. Breivik, B.-O. Fimland, Plasma-assisted oxide removal from p-type GaSb for low resistivity ohmic contacts, Journal of Vacuum Science & Technology B, 33 (2015) 061210. DOI:10.1116/1.4935883

[10] N. Rahimi, A.A. Aragon, O.S. Romero, D.M. Kim, N.B.J. Traynor, T.J. Rotter, G. Balakrishnan, S.D. Mukherjee, L.F. Lester, Ohmic contacts to n-type GaSb grown on GaAs by the interfacial misfit dislocation technique, Physics, Simulation, and Photonic Engineering of Photovoltaic Devices II, Proc SPIE, 8620 (2013) 86201K. DOI:10.1117/12.2003392

[11] B.G. Svensson, K.H. Rydén, B.M.S. Lewerentz, Overlapping electron traps in n-type silicon studied by capacitance transient spectroscopy, Journal of Applied Physics, 66 (1989) 1699-1704. DOI:10.1063/1.344389

[12] B.R. Bennett, W.J. Moore, M.J. Yang, B.V. Shanabrook, Transport properties of Be- and Si-doped AlSb, Journal of Applied Physics, 87 (2000) 7876-7879. DOI:10.1063/1.373470 19

[13] E.I. Vaughan, S. Addamane, D.M. Shima, G. Balakrishnan, A.A. Hecht, High-Resistivity Semiinsulating AlSb on GaAs Substrates Grown by Molecular Beam Epitaxy, Journal of Electronic Materials, 45 (2016) 2025-2030. DOI:10.1007/s11664-016-4359-y

[14] C. Raisin, A. Rocher, G. Landa, R. Carles, L. Lassabatere, GaSb/GaAs heteroepitaxy characterized as a stress-free system, Applied Surface Science, 50 (1991) 434-439. DOI:10.1016/0169-4332(91)90213-4

[15] E. Selvig, Molecular beam epitaxial growth and characterization of GaInAsSb/AlGaAsSb midinfrared laser structures, Doctoral thesis, Norwegian University of Science and Technology, Trondheim, 2004. ISBN:8247163926

[16] K.-K. Kim, S. Niki, J.-Y. Oh, J.-O. Song, T.-Y. Seong, S.-J. Park, S. Fujita, S.-W. Kim, High electron concentration and mobility in Al-doped n-ZnO epilayer achieved via dopant activation using rapid-thermal annealing, Journal of Applied Physics, 97 (2005) 066103. DOI:10.1063/1.1863416

[17] R. Bugge, B.-O. Fimland, Annealing effects in InGaAsSb quantum wells with pentenary AlInGaAsSb barriers, Physica Scripta, T126 (2006) 15-20. DOI:10.1088/0031-8949/2006/T126/004

[18] Y. Wang, H. Djie, B. Ooi, Interdiffusion in InGaAsSb⁄AlGaAsSb quantum wells, Journal of Applied Physics, 98 (2005) 073508. DOI:10.1063/1.2061893

[19] T.H. Chiu, J.A. Ditzenberger, H.S. Luftman, W.T. Tsang, N.T. Ha, Te doping study in molecular beam epitaxial growth of GaSb using Sb_2Te_3, Applied Physics Letters, 56 (1990) 1688-1690. DOI:10.1063/1.103118

[20] J. Frenkel, On pre-breakdown phenomena in insulators and electronic semi-conductors, Physical Review, 54 (1938) 647-648. DOI:10.1103/PhysRev.54.647

[21] M.C. Chen, D.V. Lang, W.C. Dautremont-Smith, A.M. Sergent, J.P. Harbison, Effects of leakage current on deep level transient spectroscopy, Applied Physics Letters, 44 (1984) 790-792. DOI:10.1063/1.94887

[22] J. Bourgoin, A. Mauger, Physical origin of the DX center, Applied Physics Letters, 53 (1988) 749-751. DOI:10.1063/1.99821

[23] A. Nakagawa, J.J. Pekarik, H. Kroemer, J.H. English, Deep levels in Te-doped AlSb grown by molecular beam epitaxy, Applied Physics Letters, 57 (1990) 1551-1553. DOI:10.1063/1.103350

[24] A. Baraldi, C. Ghezzi, A. Parisini, R. Magnanini, L. Tarricone, S. Franchi, Occupancy level of the DX center in Te-doped $Al_xGa_{1-x}Sb$, Journal of Applied Physics, 85 (1999) 256-263. DOI:10.1063/1.369438

5.2. Paper 2 - High precision AlGaAsSb ridge-waveguide etching by *in situ* reflectance monitored ICP-RIE

Authors: **Thanh-Nam Tran**, Magnus Breivik, Saroj Kumar Patra, and Bjørn-Ove Fimland

First published in: Semiconductor Lasers and Laser Dynamics VI, Proc. SPIE 9134 (2014) - 91342E

DOI: 10.1117/12.2052615

Contributions: MB conceived the initial research idea and **TNT** planned the study under the supervision of BOF. **TNT** performed the experimental works related to the ICP-RIE process with the *in situ* reflectance monitoring system. MB provided simulations results. SKP grew samples using MBE and performed structural characterizations on these. **TNT** did all data analysis, drafted the first version of the manuscript, discussed it with other authors, and finalized it.

Abstract

GaSb-based semiconductor diode lasers are promising candidates for light sources working in the mid-infrared wavelength region of 2-5 µm. Using edge emitting lasers with ridge-waveguide structure, light emission with good beam quality can be achieved. Fabrication of the ridge waveguide requires precise etch stop control for optimal laser performance. Simulation results are presented that show the effect of increased confinement in the waveguide when the etch depth is well-defined. *In situ* reflectance monitoring with a 675 nm-wavelength laser was used to determine the etch stop with high accuracy. Based on the simulations of laser reflectance from a proposed sample, the etching process can be controlled to provide an endpoint depth precision within ± 10 nm.

Keywords: Ridge-waveguide laser, dry etching, endpoint detection, *in situ* reflectance monitoring

I. INTRODUCTION

GaSb and related compounds in the 6.1 Å family have shown high potential for a wide range of optoelectronic applications. Semiconductor diode lasers fabricated from these compounds are promising candidates for mid-infrared lasers in the wavelength region of 2-5 µm, whose applications include the light sources needed for trace-gas sensing systems based on tunable diode-laser absorption spectroscopy (TDLAS). Using edge emitting lasers with a ridge-waveguide structure, light emission with good beam quality can be achieved. The ridge waveguide etch depth plays a key role in the laser's characteristics, namely the optical confinement and surface recombination of injected carriers[1, 2]. By creating a large index contrast, the light can be well-confined inside the waveguides. This is very critical for reducing high bend losses in waveguide designs such as S-bend, Y-branch and Mach-Zehnder structures.

The fabrication of ridge-waveguide lasers benefits from an etch process capable of controlling the etch stop in real-time. A common approach for precise etching is dry etching using endpoint detection. For laser fabrication, dry etching is preferable over wet chemical etching because it is capable of creating close to vertical sidewall profiles with high uniformity and good reproducibility. Additionally, the etch process can be controlled by *in situ* monitoring techniques like optical emission spectroscopy, reflectometry, photoluminescence, and mass spectrometry. In this paper, *in situ* reflectance monitoring with a 675 nm-wavelength laser was used to determine the etch stop with a high accuracy in a laser structure for 2.2 µm wavelength lasing. The principle of this technique is based on the interference of the reflected laser light in multilayered thin films structure. The interferometric variation of the reflectance signal ceases when the top layer is etched completely.

To achieve the optimal optical and electrical confinement for the mid-infrared laser performance, it is desirable to stop etching at the interface between the upper cladding layer (typically $Al_{0.9}Ga_{0.1}AsSb$) and the separate confinement heterostructure (SCH) layer (typically $Al_xGa_{1-x}AsSb$ with x much less than 0.9). However, due to the lack of precise data for the optical properties of the laser materials, a simpler structure consisting of only $Al_{0.9}Ga_{0.1}AsSb$

(cladding) capped with GaSb and grown on GaSb(100) substrate was proposed for the reflectance monitoring. The reflectance monitoring was performed on such a sample while etching it simultaneously with a laser structure sample having similar upper cladding and cap layers.

In sections 2.1 and 2.2, the effect of etch depth to the waveguiding properties of the ridge and Y-branch waveguides in a laser structure for 2.2 µm wavelength lasing is investigated. Based on the simulation of laser reflectance on the proposed sample, presented in section 2.3, precise fabrication of the ridge waveguides was performed by ICP-RIE using *in situ* reflectance technique. The reflectance pattern recorded during etching of the proposed sample provides information about the refractive index of the $Al_{0.9}Ga_{0.1}AsSb$ cladding layer at 675 nm wavelength, which can be used for reflectance simulations.

II. SIMULATIONS

1. Light propagation in ridge-waveguides

The height of the ridge, or the etch depth, is critical for the propagation of light in the ridge waveguide. In this work, the characteristics of the laser beam, namely the beam confinement and far field pattern, in ridge waveguides with different etch depths were investigated. The laser structure and the refractive indices of these materials are presented in Table 1. Solutions to the mode profiles for different etch depths were simulated using the Light software by Sarangan [3]. To account for the etched ridge, the removed cladding material was replaced by photoresist with the refractive index of 1.5, which represents the ridge-sidewall insulation layer. Simulation for different ridge widths of 1.5, 2.0 and 2.5 µm, respectively, were performed. The results for the 2 µm wide ridge are shown in Figure 1. The results for the 1.5 and 2.5 µm wide ridges were qualitatively the same as for the 2.0 µm wide ridge.

Table 1. Layer information for the nominal laser structure used in the simulations presented in Figs. 1 and 2. The buffer layer includes a superlattice and a grading layer, which however has negligible effect on the simulation results and for simplicity are therefore not specified here. A 42 nm grading layer between upper cladding and cap has been omitted in the table for the same reason.

Layer	Material	Thickness (nm)	Refractive index at above 2 µm [4]
Substrate	GaSb	5×10^5	3.8
Buffer	GaSb	980	3.8
Cladding	$Al_{0.9}GaAsSb$	2000	3.4
SCH	$Al_{0.25}GaAsSb$	150	3.58
Multiple Quantum Well	AlGaAsSb/GaInAsSb	20/12.5 x 3	3.89
SCH	$Al_{0.25}GaAsSb$	150	3.58
Cladding	$Al_{0.9}GaAsSb$	2000	3.4
Cap	GaSb	50	3.8

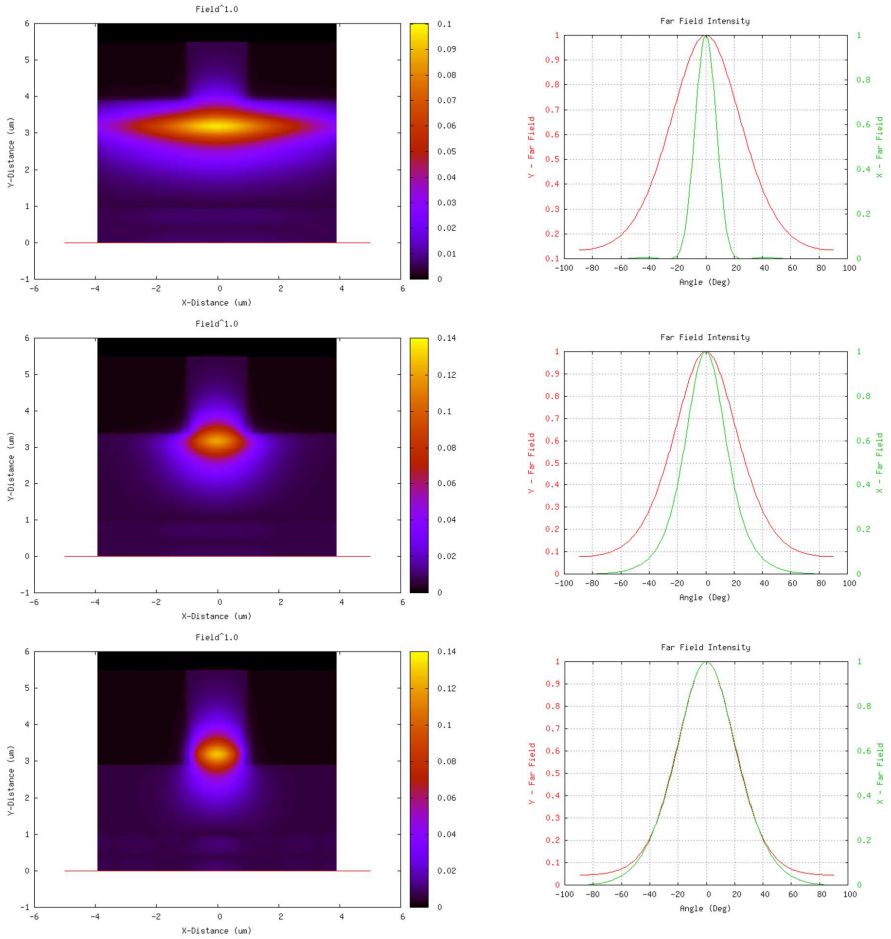

Figure 1. 2D mode solutions for the waveguide mode profiles (left) in the laser structure and their far field patterns (right). The green line is the in-plane (x) and the red line is the out-of-plane (y) far field, respectively. From top to bottom: etch depth of 1.6, 2.1 and 2.6 µm. Ridge width is 2.0 µm. The thickness of the laser structure above the waveguide core is nominally 2.092 µm.

2. Light propagation in Y-branch waveguides

The propagation of an optical field through a Y-branch waveguide requires a sufficient refractive index contrast to avoid large bending losses. In this work, the waveguiding properties of a Y-branch (2 µm wide ridge, 750 µm bend radius) with different refractive index contrast, *dn*, were investigated by the beam propagation method (BPM). The larger refractive index

contrast can be interpreted as a deeper etch [5]. Additionally, the waveguide roughness due to the imperfection of the mask, photoresist and the ICP-RIE process was introduced to the simulation. The refractive indices for the simulations were chosen on the basis of measurements of the Fabry-Perot mode spacing of the ridge waveguide lasers. The structure of these lasers is shown in Table 1, and the effective group indices were found to be from 3.75 to 3.85. The background refractive index was therefore set to 3.77, and the waveguide refractive index was set to 3.77 + *dn* where *dn* varies from 0.02 to 0.05. Some of the simulation results are shown in Figure 2.

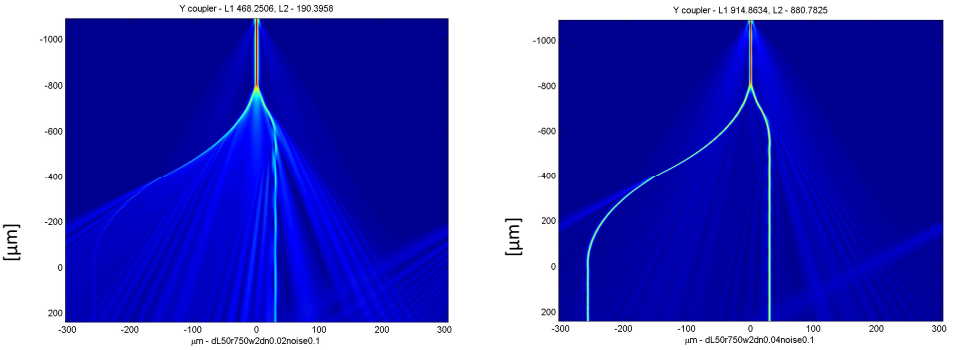

Figure 2. 2D BPM simulation of light propagation in Y-branch with an etch roughness of 0.1 µm. The refractive index contrast is 0.02 (left) and 0.04 (right).

3. Simulation of reflectance variation during etching

The reflectance signal during etching can in principle be simulated from the reflectance of the laser structure in question, containing layers of different compositions and thicknesses. Therefore, the etch stop can be predicted precisely within 10 nm. The simulations were based on the script given by Oxford Instruments [6]. However, due to the lack of precise data on the optical properties of the laser materials at 675 nm wavelength, the simulation was only performed on the proposed structure. For the simulation, the refractive index of $Al_{0.9}Ga_{0.1}AsSb$ at 675 nm wavelength as determined from the experiment described below was used. By controlling the etch stop when etching the $Al_{0.9}Ga_{0.1}AsSb$ cladding layer, the thickness D etched in one signal period T, shown in Figure 3, can be measured and used to calculate the refractive index of $Al_{0.9}Ga_{0.1}AsSb$ by the following equation: $D = \lambda / 2n$, where λ is the laser wavelength and n is the refractive index of $Al_{0.9}Ga_{0.1}AsSb$ at the wavelength λ. Figure 4 shows the simulated interferometric variation of the laser reflectance during etching as a function of film thickness.

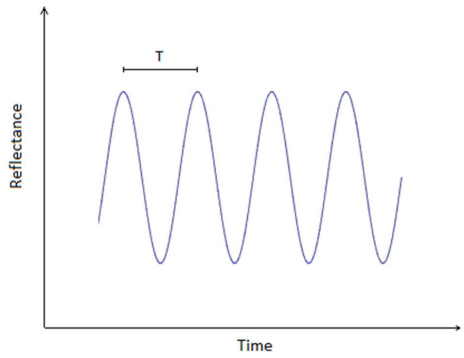

Figure 3. During the etching process, the reflectance signal is expected to vary with a period T.

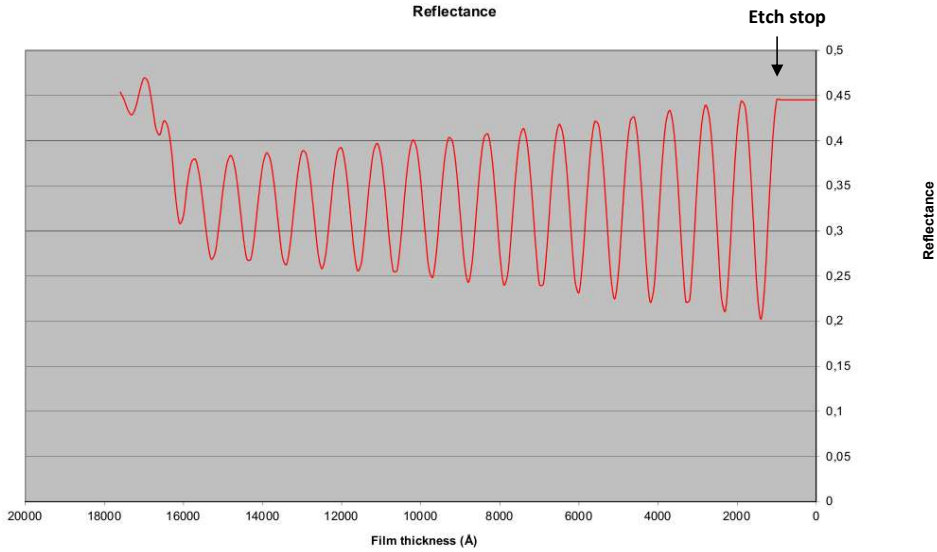

Figure 4. Simulation of laser reflectance from the proposed sample as a function of film thickness during the etching process. Note that 100 nm of GaSb was added between the cladding layer and the substrate to show how the reflectance is after etching through the thin films. This layer corresponds to the horizontal line at the right side of the reflectance oscillations.

III. EXPERIMENTS

The epitaxial structure of the proposed sample consisting of 1.4 µm $Al_{0.9}Ga_{0.1}AsSb$ followed by 42 nm grading of AlGaAsSb/GaSb and capped by 100 nm of GaSb was grown on GaSb(100) substrate using molecular beam epitaxy (MBE). The etch depth target is 1542 nm. Before processing, the wafer was cleaved into 1 x 1 cm pieces. The ridges were defined on the sample with photoresist SPR700 using standard i-line photolithography. Etching was performed in an Oxford Plasma System 100 ICP380 reactor at 60 ºC. Using fomblin oil, the samples were mounted on a sapphire carrier which was backside cooled with He gas during etching. The baseline etch parameters are 1000 W ICP power, 150W RF power, 4 mTorr chamber pressure, 23 sccm Ar flow rate and 6 sccm BCl_3 flow rate. An *in situ* 675 nm wavelength laser was used for endpoint detection. An example of the interferometric variation of the recorded reflectance signal during the etching process of the proposed sample is shown in Figure 5. To determine the thickness D, related to the period, the etching process was stopped at different peaks in the recorded reflectance signal for different samples. The etch depth and sidewall profile were evaluated with a scanning electron microscope (SEM). The mean value of D from 6 samples with different etch depths was used to calculate the refractive index used in the simulations of laser reflectance.

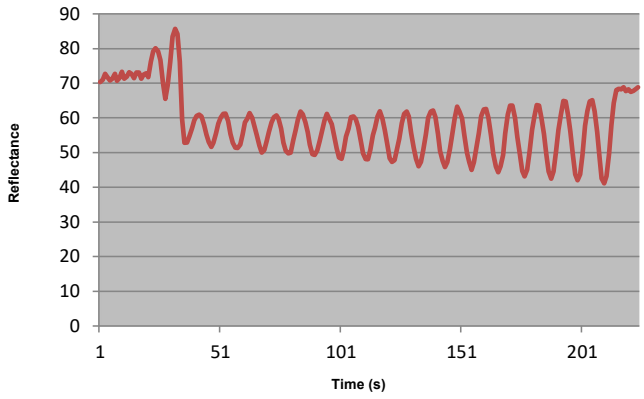

Figure 5. Reflectance signal from etching the proposed sample. Note that the etch rate is slower at close to the edge of the ridge waveguide. Therefore, extra time was added to get the correct etch depth.

IV. RESULTS AND DISCUSSION

The simulation results in sections 2.1 and 2.2 show the effect of increased confinement in the waveguide when the etch depth increases. As seen in Figure 1, increase in etch depth provides better confinement of the mode profiles in the ridge. This is also indicated in the change of far field intensity profile. Figure 2 shows the reduction of bending losses of light in

Y-branch waveguides when increasing the refractive index contrast. Consequently, higher etch depth provides better optical confinement of the ridge waveguide. However, if the etching is too deep, the edges of the active region can be in contact with imperfect surfaces because of waveguide roughness. That leads to significant degradation of the laser performance due to strong surface recombination of the injected carriers [7]. Therefore, it is desirable to control precisely the etch stop to optimize both optical and electrical confinement properties of the ridge waveguide.

In this work, all simulations performed have only used the real refractive index, and the effect of gain and absorption have not been accounted for. The real refractive index of $Al_{0.9}Ga_{0.1}AsSb$ at 675 nm wavelength was found to be equal to 3.65 ± 0.05. This value is smaller than the value published by Adachi [8]. However, it provides good agreement between measured and simulated variation in the reflectance signal during the etching. Figure 6 shows the etch depth measurement of the proposed sample by SEM. It shows that the etching target of 1542 nm is fulfilled and the etching process can be controlled to provide an endpoint depth precision within ± 10 nm.

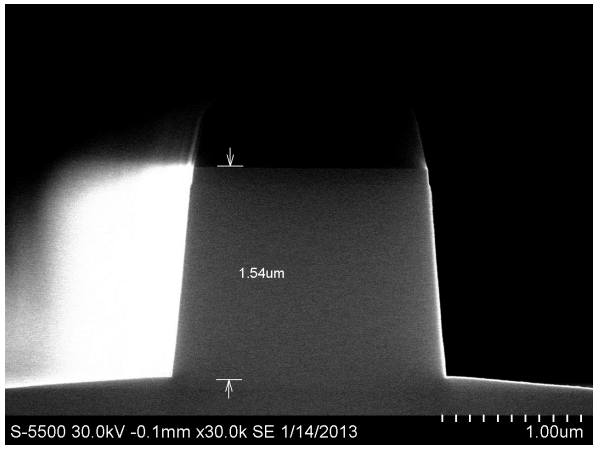

Figure 6. SEM image of the cross-section of the proposed sample. The etch depth was very close to the target of 1.542 μm. The accuracy of the measurements depends on the SEM instrument.

V. CONCLUSIONS

In conclusion, ridge waveguides for laser application were fabricated by ICP-RIE using *in situ* reflectance monitoring with a high precision. The role of etch depth to the waveguiding properties of the ridge waveguide was also investigated to emphasize the importance of endpoint detection. The simulation of laser reflectance during the etching process provides a

guideline to controlling the etch stop. The refractive index of $Al_{0.9}Ga_{0.1}AsSb$ was determined for 675 nm wavelength.

ACKNOWLEDGMENTS

The authors would like to acknowledge the Norwegian University of Science and Technology for support (from the Strategic Area Materials program) and the Research Council of Norway for the support to this work (Grant 177610/V30) and to the Norwegian Micro- and Nano-Fabrication Facility, NorFab (Grant 197411/V30).

REFERENCES

[1] Casey, H. C., Jr and Panish, M. B., [Heterostructure Lasers, Part B: Material and Operating Characteristics], Academic Press, Orlando (1978).

[2] Redaelli, L., et al., "Effect of ridge waveguide etch depth on laser threshold of InGaN MQW laser diodes", Proc. SPIE 8262 (2012).

[3] Saragan, A., "LIGHTS Online Optical Simulation Software", http://www.nano-fab.com/lights/.

[4] Gonzalez-Cuevas, J. A., Refaat, T. F., Abedin, M. N. and Elsayed-Ali, H. E., "Calculations of the temperature and alloy composition effects on the optical properties of $Al_xGa_{1-x}As_ySb_{1-y}$ and $Ga_xIn_{1-x}As_ySb_{1-y}$ in the spectral range 0.5-6 eV", J. Appl. Phys. 102(1), 014504-014504-11 (2007).

[5] Aiki, K., et al., "Transverse mode stabilized $Al_xGa_{1-x}As$ injection lasers with channeled-substrate-planar structure", IEEE J. Quantum Electron. 14(2), 89-94 (1978).

[6] Welch, C., Oxford Instruments Plasma Technology, Personal communication (2013).

[7] Agrawal, G. P. and Dutta, N. K., [Long-wavelength semiconductor lasers], Van Nostrand Reinhold, New York, 113-116 (1986).

[8] Adachi, S., "Band gaps and refractive indices of AlGaAsSb, GaInAsSb, and InPAsSb: Key properties for a variety of the 2–4-μm optoelectronic device applications", J. Appl. Phys. 61(10), 4869-4876 (1987).

5.3. Paper 3 – Plasma-assisted oxide removal from p-type GaSb for low resistivity ohmic contacts

Authors: **Thanh-Nam Tran**, Saroj Kumar Patra, Magnus Breivik, and Bjørn-Ove Fimland

First published in: *Journal of Vacuum Science & Technology B* 33, 061210 (2015)

DOI: 10.1116/1.4935883

Contributions: **TNT** planned the study under the supervision of BOF. **TNT** performed the experimental works related to the fabrication of TLM structures with different oxide removal techniques. **TNT** performed measurements of specific contact resistivity and surface characterizations using SEM and AFM. SKP grew samples using MBE and performed electrical characterizations on these. MB provided useful feedbacks to the sample fabrication and characterizations. **TNT** did all data analysis, drafted the first version of the manuscript, discussed it with other authors, and finalized it.

Abstract

The effect of several plasma-assisted oxide removal techniques prior to metallization of p-type GaSb was investigated. Compared to conventional chemical methods, the plasma-assisted oxide removal resulted in significant improvement of the specific contact resistivities, obtained from transfer length method measurements. Very low specific contact resistivities of less than 5×10^{-8} Ω cm^2 were observed after surface pretreatment by H_2/Ar sputter etching and low-ion-energy Argon irradiation. By eliminating sample exposure to air, *in situ* Ar irradiation becomes a promising technique for high performance GaSb-based semiconductor diode lasers.

I. INTRODUCTION

GaSb-based diode lasers are one of the most promising monochromatic light sources in the mid-infrared wavelength region of 2-5 μm, and low resistance ohmic contact to GaSb is desirable for high performance operation of these devices. When exposed to air, the GaSb surface quickly forms a 3-5 nm thick surface oxide layer[1]. It is therefore essential to remove this oxide layer prior to metallization to achieve a good ohmic contact.

Current approaches for GaSb native oxide removal are primarily based on wet chemical clean using common acids and bases in semiconductor processing, such as HCl, HF or NH_4OH. Among chemical treatments, HCl clean is reported to be the best choice to create an oxide-free surface[1,2]. However, the chemical treatments prior to metallization lack reproducibility due to the rapid reoxidation of GaSb. Thus, *in situ* oxide removal techniques prior to metallization are advantageous. Argon plasma irradiation has recently been used for removal of the native oxide of III-V compounds for contact purposes[3-5] and low-ion-energy Ar^+ irradiation on oxidized GaSb can lead to a nanostructured and oxide-free surface[6,7]. However, the effect on the metal-GaSb contact properties from such Ar^+ irradiation has yet not been fully characterized. Other reported plasma-assisted techniques used to (at least partly) remove the GaSb native oxide are hydrogen (H_2) plasma cleaning and GaSb etching using chlorine-based chemistry[8-10].

In this work, *in situ* Ar^+ irradiation with different ion energies, H_2 and BCl_3 plasma cleaning were applied to remove the native oxide of p-type GaSb. The effect of each of these oxide removal techniques on the contact properties in comparison with the conventional chemical methods is evaluated via the specific contact resistivity between the metallic layers and p-GaSb.

II. EXPERIMENTAL

Two micrometer thick epitaxial layers of Be-doped GaSb were grown on n-type GaSb (100) wafers in a Varian GEN II molecular beam epitaxy system. The p-type doping concentration was 2×10^{19} cm^{-3}, which is a typical concentration for the laser cap layer[11,12]. An n-type GaSb substrate with a nominal carrier concentration of 5×10^{17} cm^{-3} was chosen to create a p-n junction in order to prevent the current leaking into the substrate.

The specific contact resistivity was determined by the transfer length method (TLM) and four-point probe measurements. TLM structures were defined by conventional UV-lithography and were isolated on rectangular mesas by inductively-coupled plasma reactive ion etching (ICP-RIE). Ti/Pt/Au is the standard p-sided metallization for a number of antimonide-based devices. The specific contact resistivity of this metallization is typically in the order of 10^{-7} - 10^{-6} Ω cm^2 [5,13]. In this work, the Ti/Pt/Au metallization was performed by e-beam evaporation in a combined sputtering and e-beam evaporation system (AJA ATC-2200V) with Ti-, Pt- and Au-thicknesses of 50 nm, 25 nm and 325 nm, respectively. The different oxide removal techniques applied prior to metallization were:

1- *In situ* Ar plasma etching with different ion energies (70 eV, 120 eV, 180 eV, 250 eV, and 325 eV) for 1 min at 3 mTorr.
2- H_2/Ar etching by ICP-RIE for 45 s at 80 °C. The baseline etch parameters are 50 W RF power, 400 W ICP power, 50 mTorr chamber pressure, 100 sccm Ar flow rate and 15 sccm H_2 flow rate.
3- BCl_3/Ar etching by ICP-RIE for 1 min at 20 °C. The baseline etch parameters are 15 W RF power, 50 W ICP power, 2 mTorr chamber pressure, 3 sccm Ar flow rate, 10 sccm BCl_3 flow rate and 2 sccm N_2 flow rate.
4- 18.5 % HCl soak for 30 s followed by a deionized water (DIW) rinse for 5 s and quick drying in N_2.
5- 18.5 % HCl soak for 30 s followed by 2 % $(NH_4)_2S$ soak for 5 s and quick drying in N_2.

ICP-RIE was performed in an Oxford plasma system 100 ICP380 reactor. Samples undergoing the surface treatment methods 2 through 5 were immediately transferred to the metallization system (less than 30 s exposure to air). After lift-off, the samples underwent a rapid thermal anneal at 290 °C for 45 s. This annealing procedure is commonly used for contacts to n-type GaSb[14] in laser fabrication, and thus simultaneously applied for contacts to p-type GaSb. Finally, TLM patterns on p-type GaSb epilayer were wire-bonded to the Au bonding pads on glass substrate, as shown in Fig. 1, for four-probe measurements using a Lake Shore Hall effect measurement system. The adhesion between the metals and p-type GaSb epilayer was evaluated during the bonding process.

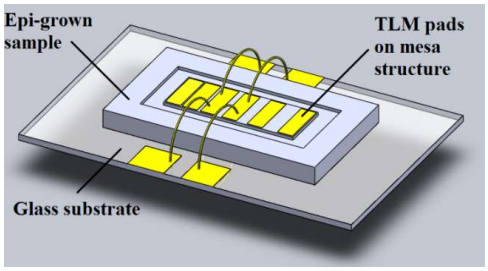

Figure 1. TLM structure wire-bonded to Au pads on glass. TLM pad size is 250 x 750 µm and the distance between TLM pads is 25, 50, 100, 175, and 250 µm.

III. RESULTS AND DISCUSSION

The measured specific contact resistivities for different oxide removal techniques are summarized in Table 1.

Table 1: p-type GaSb/Ti/Pt/Au contact: The measured specific contact resistivity and adhesion property for each treatment

Treat-ment	Surface treatment	Lowest ρ_c (10^{-8} Ω cm^2)	Highest ρ_c (10^{-8} Ω cm^2)	Average ρ_c (10^{-8} Ω cm^2)	Adhesion property
1a (N=3)	Ar irradiation - 70 eV	24.1	87.1	47.1 (for N=3)	Poor
1b (N=3)	Ar irradiation - 120 eV	5.42	5.88	5.59 (for N=3)	Good
1c (N=4)	Ar irradiation - 180 eV	0.28	4.28	2.11 (for N=3*)	Good
1d (N=5)	Ar irradiation - 250 eV	2.27	18.8	11.9 (for N=5)	Good
1e (N=3)	Ar irradiation - 325 eV	3.73	17.4	10.5 (for N=3)	Good
2 (N=4)	H_2/Ar etching	---	2.72	2.72 (for N=1*)	Good
3 (N=3)	BCl_3/Ar etching	59.4	65.5	62.4 (for N=3)	Poor
4 (N=3)	HCl soak + DIW rinse	53.2	111	81.7 (for N=3)	Poor
5 (N=3)	HCl soak + sulphur passivation	25.9	32.2	28.4 (for N=3)	Poor

Good: the metal contacts after bonding provide excellent electrical connection
Poor: the metal contacts are easily peeled off from the GaSb epilayer during the bonding process
N: number of samples
*: Measurement results of the other samples gave negative contact resistance

The TLM only gives accurate/valid results, i.e. consistent with the theory (equations) used, for $\rho_c > 0.2\ \rho_s\ t^2$ where ρ_s is the semiconductor sheet resistance and t is the layer thickness[15], whereas the results are expected to deviate more (in percentage) from theory below this value. In our experiments, $0.2\ \rho_s\ t^2 = 5 \times 10^{-8}\ \Omega\ cm^2$. Thus, the TLM failed to determine accurately the extremely low specific contact resistivities of the contacts after treatment 1c and 2. This is supported by the fact that the measurements of one sample of treatment 1c and three samples of treatment 2 gave a negative contact resistance R_c with the absolute value similar to those of the above results. For each sample, the measurement results were repeatable within 5% of the overall mean value, and thus the variation of ρ_c is attributed to the fabrication process.

The results from the conventional chemical treatment, treatment 4, are in line with previously reported results[5]. Comparing the chemical treatments 4 and 5, the sulphur passivation after HCl soak showed the better contact properties. This can be explained by the decrease in the surface state density after sulphur surface treatment[16]. However, the presence of a thin oxide or sulfur passivation layer on the semiconductor surface after these pre-treatments leads to poor adhesion of the metal contacts.

The results of specific contact resistivity from Ar^+ irradiation surface treatment (1 a-e) show the advantage of the *in situ* oxide removal technique in terms of contact and adhesion properties. At 70 eV, the ion-induced effect was insufficient, resulting in high ρ_c and poor adhesion of the metal contact. When the ion energy was increased, but still moderate, the ion bombardment was adequate to remove the oxide (at least sufficiently to get a good contact) while minimizing the ion-induced damage of the GaSb surface. At 180 eV, the specific contact resistivity to p-type GaSb is lowest and below the limit for accurate TLM measurement results (i.e. below $5 \times 10^{-8}\ \Omega\ cm^2$). However, at higher ion energies (250 and 325 eV), the ion-induced damage led to the formation of nanodots on the GaSb surface, as depicted in figure 2 and figure 3. The nanodot formation indicates the presence of the Ga rich amorphous layer as has been reported in the literature[17-19] that results in high contact resistances. Hence, as can be seen in figure 4, the best contact is obtained for an optimum compromise between oxide removal and ion-induced damage. The variation in ρ_c for a given ion energy is most likely due to the ion-induced damage of the semiconductor surface and the interface reaction between Ti and GaSb[20]. Note that in this study, the AJA sputtering and evaporation system has low ion density, in the range of 10^7-10^8 ion cm^{-3}. Thus, the estimated projectile Ar^+ fluence was in the range of 10^{13} ion cm^{-2}, which is much lower than the ion fluence threshold of 1×10^{16} ion cm^{-2} for Sb_2O_3 removal and of $> 7 \times 10^{16}$ ion cm^{-2} for Ga_2O_3 removal reported by El-Atwani *et al.*[6,7].

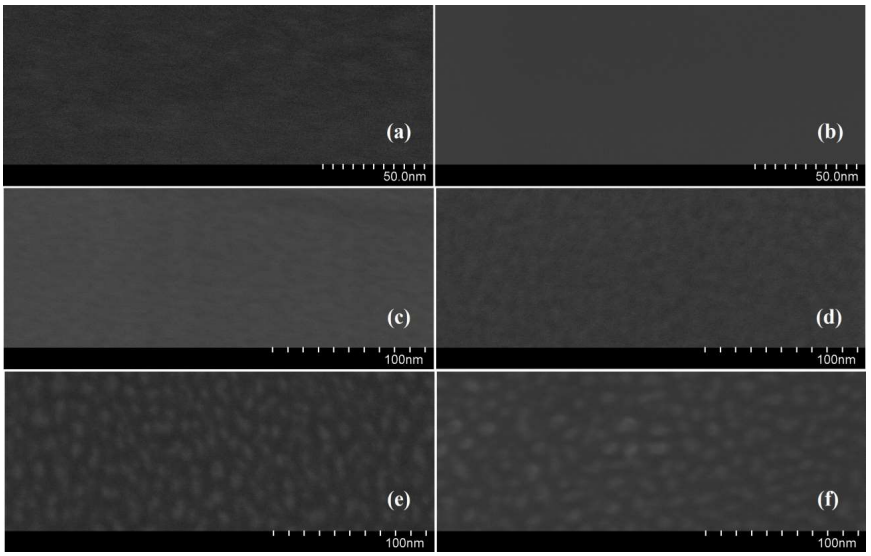

Figure 2. Scanning electron micrographs of GaSb surface after argon irradiation at (a) non-treatment, (b) 70 eV, (c) 120 eV, (d) 180 eV, (e) 250 eV and (f) 325 eV.

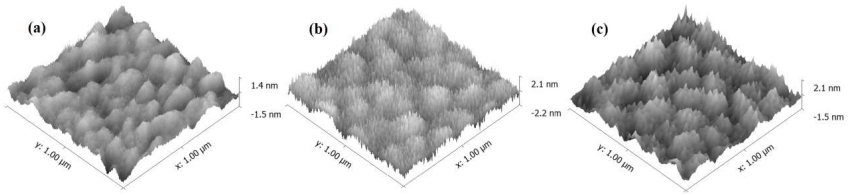

Figure 3. Atomic force micrographs of GaSb surface after argon irradiation at (a) 180 eV, (b) 250 eV and (c) 325 eV with RMS values of 0.34 nm, 0.52 nm, and 0.44 nm, respectively.

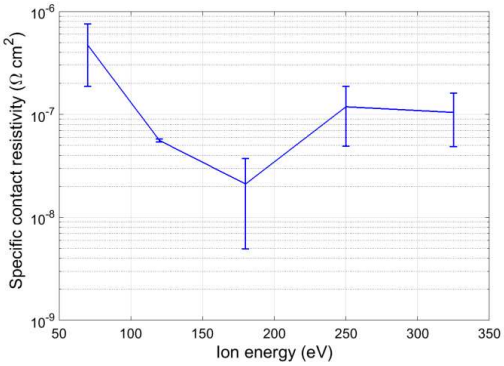

Figure 4. The effect of Argon ion energy on the contact properties of p-GaSb via the measurement of specific contact resistivity (average value with the standard deviation shown as error bars). We note that all measured values of the specific contact resistivity for 180 eV ion energy are less than 5×10^{-8} Ω cm^2.

Among plasma-assisted treatment techniques, surface treatment by BCl_3/Ar etching (treatment 3) is non-preferable due to a relatively high contact resistance and poor adhesion. This is most likely due to residual oxide and possibly the presence of chlorine-containing residues after BCl_3 ICP-RIE[21]. As opposed to this, surface treatment by H_2/Ar etching (treatment 2) led to extremely low specific contact resistivity and good adhesion between metallic layers and p-GaSb. We believe this is due to an oxide-free and high quality GaSb surface after the treatment.

IV. SUMMARY AND CONCLUSIONS

In this work, different plasma-assisted techniques were performed prior to metallization to remove the native oxide of epitaxially grown p-GaSb. The effects of these pre-treatment techniques on the electric contact and adhesion properties were compared with that of conventional chemical methods by evaluating the specific contact resistivities between the metallic layers and p-GaSb. The surface pre-treatment using H_2/Ar etching and low-ion-energy Ar^+ irradiation led to extremely low specific contact resistivities with value below the limit of TLM for accurate value determination. In Ar^+ irradiation surface pre-treatment, optimization of the argon ion energy is required to sufficiently remove GaSb native oxide while minimizing the ion-induced damage of the semiconductor surface. The use of *in situ* Ar^+ irradiation eliminates sample exposure to the air, thus making it a promising technique for high performance GaSb-based semiconductor devices.

ACKNOWLEDGMENTS

The authors would like to acknowledge the Norwegian University of Science and Technology for support (from the Strategic Area Materials program) and the Research Council of Norway

for the support to this work (Grant 177610/V30) and to the Norwegian Micro- and Nano-Fabrication Facility, NorFab (Grant 197411/V30).

REFERENCES

[1]Z. Y. Liu , B. Hawkins, and T.F. Kuech, *J. Vac. Sci. Technol. B* **21**, 71 (2003).
[2]A. Nainani, Y. Sun, T. Irisawa, Z. Yuan, M. Kobayashi et al., *J. Appl. Phys.* **109**, 114908 (2011).
[3]P. H. C. Magnée, S. G. den Hartog, B. J. van Wees, T. M. Klapwijk, W. van de Graaf, and G. Borghs, *Appl. Phys. Lett.* **67**, 3569 (1995).
[4]M. F. Millea, A. H. Silver, and L. D. Flesner, *Thin Solid Films* **56**, 253 (1979).
[5]F. Y. Soldatenkov et al., *Semiconductors* **45**, 1219 (2011).
[6]O. El-Atwani, J. P. Allain, and S. Ortoleva, *Nucl. Instr. Methods Phys. Res. B* **272**, 210 (2012).
[7]O. El-Atwani, J. P. Allain, and A. Suslova, *Appl. Phys. Lett.* **101**, 251606 (2012).
[8]E. R. Cleveland, L. B. Ruppalt, B. R. Bennett, and S. M. Prokes, *Appl. Surf. Sci.* **277**, 167 (2013).
[9]Z. Lu, Y. Jiang, W. I. Wang, M. C. Teich, and R. M. Osgood, *J. Vac. Sci. Technol. B* **10**, 1856 (1992).
[10]R. P. H. Chang, C. C. Chang, and S. Darack, *J. Vac. Sci. Technol.* **20,** 45 (1982).
[11]J. A. Gupta, P. J. Barrios, J. Lapointe, G. C. Aers, and C. Storey, *Appl. Phys. Lett.* **95**, 041104 (2009).
[12]A. Ducanchez, L. Cerutti, A. Gassenq, P. Grech, and F. Genty, *IEEE J. Sel. Top. Quantum Electron.* **14**, 1014 (2008).
[13]B. Tadayon, C. S. Kyono, M. Fatemi, S. Tadayon, and J. A. Mittereder, *J. Vac. Sci. Technol. B* **13,** 1 (1995).
[14]N. Rahimi, A. A. Aragon, O. S. Romero, D. M. Kim et al., *Proc. of SPIE*, 8620 (2013).
[15]D. K. Schroder, *Semiconductor Material and Device Characterization* (Wiley-IEEE Press, New Jersey, 2006).
[16]P. S. Dutta, K. S. Sangunni, H. L. Bhat, and V. Kumar, *Appl. Phys. Lett.* **65,** 1695 (1994).
[17]C. Palacio, J. Olvera, J. L. Plaza, and E. Diéguez, *Surf. Coat. Technol.* **206**, 3146 (2012).
[18]S. Facsko, T. Dekorsy, C. Koerdt, C. Trappe, H. Kurz, A. Vogt, and H. L. Hartnagel, *Science* **285**, 1551 (1999).
[19]S. Facsko, T. Bobek, H. Kurz, T. Dekorsy, S. Kyrsta, and R. Cremer, *Appl. Phys. Lett.* **80**, 130 (2002).
[20]A. Vogt, A. Simon, J. Weber, H. L. Hartnagel, J. Schikora, V. Buschmann, and H. Fuess, *Mater. Sci. Eng. B* **66**, 199 (1999).
[21]S. J. Pearton, in *Handbook of Compound Semiconductors*, edited by P. H. Holloway and G. E. McGuire (William Andrew Inc., New Jersey, 1996).

5.4. Paper 4 – Aluminum-based contacts for use in GaSb-based diode lasers

Authors: **Thanh-Nam Tran**, Saroj Kumar Patra, Magnus Breivik, and Bjørn-Ove Fimland

First published in: *Journal of Vacuum Science & Technology B* 34, 061207 (2016)

DOI: 10.1116/1.4967300

Contributions: MB conceived the initial research idea and **TNT** planned the study under the supervision of BOF. **TNT** performed the experimental works related to the fabrication of TLM structures and Fabry-Perot laser diodes. **TNT** performed measurements of specific contact resistivity of TLM structures and output characteristics of laser devices. SKP grew samples using MBE and performed structural and optical characterizations on these. MB developed the first recipe for laser processing and the recipe was later optimized by **TNT**. **TNT** did all data analysis, drafted the first version of the manuscript, discussed it with other authors, and finalized it.

Abstract

Aluminum-based contacts could be a good alternative to conventional gold-based contacts for a number of GaSb-based devices. In this study, the use of some Al-based contacts in GaSb-based diode lasers was investigated via the measurement of specific contact resistivity and laser output characteristics. The Al-based contacts to p-type GaSb(001) exhibited lower specific contact resistivities than the conventional Au-based contacts, whereas the opposite was the case for contacts to n-type GaSb(001). The good performance of GaSb-based laser diodes using Al-based contacts shows the applicability of this type of contact in GaSb-based devices. The contact between Al only and p-type GaSb(001), however, could suffer from a reliability problem when used in diode lasers, due to interdiffusion, in which case a diffusion barrier should be included.

I. INTRODUCTION

GaSb-based diode lasers are one of the promising monochromatic light sources in the mid-infrared wavelength region of 2-5 μm. The high-performance operation of these devices requires ohmic contacts with ultra-low resistivity to enhance the current injection and to minimize the heat generation in the laser structures in order to minimize Auger recombination. Currently, Au-based contacts are predominantly used. Although aluminum contacts have been widely used in silicon integrated-circuits, it has not been reported in use in GaSb-based lasers. Thanks to excellent properties of aluminum, such as low electrical resistance and good contacting with wire bonds (both Au and Al wires), the Al-based contacts are promising as a cheaper alternative for GaSb-based devices.

Ti/Pt/Au ohmic contact to p-type GaSb(001) is widely chosen for a number of antimonide-based devices, including for GaSb-based diode lasers, and is a natural choice of Au-based contact that alternative Al-based contacts should be compared with. The specific contact resistivity of this metallization is typically in the order of 10^{-8} - 10^{-6} Ω cm^2 [1-3]. Since every deposited metal can create an ohmic contact to p-type GaSb(001),[4,5] Al can be used as single-element metallization system. Milnes et al.[6] have investigated ohmic contacts to p-type GaSb(001), using Al amongst other metals. The authors showed that p-GaSb(001)/Al contact had a low specific contact resistivity which was comparable to those of Au and Ag contacts, but less stable after being heated for 30 h at temperatures from 200 °C and above. We believe the latter is due to the diffusion of Al into GaSb, in which case it can be avoided by adding a diffusion barrier. Ti is well-known as the diffusion barrier for the Al contacts to Si,[7] and thus Ti is our candidate for the diffusion barrier in Al contacts to GaSb. The formation of the intermetallic layer $TiAl_3$ at annealing temperatures above 300 °C which allows Al to diffuse through[7] is not expected to be an issue as long as the contact is annealed below 300 °C for a rather short time.

In contrast, the Schottky barrier due to the Fermi-level pinning at the surface near the valence band makes ohmic contacts to n-type GaSb(001) more difficult to obtain[8-10]. Forming ohmic contact to n-type GaSb(001) mostly bases on the formation of intermetallic compound

at the metal – semiconductor interface by the use of multilayer contacts and annealing[11]. The metals Pd and Ni are widely chosen to make intermetallic compound with n-type GaSb(001),[12-15] where the primary function is to initiate reactions with GaSb and to serve as an adhesion layer[5]. Ge can be used to create a highly doped n^+-GaSb layer in order to provide a tunneling contact[16]. Our choice of Au-based contact here, that alternative Al-based contacts should be compared with, is a specific Pd/Ge/Au/Pt/Au metal stack contact that has shown excellent performance[12]. Although an alternative Ni/Ge/Au/Pt/Au contact has shown even lower specific contact resistivity, we chose Pd over Ni as there is some uncertainty regarding how stable Ni would be as compared to Pd in long term thermal stability[12]. Utilizing the advantages of solid phase reaction of Pd/Ge contact, we propose an Al-based metallization system to n-type GaSb(001) consisting of Pd, Ge, Ti and Al.

In this work, the specific contact resistivities of Al-based contacts to p- and n-type GaSb(001) are measured and compared to those of the selected Au-based contacts. Subsequently, the use of these Al-based contacts in GaSb-based lasers is examined via the laser performance. Furthermore, the reliability of the Al-based contacts for laser applications is evaluated in a laser burn-in and life-time test.

II. EXPERIMENTS

1. Material growths

To determine the specific contact resistivity of Al-based contacts, the transfer length method (TLM) and four-probe measurements were performed on samples grown by molecular beam epitaxy (MBE)[3,17]. For the contacts to p-type GaSb(001), a 2 µm thick epitaxial layer of Be-doped GaSb was grown on a 100 nm thick undoped GaSb buffer layer grown on n-type GaSb(001) wafer (with nominal carrier concentration of 5×10^{17} cm^{-3}) in a solid source Varian GEN II Modular MBE system. The p-type doping concentration was 2×10^{19} cm^{-3}, which is a typical concentration for the cap layer of the laser structure. For the contacts to n-type GaSb(001), a 2 µm thick epitaxial layer of Te-doped GaSb was grown on semi-insulating GaAs(001) wafer. For the n-type sample, the nominal carrier concentration was 5×10^{17} cm^{-3}, which is similar to the carrier concentration of n-type GaSb(001) substrates used for laser growth.

The laser structure, shown schematically in Fig. 1, was grown in the above-mentioned MBE system equipped with Veeco valved cracker cells for both arsenic and antimony. The 2 µm thick lower cladding layer of n-type $Al_{0.9}Ga_{0.1}As_{0.06}Sb_{0.94}$ was doped with Te to a carrier concentration level of 1.6×10^{17} cm^{-3} for the first 1.6 µm and then the doping level was graded to a carrier concentration level of 1.0×10^{17} cm^{-3} over the next 400 nm toward the active region of the laser. The 2 µm thick upper cladding layer of p-type $Al_{0.9}Ga_{0.1}As_{0.06}Sb_{0.94}$ was Be-doped with a grading in carrier concentration from 2.0×10^{17} cm^{-3} to 5.0×10^{18} cm^{-3} over the first 400 nm and then constant doping with carrier concentration at 5.0×10^{18} cm^{-3} for the next 1.6 µm. The grading in carrier concentration was achieved by varying the temperature of dopant sources linearly with time. A 12 nm thick doped (nominal average carrier concentration of 4.1×10^{17} cm^{-3}) GaSb/AlSb superlattice structure was introduced within the Te-doped GaSb buffer layer on top of the Te-doped GaSb(001) substrate to minimize the propagation of any dislocation

defects towards the active region of the laser. The nominal carrier concentration in the Te-doped GaSb buffer layer and Te-doped GaSb(001) substrate was 5×10^{17} cm^{-3}. To help carrier injection, heavily doped graded bandgap transition layers were grown between the buffer layer and the n-type cladding layer and between the p-type cladding layer and the heavily doped p-type (Be dopant concentration of 2×10^{19} cm^{-3}) GaSb cap layer. The active region of the laser consisted of three 12 nm wide $In_{0.33}Ga_{0.67}As_{0.1}Sb_{0.9}$ quantum wells separated by 20 nm wide $Al_{0.35}Ga_{0.65}As_{0.026}Sb_{0.974}$ barriers and sandwiched between two 145 nm wide undoped $Al_{0.35}Ga_{0.65}As_{0.026}Sb_{0.974}$ separate confinement layers.

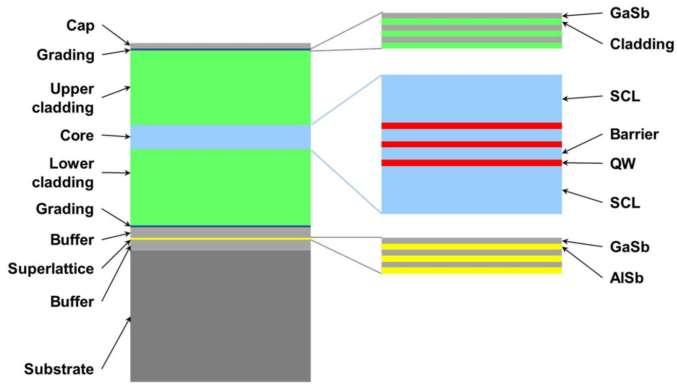

Figure 1. Schematic of the growth structure of the lasers. (Details are given in Sec. II A.)

2. Device fabrications

TLM structures were defined by conventional UV-lithography and were isolated on rectangular mesas by inductively-coupled plasma reactive ion etching (ICP-RIE)[3]. The metallization was performed by e-beam evaporation in a combined sputtering and e-beam evaporation system (AJA ATC-2200V) at a starting pressure of 10^{-7} Torr. The contact formation is summarized in Table I. Prior to metallization, *in situ* cleaning of the GaSb surface by low-ion-energy (325 eV) Ar^+ irradiation was applied to remove the native oxide[3]. After lift-off, the samples underwent a rapid thermal anneal at 290 °C for 45 s in nitrogen atmosphere, which is an optimized annealing procedure[12] for the n-type GaSb/Pd/Ge/Au/Pt/Au contact that we use as a comparison reference for the performance of Al-based contacts to n-type GaSb. For GaSb-based diode lasers, the optimized annealing procedure for contacts to n-type GaSb is simultaneously also applied for the Ti/Pt/Au contacts to p-type GaSb during laser fabrication. As our Al-based contacts to n-type GaSb also include Pd/Ge, we thus use the same annealing procedure for all annealed contacts. Samples of non-annealed Al contact to p-type GaSb(001) were also prepared to investigate the effect of Al diffusion on the contact properties.

Ridge-waveguide lasers using Al-based and Au-based contacts with 25 µm wide strips, as shown in Fig. 2, were processed using ICP-RIE (Oxford Plasma System 100 ICP380 reactor) with BCl_3/Cl_2 chemistry. The etch stop was controlled precisely, as described in detail in Ref.

18, to 100 nm above the active region, using *in situ* reflectance monitoring. For mesa passivation, photoresist ma–N440 was spin-coated followed by thermal hardening and RIE etchback with O_2/CF_4 chemistry. The metallization of the laser contacts presented in Fig. 2 and Table II were performed as in the specific contact resistivity experiments, except using an optimized Ar ion energy of 180 eV to remove GaSb native oxide[3]. To achieve good bonding to the aluminum contact, 50 nm of SiO_2 was added to improve the adhesion between photoresist and Al. In addition, a thick layer of Al is required to reduce the bonding force. We observed non-lasing behavior of the laser when the bonding force exceeded 80 g. After top contact metallization, the laser samples were thinned down to about 150 µm before applying the bottom contact metallization. Finally, all lasers were annealed following the mentioned annealing procedure and were cleaved into 1.5 mm long laser bars before being mounted episide-up on copper heat sinks. No facet coating was applied. The laser diodes were characterized in continuous wave operation at 16 °C, lasing at 2.29 µm wavelength. The reliability of the Al-based contacts was examined in a laser burn-in and life-time test. The test conditions are summarized in Table II. Laser properties such as output power and I-V characteristic were recorded to evaluate the contact reliability.

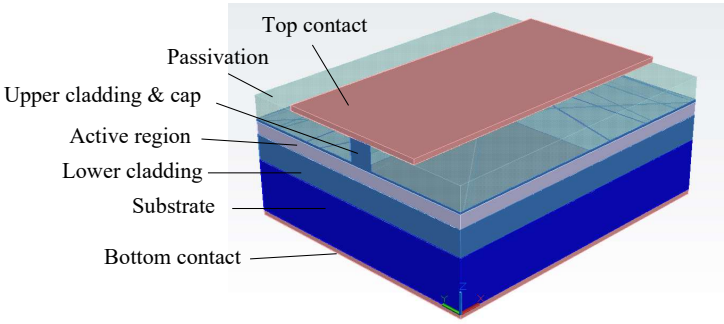

Figure 2. 25 µm wide ridge-waveguide laser using different types of contacts. **Laser A**: Al top contact and Pd/Ge/Ti/Al bottom contact. **Laser TA**: Ti/Al top contact and Pd/Ge/Ti/Al bottom contact. **Laser TPA**: Ti/Pt/Au top contact and Pd/Ge/Au/Pt/Au bottom contact.

III. RESULTS AND DISCUSSIONS

The Al-based contacts to both p- and n-type GaSb(001) exhibited low specific contact resistivity and comparable to the Au-based contacts. The results are summarized in Table I.

Similar to Ti[5], Al can react with p-type GaSb, even at room temperature[18], to provide good ohmic contact. However, unlike the contact between Ti and p-type GaSb(001), where the contact resistivity is not affected by annealing[14], the interdiffusion between Al and p-type GaSb(001) during annealing improves the contact resistivity. After annealing, the measured value of ρ_c for the Al contact to p-type GaSb(001) is lower than both for the as-deposited Al

contact and for the Au-based contact. It is one of the lowest reported results for contact to p-type GaSb(001). However, it is also quite a bit below the lower limit (5×10^{-8} Ω cm^2 in this case[3]) for accurate/valid results of the measurement method, and thus, there is a relatively high uncertainty attached to this value. This is supported by the fact that the measurements of two out of three annealed Al samples gave negative contact resistances (R_c) with small absolute values similar to the positive contact resistance of the third sample, indicating that the TLM failed to accurately determine the extremely low specific contact resistivity of the Al contact to p-type GaSb after annealing. The metal contact to p-type GaSb(001) consisting of Ti and Al also exhibited a very low specific contact resistivity which is unexpectedly lower than that of the Au-based contact, even though Ti is the first deposited metal in both cases.

Table I. Contact preparation and the measured specific contact resistivity for each metallization. N: number of samples.

Contact	Metallization	N	Thickness (Å)	Average ρ_c (Ω cm^2)
p-type GaSb	Non-annealed Al	3	2000	7.8×10^{-8} (for N=3)
	Annealed Al	3	2000	1.4×10^{-8} (for N=1[a])
	Ti/Al	3	500/2000	2.0×10^{-8} (for N=3)
	Ti/Pt/Au	5	500/250/3250	10.5×10^{-8} (for N=5)
n-type GaSb	Pd/Ge/Al	3	87/560/2000	3.3×10^{-3} (for N=3)
	Pd/Ge/Ti/Al	3	87/560/500/2000	2.6×10^{-3} (for N=3)
	Pd/Ge/Au/Pt/Au	3	87/560/233/476/2000	1.2×10^{-3} (for N=3)

[a]Measurement results of the other samples gave negative contact resistances with small absolute values similar to the positive contact resistance (R_c), and thus there is a relatively high uncertainty attached to the listed value.

For the contacts to n-type GaSb(001), an ohmic behavior was observed from I – V curves in all samples. The Au-based contact showed the lowest average ρ_c while the Al-based contact using Ti as a diffusion barrier showed a slightly lower average ρ_c than the Al-based contact without Ti. The observed high value of ρ_c for both Au-based and Al-based contacts is likely due to the low doping level (i.e. carrier concentration) of the n-type GaSb epilayer. Consequently, the value of ρ_c would improve if the carrier concentration in the n-GaSb epi-layer was increased. This, however, is not applicable for the case of GaSb-based lasers as fabricated in this study as high quality n-type GaSb(001) wafers with much higher carrier concentration (e.g. above 2×10^{18} cm^{-3}) are in general not commercially available.

The representative output power and current-voltage characteristics of as-fabricated lasers are shown in Fig. 3. All lasers exhibit similar performance. Compared to the lasers with Au-based contacts (Laser TPA), the lasers with Al-based contacts (Laser A and Laser TA) had higher resistance, most likely due to the bottom contact.

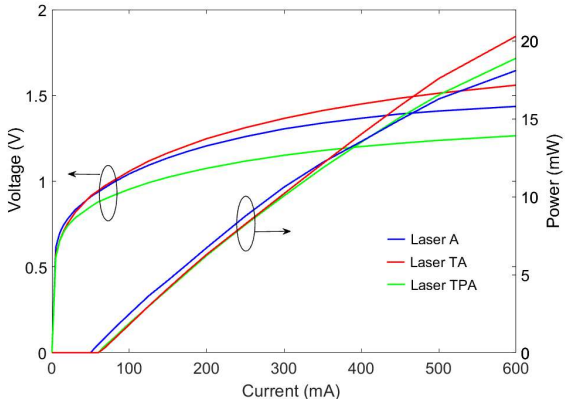

Figure 3. Representative output power and current-voltage characteristics of as-fabricated lasers. (Laser A: Al top contact, Laser TA: Ti/Al top contact, Laser TPA: Ti/Pt/Au top contact).

After the burn-in test, no degradation, as judged by output power, was observed from any of the lasers. Some lasers with Laser A contacts had even higher output power than as-fabricated devices. After the life-time test, the output power of lasers with Laser A contacts degraded ca. 5-15%, whereas the lasers with Laser TA or Laser TPA contacts showed no degradation. The degradation in output power of the lasers with Laser A contacts was attributed to an increase in the total resistance of the laser (see Fig. 4), probably due to Al diffusion during burn-in causing a degradation of the top contact. We believe the Ti in the Laser TA top contact reduces the Al diffusion during the life-time test, and thus prevents degradation of the lasers with Laser TA contacts. Finally, we note that using the TiAl top contact in combination with the conventional PdGeAuPtAu bottom contact should potentially give an even better laser diode performance than demonstrated here.

Table II. Reliability test for GaSb-based laser diodes using different types of contacts.

Test	Type of laser	Contacts (Top/Bottom)	Number of samples	Time (h)	Current density (A/cm^2)	Output power after testing
First:	Laser A	Al/PdGeTiAl	5	100	800	No degradation
Burn-in	Laser TA	TiAl/PdGeTiAl	4	100	800	No degradation
(16 °C)	Laser TPA	TiPtAu/PdGeAuPtAu	3	100	800	No degradation
Second:	Laser A	Al/PdGeTiAl	5	100	1200	5-15% degradation
Life-time	Laser TA	TiAl/PdGeTiAl	4	100	1200	No degradation
(80 °C)	Laser TPA	TiPtAu/PdGeAuPtAu	3	100	1200	No degradation

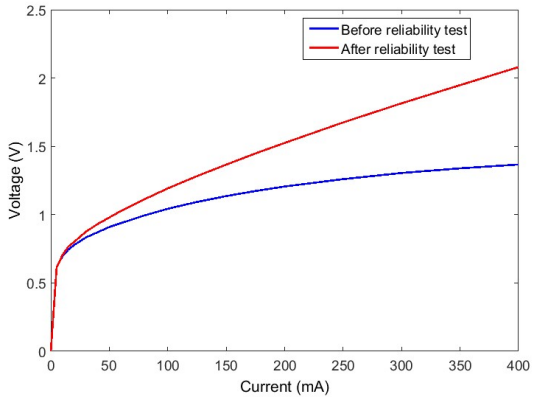

Figure 4. Typical I-V characteristic of lasers with Laser A contacts before and after reliability test.

IV. CONCLUSIONS

We found that the Al-based contacts to p-type GaSb(001) exhibited around five times lower specific contact resistivities than the conventional Au-based contacts, whereas the opposite (two-three times higher) was the case for contacts to n-type GaSb(001). However, as revealed by our reliability test, the contact between Al only and p-type GaSb(001) could suffer from a reliability problem when used in some devices, due to interdiffusion, in which case a diffusion barrier should be included. The GaSb-based laser diodes with TiAl/PdGeTiAl top/bottom contacts proved to have equally good performance, in terms of power output and reliability, as the laser diodes with conventional TiPtAu/PdGeAuPtAu top/bottom contacts, which is promising with regard to the applicability of Al-based contacts in GaSb-based devices.

ACKNOWLEDGMENTS

The authors would like to acknowledge the Norwegian University of Science and Technology (NTNU) for support (from the Strategic Area Materials program) and the Research Council of Norway for the support to this work (Grant 177610/V30) and to the Norwegian Micro- and Nano-Fabrication Facility, NorFab (Grant 197411/V30).

REFERENCES

[1]B. Tadayon, C. S. Kyono, M. Fatemi, S. Tadayon, and J. A. Mittereder, J. Vac. Sci. Technol. B **13**, 1 (1995).

[2]F. Y. Soldatenkov, S. V. Sorokina, N. K. Timoshina, V. P. Khvostikov, Y. M. Zadiranov, M. G. Rastegaeva, and A. A. Usikova, Semiconductors **45**, 1219 (2011).

[3]N. T. Tran, S. K. Patra, M. Breivik, and B. -O. Fimland, J. Vac. Sci. Technol. B **33**, 061210 (2015).

[4]J. O. McCaldin, T. C. McGill, and C. A. Mead, J. Vac. Sci. Technol. **13**, 802 (1976).

[5]A. Vogt, A. Simon, J. Weber, H. L. Hartnagel, J. Schikora, V. Buschmann, and H. Fuess, Mater. Sci. Eng. B **66**, 199 (1999).

[6]A.G. Milnes, M. Ye, and M. Stam, Solid State Electron. **37**, 37 (1994).

[7]M. Lawrence, and A. Dass, *Characterization in Silicon Processing*, edited by Y. Strausser (Butterworth-Heinemann, Boston, 1993).

[8]W. E. Spicer, I. Lindau, P. Skeath, C. Y. Su, and P. Chye, Phys. Rev. Lett. **44**, 420 (1980).

[9]Z. M. Lü, D. Mao, L. Soonckindt, and A. Kahn, J. Vac. Sci. Technol. A **8**, 1988 (1990).

[10]K. M. Schirm, P. Soukiassian, P.S. Mangat, and L. Soonckindt, Phys. Rev. B **49**, 5490 (1994).

[11]D. G. Ivey, Platinum Metals Rev. **43**, 2 (1999).

[12]N. Rahimi, A. A. Aragon, O. S. Romero, D. M. Kim, N. B. J. Traynor, T. J. Rotter, G. Balakrishnan, S. D. Mukherjee, and L. F. Lester, Proc. SPIE **8620**, 86201K (2013).

[13]W. S. Tse, R. H. Chen, C. S. A. Fang, and J. R. Chen, Appl. Phys. A **54**, 556 (1992).

[14]A. Vogt, H. L. Hartnagel, G. Miehe, H. Fuess, and J. Schmitz, J. Vac. Sci. Technol. B, **14**, 3514 (1996).

[15]J. A. Robinson, and S. E. Mohney, J. Appl. Phys. **98**, 033703 (2005).

[16]A. Vogt, A. Simon, H. L. Hartnagel, J. Schikora, V. Buschmann, M. Rodewald, H. Fuess, S. Fascko, C. Koerdt, and H. Kurz, J. Appl. Phys. **83**, 7715 (1998).

[17]D. K. Schroder, *Semiconductor Material and Device Characterization* (Wiley-IEEE Press, New Jersey, 2006).

[18]N. T. Tran, M. Breivik, S. K. Patra, and B. -O. Fimland, Proc. SPIE 9134, 91342E (2014).

[19]W. Oueini, M. Rouanet, and J. Bonnet, Surf. Sci. 409, 445 (1998).

5.5. Paper 5 – Widely tunable Y-junction lasers at 2.34 – 2.39 µm wavelength for trace-gas sensing applications

Authors: **Thanh-Nam Tran**, Saroj Kumar Patra, Magnus Breivik, Kjetil Haddeland, and Bjørn-Ove Fimland

Submitted to IEEE Photonics Technology Letters (ID: PTL-39988-2023)

Contributions: BOF and MB conceived the initial research idea and **TNT** planned the study under the supervision of BOF. **TNT** performed the experimental works related to the fabrication and characterization of the output characteristics of Y-junction laser diodes. SKP grew samples using MBE and performed structural characterizations. MB developed the first recipe for laser processing and the recipe was later optimized by **TNT**. KH performed the mask design for Y-junction lasers. **TNT** did all data analysis, drafted the first version of the manuscript, discussed it with other authors, and finalized it.

Abstract

Widely tunable Y-junction lasers have been realized in the wavelength range of 2.34 - 2.39 µm for trace-gas sensing application. Y-junction structures with large bend radius and small length difference between the two cavities have been chosen to maximize the output power and wavelength tunability while having sufficient side mode suppression ratio (SMSR). By changing the electric currents in different sections of the Y-junction lasers, a tunable wavelength range of 50 nm with an SMSR > 23 dB was achieved.

Keywords: Tunable diode lasers, Y-junction, mid-infrared, Gallium Antimonide (GaSb), side mode suppression ratio (SMSR)

I. INTRODUCTION

GaSb-based type-I semiconductor diode lasers with high optical gain, simple growth design and easy approach to continuous wave (cw) operation at room temperature (RT) are excellent candidates for mid-infrared lasers in the wavelength region of 1.5-3.3 µm [1-3], whose applications include the monochromatic light sources needed for trace-gas sensing systems based on tunable diode-laser absorption spectroscopy (TDLAS). Among edge-emitting laser structures for light source of TDLAS, Y-junction structure is an interesting alternative, thanks to its wide tunable range and less complex fabrication process. Most of widely tunable monolithic laser structures benefit from passive gratings and phase sections, requiring epitaxial regrowth of the laser structure [4]. This regrowth could be performed for GaSb-based laser structures [5], but has to overcome the reactive nature of AlGaAsSb [6] used for the cladding layers. Y-junction lasers provide a regrowth-free solution, using less complex processing steps and tools (such as conventional photolithography), resulting in potentially lower costs and higher yield. First studied by Wang, Choi and Fattah [7, 8], the Y-junction lasers were later further developed by other groups focusing on optical communication applications [9-13]. Recently, tunable lasers using Y-junction [14, 15] or related structures such as Mach-Zehnder (MZ) interferometer [16-19], V-coupled cavity [20], modulated grating Y-branch [21] and multimode interference couplers [22, 23] have been investigated, typically for gas sensing and communication applications. For the regrowth-free, low-cost tunable lasers, a tuning range of up to 55 nm and an SMSR exceeding 30 dB have been reported for the wavelength region of 1.5-1.6 µm [18, 22-24].

In the present work, the ridge waveguide Y-junction structure, which can be considered a "half MZ interferometer", consists of two S-bend cavities with same bending radius sharing a common section, as shown in Fig. 1, but where one S-bend cavity is shorter due to a shorter bend section. The geometrical path difference ΔL allows the selection of the overlapped modes (supermodes) between two mode-combs of these two cavities, called the Vernier effect, thus enabling the interferometric tuning behavior of the Y-junction lasers when the mode-comb of one cavity is shifted relative to the other. Here, Y-junction lasers of different configuration (i.e., different bend radii r and ΔL) have been fabricated and characterized. The main goal is to maximize wavelength tuning range while keeping the SMSR sufficient for gas detection [25].

With the tuning range of 2.34 – 2.39 µm, several targeted gas molecules can be detected such as CH_4 and CO, which have strong absorption lines in this wavelength regime [26-28].

II. EXPERIMENTS

In this study, GaInAsSb/AlGaAsSb quantum well (QW) diode lasers emitting at 2.3 µm wavelength were grown on n-type GaSb (001) wafer by molecular beam epitaxy (MBE). The active region consisted of three 12 nm wide $Ga_{0.67}In_{0.33}As_{0.10}Sb_{0.90}$ QWs separated by 20 nm wide quaternary $Al_{0.35}Ga_{0.65}As_{0.026}Sb_{0.974}$ barrier layers and sandwiched between two 145 nm wide undoped $Al_{0.35}Ga_{0.65}As_{0.026}Sb_{0.974}$ separate confinement layers. For optical and electrical confinement, the active region was surrounded by n- and p-type doped $Al_{0.90}Ga_{0.10}As_{0.06}Sb_{0.94}$ cladding layers with the thickness of 2 and 1.4 µm, respectively. The carrier concentration in the cladding layers has been optimized to enhance the laser performance [29].

5 µm wide ridge Y-junction lasers, with locally symmetric Y-splitter structure and with different bend radii r and length differences ΔL, were processed into the structure shown schematically in Fig. 1. For the loss characterization in the Y-junction structure, straight lasers with the same waveguide width were also fabricated for comparison. To improve the light confinement in the Y-junction structure, especially in the bend sections, a deep etch (within 100 nm above the active region) is important. The etch depth can be precisely controlled by *in situ* reflectance monitoring [30]. For the contact planarization and waveguide sidewall isolation, photoresist ma-N440 was spin-coated followed by thermal hardening and O_2/CF_4 Reactive Ion Etching etchback. Prior to metallization, *in situ* cleaning of the GaSb surface by optimal-ion-energy (180 eV) Ar^+ irradiation was applied to remove the native oxide [31]. The conventional gold-based contacts, Ti/Pt/Au and Pd/Ge/Au/Pt/Au, were used for top and bottom laser contacts, respectively, followed by annealing. The lasers were cleaved into bars of 1.5 mm before being mounted epi-side-up on copper heat sinks. The laser diodes were characterized in cw operation at 16 °C without any facet coatings.

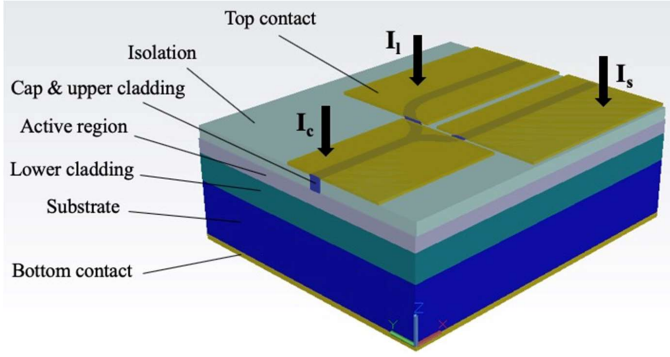

Figure 1. Schematic of a fabricated Y-junction laser with three top electrodes for current injection, where I_c, I_s and I_l are the injected currents for the common section, the shorter arm and the longer arm, respectively.

III. RESULTS AND DISCUSSIONS

Fig. 2 shows the output power characteristics of Y-junction lasers with different bend radii where all three currents were kept identical. The typical Y-junction laser (r = 1000 µm, ΔL = 20 µm) exhibits a relatively high threshold current density J_{th} of 1140 A/cm^2 (380 A/cm^2 per well) compared to the straight waveguide lasers (J_{th} = 750 A/cm^2). A significant contribution to the high threshold current density is the bend losses not found in the straight laser structures. The inset in Fig. 2 displays the single-mode behavior of the Y-junction lasers emitting at 2.37 µm with an SMSR of 25 dB. The laser linewidth or the full width at half maximum (FWHM) of laser peak is measured to be ~0.1 nm which is suitable for high accuracy gas sensing applications as simulated by Chan et al. [32]. The characteristic temperature (T_0) of 84.3 K measured from straight waveguide lasers of the same laser growth structure indicates a good thermal stability of the devices.

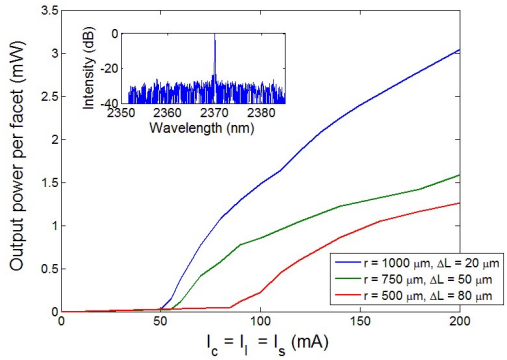

Figure 2. Output performance of the Y-junction lasers with different bend radii. Single-mode emission with SMSR = 25 dB is shown in the upper inset, recorded for the Y-junction configuration with r = 1000 µm and ΔL = 20 µm. (See Fig. 1 for definition of I_c, I_l and I_s.)

The design of the bend section in the Y-junction structure significantly affects the performance of the final devices in terms of output power and wavelength tunability. As the bend radius decreases, the optical losses due to leakage in the bend section and the mode mismatch between the straight and bent waveguide segments increases, resulting in higher total loss and lower output power [33, 34], as seen in Fig. 2. Moreover, for a given waveguide separation, the bend radius also determines the length difference ΔL between two cavities in the asymmetric Y-junction structure. The larger the bend radius, the smaller ΔL can be, and thus a higher tuning range, given by $\Delta\lambda_Y = \lambda^2/2n_{g,eff}\Delta L$ where $n_{g,eff}$ is the effective group index, can be achieved. Therefore, larger bend radius is preferable to maximize the output power and the tuning range. With $n_{g,eff}$ = 3.75 (determined from mode spacing measurements), the theoretical tuning range of the Y-junction lasers with the largest r = 1000 µm and ΔL = 20 µm in this study is $\Delta\lambda_Y$= 36.5 nm, which is in agreement with the experimental results presented

in Fig. 3(a) (i.e., by keeping $I_c = I_s = 120$ mA and varying I_l, the tuning range is 37 nm with an average tuning rate of 0.6 nm/mA). The drawback of the Y-junction configuration is the tradeoff between increased tuning range and the associated reduction in SMSR [11]. However, a typical SMSR of 23 dB and up to 25 dB is obtained in this work, which satisfies the requirement for trace-gas sensing application.

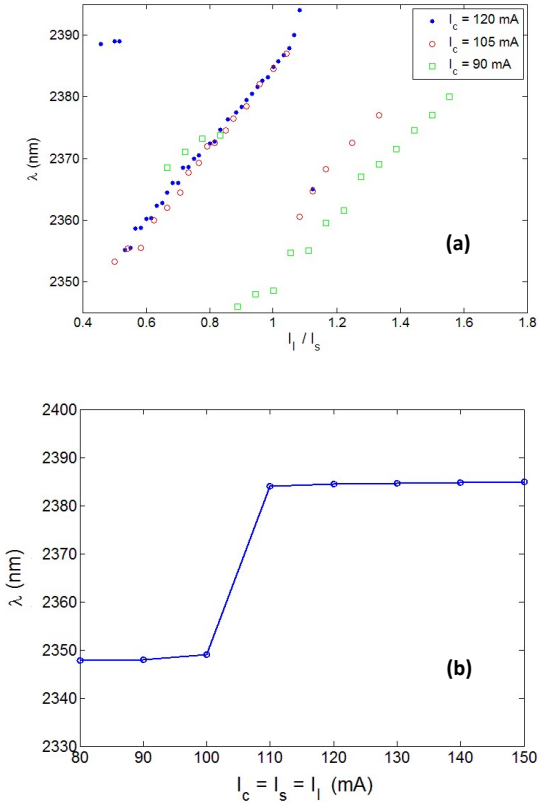

Figure 3. Tuning behavior of Y-junction laser with r = 1000 µm and ΔL = 20 µm. **(a)** Variation of the MZ filter across the FP modes. **(b)** Variation of the whole gain curve across the MZ filter.

The tuning behavior of the Y-junction lasers has been characterized as shown in Fig. 3. By adjusting the injection currents into each section, the emitted wavelength can be tuned in two different ways which allow the largest variety of controllable applications [11]. The first tuning scheme is based on the variation of the MZ filter across the Fabry-Perot (FP) modes. By varying the ratio of the injection currents into the longer arm (I_l) and the shorter arm (I_s), the sawtooth-shaped tuning behavior can be observed as shown in Fig. 3(a) when the position of the MZ loss minimum is tuned across the allowed FP modes (continuous tuning) until the neighboring

minimum reaches the same low level (step-like tuning). The single-mode lasing spectra with a tuning range of 32 nm covered in steps of 1-3 nm is displayed in Fig. 4. By combining with variations of the injected current into the common section (I_c), a wide tuning range of up to 50 nm can be obtained. This would be advantageous as it can enable several gases to be detected by one single laser. The second tuning scheme is achieved by changing all of the injected currents simultaneously (usually equal) to shift the whole gain curve across the MZ filter. Step-like tuning behavior can be observed, as shown in Fig. 3(b), resulting from the switch of the supermode when the level of the next MZ loss minimum has reached the value of the previous one.

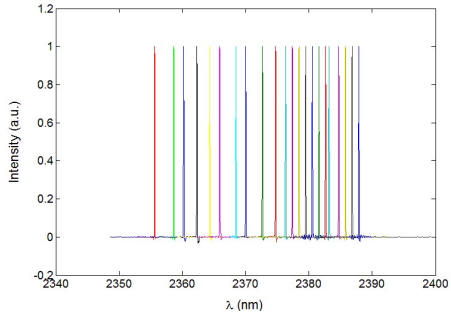

Figure 4. Single-mode lasing spectra (with normalized peak intensities) of the Y-junction laser (r = 1000 µm, ΔL = 20 µm) with a 32 nm tuning range.

IV. CONCLUSIONS

Tunable Y-junction lasers lasing at 2.34 – 2.39 µm wavelength have been successfully fabricated and characterized. A single-mode emission tuning range as wide as 50 nm is demonstrated for Y-junction laser with bend radius of 1000 µm and length difference of 20 µm between the two cavities. In addition, the devices exhibit good output performance in terms of power, FWHM and SMSR that makes Y-junction laser a promising candidate for trace-gas sensing applications.

REFERENCES

[1] G. Almuneau, F. Genty, A. Wilk, P. Grech, A. Joullié, and L. Chusseau, "GaInSb/AlGaAsSb strained quantum well semiconductor lasers for 1.55 µm operation," *Semicond. Sci. Technol.*, vol. 14, no. 1, pp. 89, Jan. 1999, doi: 10.1088/0268-1242/14/1/014.

[2] T. Hosoda, G. Kipshidze, L. Shterengas, and G. Belenky, "Diode lasers emitting near 3.44 µm in continuous-wave regime at 300K," *Electron. Lett.*, vol. 46, no. 21, pp. 1455-1457, Oct. 2010, doi: 10.1049/el.2010.2564.

[3] E. Tournié, and A. N. Baranov, "Mid-infrared semiconductor lasers," in *Advances in Semiconductor Lasers* (Semiconductor and Semimetals series), vol. 86, J. J. Coleman, A. C. Bryce, and C. Jagadish, Eds. New York, NY, USA: Academic, 2012, p. 183.

[4] J. Buus, M. C. Amann, and D. J. Blumenthal, *Tunable diode lasers and related optical sources*, Hoboken, NJ, USA: John Wiley & Sons, Inc., 2005, pp. 169-220.

[5] Q. Gaimard, M. Triki, T. N. -Ba, L. Cerutti, G. Boissier, R. Teissier, A. Baranov, Y. Rouillard, and A. Vicet, "Distributed feedback GaSb based laser diodes with buried grating: a new field of single-frequency sources from 2 to 3 μm for gas sensing applications," *Opt. Express*, vol. 13, no. 15, pp. 19118-19128, Jul. 2015, doi: 10.1364/OE.23.019118.

[6] M. Reason, B. Bennett, R. Magno, and J. B. Boos, "Molecular Beam Epitaxial Regrowth of Antimonide-Based Semiconductors," *J. Electron. Mater.*, vol. 40, no. 1, pp. 6-10, Jan. 2011, doi: 10.1007/s11664-010-1399-6.

[7] S. Wang, H. K. Choi, and I. H. A. Fattah, "Studies of semiconductor lasers of the interferometric and ring types," *IEEE J. Quantum Electron.*, vol. 18, no. 4, pp. 610-617, Apr. 1982, doi: 10.1109/JQE.1982.1071587.

[8] I. H. A. Fattah, and S. Wang, "Semiconductor interferometric laser," *Appl. Phys. Lett.*, vol. 41, no. 2, pp. 112-114, Jul. 1982, doi: 10.1063/1.93444.

[9] M. Schilling, H. Schweizer, K. Dütting, W. Idler, E. Kühn, A. Nowitzki, and K. Wünstel, "Widely tunable Y-coupled cavity integrated interferometric injection laser," *Electron. Lett.*, vol. 26, no. 4, pp. 243-244, Feb. 1990, doi: 10.1049/el:19900163.

[10] M. Schilling, W. Idler, E. Kühn, G. Laube, H. Schweizer, K. Wünstel, and O. Hildebrand, "Integrated interferometric injection laser: novel fast and broad-band tunable monolithic light source," *IEEE J. Quantum Electron.*, vol. 2727, no. 6, pp. 1616-1624, Jun. 1991, doi: 10.1109/3.89985.

[11] K. Dütting, O. Hildebrand, D. Baums, W. Idler, M. Schilling, and K. Wünstel, "Analysis and simple tuning scheme of asymmetric Y-lasers," *IEEE J. Quantum Electron.*, vol. 30, no. 3, pp. 654-659, Mar. 1994, doi: 10.1109/3.286151.

[12] O. Hildebrand, W. Idler, K. Dütting, G. Laube, and K. Wünstel, "The Y-laser: a multifunctional device for optical communication systems and switching networks," *J. Lightwave Technol.*, vol. 11, no. 12, pp. 2066-2075, Dec. 1993, doi: 10.1109/50.257971.

[13] M. Kuznetsov, P. Verlangieri, A. G. Dentai, C. H. Joyner, and C. A. Burrus, "Asymmetric Y-branch tunable semiconductor laser with 1.0 THz tuning range," *IEEE Photon. Technol. Lett.*, vol. 4, no. 10, pp. 1093-1095, Oct. 1992, doi: 10.1109/68.163743.

[14] R. Bugge, and B. -O. Fimland, "A novel tunable wet etched mid-IR pentenary AlInGaAsSb junction laser at 2.34-2.44 μm," in *Proc. DRC'05*, Santa Barbara, CA, USA, 2005, doi: 10.1109/DRC.2005.1553035.

[15] A. Lyakh, R. Maulini, A. Tsekoun, R. Go, and C. K. N. Patel, "Continuous wave operation of buried heterostructure 4.6μm quantum cascade laser Y-junctions and tree arrays," *Opt. Express*, vol. 22, no. 1, pp. 1203-1208, Jan. 2014, doi: 10.1364/OE.22.001203.

[16] M. C. Zheng, P. Q. Liu, X. Wang, J. -Y. Fan, M. Troccoli, and C. F. Gmachl, "Wide single-mode tuning in quantum cascade lasers with asymmetric Mach-Zehnder interferometer type cavities with separately biased arms," *Appl. Phys. Lett.*, vol. 103, no. 21, pp. 211112, Nov. 2013, doi: 10.1063/1.4832337.

[17] P. Q. Liu, X. Wang, and C. F. Gmachl, "Single-mode quantum cascade lasers employing asymmetric Mach-Zehnder interferometer type cavities," *Appl. Phys. Lett.*, vol. 101, no. 16, pp. 161115, Oct. 2012, doi: 10.1063/1.4761247.

[18] M. Dernaika, L. Caro, N. P. Kelly, M. Shayesteh, and F. H. Peters, "Tunable L-band semiconductor laser based on Mach–Zehnder interferometer," *Opt. Commun.*, vol. 402, pp. 56-59, Nov. 2017, doi: 10.1016/j.optcom.2017.05.073.

[19] S. Latkowski, A. Hänsel, P. J. van Veldhoven, D. D'Agostino, H. Rabbani-Haghighi, B. Docter, N. Bhattacharya, P. J. A. Thijs, H. P. M. M. Ambrosius, M. K. Smit, K. A. Williams, and E. A. J. M. Bente, "Monolithically integrated widely tunable laser source operating at 2 μm," *Optica*, vol. 3, no. 12, pp. 1412-1417, Dec. 2016, doi: 10.1364/OPTICA.3.001412.

[20] J. Jin, L. Wang, T. Yu, Y. Wang, and J. -J. He, "Widely wavelength switchable V-coupled-cavity semiconductor laser with ∼40 dB side-mode suppression ratio," *Opt. Lett.*, vol. 36, no. 21, pp. 4230-4232, Nov. 2011, doi: 10.1364/OL.36.004230.

[21] J. –O. Wesstrom, G. Sarlet, S. Hammerfeldt, L. Lundqvist, P. Szabo, and P. –J. Rigole, "State-of-the-art performance of widely tunable modulated grating Y-branch lasers," in *Proc. OFC 2004*, Los Angeles, CA, USA, 2004. [Online]. Available: https://ieeexplore.ieee.org/document/1359295

[22] D. D'Agostino, D. Lenstra, H. Ambrosius, and M. Smit, "Widely tunable multimode-interference based coupled cavity laser with integrated interferometer," *Opt. Express*, vol. 26, no. 11, pp. 14159-14173, May 2018, doi: 10.1364/OE.26.014159.

[23] L. Caro, M. Dernaika, N. P. Kelly, P. E. Morrissey, J. K. Alexander, and F. H. Peters, "An Integration-Friendly Regrowth-Free Tunable Laser," *IEEE Photon. Technol. Lett.*, vol. 30, no. 3, pp. 270-272, Feb. 2017, doi: 10.1109/LPT.2017.2781799.

[24] M. Nawrocka, Q. Lu, W. -H. Guo, A. Abdullaev, F. Bello, J. O'Callaghan, T. Cathcart, and J. F. Donegan, "Widely tunable six-section semiconductor laser based on etched slots," *Opt. Express*, vol. 22, no. 16, pp. 18949-18957, Aug. 2014, doi: 10.1364/OE.22.018949.

[25] Y. Rouillard, S. Belahsene, M. Jahjah, G. Boissier, P. Grech, G. Narcy, A. Vicet, L. Naehle, M. v. Edlinger, M. Fischer, and J. Koeth, "Quantum well lasers emitting between 3.0 and 3.4 μm for gas spectroscopy," in *Proc. SPIE OPTO*, vol. 8268, San Francisco, CA, USA, 2012, doi: 10.1117/12.905881.

[26] I. E. Gordon, L. S. Rothman, R. J. Hargreaves, R. Hashemi, E. V. Karlovets, F. M. Skinner, E. K. Conway, C. Hill, R. V. Kochanov, Y. Tan, P. Wcisło, A. A. Finenko et al., "The HITRAN2020 molecular spectroscopic database," *J. Quant. Spectrosc. Radiat. Transf.*, vol. 277, p. 107949, Jan. 2022, doi: 10.1016/j.jqsrt.2021.107949.

[27] M. Jahjah, S. Moumdji, O. G. -Lafaye, S. Bonnefont, Y. Rouillard, and A. Vicet, "Antimonide-based 2.3 μm photonic crystal coupled-cavity lasers for CH_4 QEPAS," *Electron. Lett.*, vol. 48, no. 5, pp. 277-278, Mar. 2012, doi: 10.1049/el.2011.3614.

[28] E. V. Stepanov, S. N. Kotelnikov, A. Y. Stavtsev, and S. G. Kasoev, "The best absorption lines for the detection of carbon monoxide at 2.35 micron with tunable diode lasers," *J. Phys.: Conf. Ser.*, vol. 1560, p. 012053, 2020, doi: 10.1088/1742-6596/1560/1/012053.

[29] S. K. Patra, T. -N. Tran, L. Vines, I. Kolevatov, E. Monakhov, and B. -O. Fimland, "Dopant incorporation in $Al_{0.9}Ga_{0.1}As_{0.06}Sb_{0.94}$ grown by molecular beam epitaxy," *J. Cryst. Growth*, vol. 463, pp. 116-122, Apr. 2017, doi: 10.1016/j.jcrysgro.2017.01.035.

[30] T. -N. Tran, M. Breivik, S. K. Patra, and B. -O. Fimland, "High precision AlGaAsSb ridge-waveguide etching by in situ reflectance monitored ICP-RIE," in *Proc. SPIE Photonics Europe*, vol. 9134, Brussels, Belgium, 2014, doi: 10.1117/12.2052615.

[31] T. -N. Tran, S. K. Patra, M. Breivik, and B. -O. Fimland, "Plasma-assisted oxide removal from p-type GaSb for low resistivity ohmic contacts," *J. Vac. Sci. Technol. B*, vol. 33, no. 6, pp. 061210, Oct. 2015, doi: 10.1116/1.4935883.

[32] K. L. Chan, Z. Ning, D. Westerdahl, K. C. Wong, Y. W. Sun, A. Hartl, and M. O. Wenig, "Dispersive infrared spectroscopy measurements of atmospheric CO_2 using a Fabry–Pérot interferometer sensor," *Sci. Total Environ.*, vol. 472, pp. 27-35, Feb. 2014, doi: 10.1016/j.scitotenv.2013.10.105.

[33] J. Wang, W. Yuan, C. S. Seibert, and D. C. Hall, "Loss characterization of high-index-contrast ridge waveguide oxide-confined InAlGaAs quantum well racetrack ring-resonator lasers," in *Proc. SPIE OPTO*, vol. 7230, San Jose, CA, USA, 2009, doi: 10.1117/12.807871.

[34] M. Breivik, "Fabrication of mid-infrared laser diodes for gas sensing applications," Ph.D. dissertation, Dept. Electron. Syst., Norwegian Univ. Sci. Technol., Trondheim, Norway, 2013.

Chapter 6

SUMMARY AND FUTURE OUTLOOK

6.1. Summary

The goal of this thesis work is to optimize the fabrication process of GaSb-based laser diodes in order to successfully fabricate and characterize tunable Y-junction lasers for trace-gas sensing applications. The process optimization focusing on carrier concentration in the cladding layers, waveguide formation and insulation, oxide-removal techniques, metallization of laser contacts and facet coating is summarized in section 6.1.1. As seen in section 6.1.2 below, the optimized processing steps show positive impact on the laser output characteristics, as evidenced by the performance of Fabry-Perot lasers with different configurations. Furthermore, the successful development of Y-junction lasers is presented, featuring operation in cw mode at room temperature with wide tuning range up to 50 nm and SMSR > 23 dB.

6.1.1. Optimization of GaSb-based laser diode fabrication process

The laser structures were grown by molecular beam epitaxy and several growth steps needed to be optimized in order to improve the laser characteristics. My contribution was to support the laser growth optimization through the discussions, fabrication and characterization of the tested structures. In section 5.1, incorporation of tellurium (Te) and beryllium (Be) dopants in $Al_{0.9}Ga_{0.1}As_{0.06}Sb_{0.94}$ cladding layers was investigated to enhance the electrical properties while minimizing the defect levels for better optical properties. The dependence of carrier concentration and Hall mobility on dopant density for both n- and p-type doped AlGaAsSb cladding layers has been precisely determined using Hall effect and SIMS depth profile measurements. Carrier concentration was found to have linear dependence on the dopant density for Be-doped $Al_{0.9}Ga_{0.1}As_{0.06}Sb_{0.94}$ for dopant density up to 2.9×10^{19} cm^{-3}, whereas it gets saturated for Te-doped $Al_{0.9}Ga_{0.1}As_{0.06}Sb_{0.94}$ samples at 1.6×10^{17} cm^{-3} for dopant density values above 8.0×10^{18} cm^{-3}. Deep level transient spectroscopy revealed the presence of deep trap levels (most likely DX-centers) as a cause of low doping efficiency in the Te-doped $Al_{0.9}Ga_{0.1}As_{0.06}Sb_{0.94}$ samples. Other works of laser growth optimization not included in this thesis are studies of doping profile in the cladding layer and indium interdiffusion into barrier due to annealing.

Our group have established a standard recipe for the fabrication of the semiconductor laser diodes. Based on the first recipe developed by Breivik [61], the significant improvements of the laser processing achieved in this work include ridge-waveguide formation, waveguide isolation, metallization and facet coating with further details given below.

Ridge-waveguide formation

Ridge-waveguide structure has been fabricated in a well-defined form. Using photoresist AZ-5214E as a mask for etching, nearly vertical profile of 85° of ridge waveguide has been obtained. Simulations results in section 5.2 and Appendix A show the importance of ridge waveguide etching to obtain high index contrast for waveguiding in Y-junction structure with high bend loss. To control precisely the etch depth or the height of the ridge waveguide, *in situ* reflectance monitored ICP-RIE has been applied providing an endpoint depth precision within ± 10 nm. Using this high precision etching technique, significant improvement in the performance of Y-junction lasers has been achieved as compared to previous studies in our group.

Waveguide insulation

By covering the sidewall of the ridge waveguide with the photoresist ma-N440 followed by heat treatment and O_2/CF_4 RIE etchback, rapid oxidation of the cladding layer AlGaAsSb can be avoided, thus improving the long-term reliability of the laser devices. The reliability tests of the laser diodes presented in section 5.4 showed no degradation of the output power, which is partly attributed to this protection. We believe that the photoresist ma-N440 can replace the expensive materials which are normally used for waveguide isolation in laser fabrication, e.g., benzocyclobutene (BCB).

Metallization

Low ohmic contact resistance to GaSb is highly desirable for high performance operation of the laser diodes. Such good ohmic contact requires an oxide-free surface of GaSb, which is in contact with the metallic layers. Prior to metallization, several plasma-assisted techniques were applied to remove the native oxide of GaSb, as presented in section 5.3. The effect of these techniques on the contact properties in comparison to the conventional chemical methods was evaluated via the specific contact resistivity between the metallic layers and p-type GaSb, obtained from transfer length method and four-point probe measurements. Very low specific contact resistivities of less than $5 \times 10^{-8}\ \Omega\ cm^2$ (the limit for accurate TLM measurement results) were observed after pre-surface treatment by H_2/Ar sputtering etching and low-ion-energy Ar irradiation. By eliminating sample exposure to air prior to metallization, *in situ* Ar irradiation is a promising technique for fabrication of high performance GaSb-based semiconductor devices.

Study on aluminum (Al)-based metallizations to n- and p-type GaSb as an alternative for gold (Au)–based contacts provides better understanding in contact properties of the GaSb-based laser diodes, as presented in section 5.4. Measurement of specific contact resistivities between metallic layers and n-/p-type GaSb demonstrated that the Al-based contacts performed as good as the conventional Au-based contacts. The contact property between Al and p-type GaSb was even better after annealing. The potential reliability problem of this type of contact revealed by reliability test when used in some devices, due to interdiffusion, can be reduced by using a diffusion barrier. The good performance of GaSb-based straight waveguide edge emitting lasers

using Al-based contacts shows the applicability of this type of contact in GaSb-based semiconductor devices.

Facet coating

Optical coating on laser facets is a promising solution to improve the output performance and long-term stability of GaSb-based semiconductor laser diodes. In chapter 4, simulations of reflectance spectra have been performed for different optical coatings in order to select proper materials matching the requirement of reflectivity. The optical coatings were then deposited on glass and GaAs substrate by electron beam evaporation, of which glass substrate is used for testing the deposition method and GaAs has the refractive index closest to those of the laser materials. The reflectance spectra of the optical coatings were then measured by FTIR spectroscopy to compare with simulation results. At the desired wavelength of 2.33 µm, the reflectivities of the HR coating, AR coating and partial HR coating were measured to be 99 %, 7 % and 50 %, respectively. The effect of optical coatings on the performance of the GaSb-based edge emitting laser diodes has been examined. Significant improvement of the output performance of the laser diodes in terms of optical power, threshold current and differential quantum efficiency has been observed after applying one facet with HR coating and the other with AR coating.

6.1.2. Fabrication and characterization of Fabry-Perot and Y-junction lasers

Fabry-Perot and Y-junction lasers have been successfully fabricated using the optimized processing steps. The output performance of the lasers has been characterized via the measurement of P-I characteristics, I-V characteristics, laser spectrum, near- and far-field patterns. The long-term stability of the laser diodes has also been evaluated via reliability test.

The FP lasers with different configuration (i.e., straight and S-bend waveguide with different widths) have been processed for the characterization of laser growth structure and process optimization. FP ridge waveguide lasers with 25 µm width and 1 mm length operating at RT in cw mode with good output characteristics have been obtained, i.e., maximum output power per facet of 20 mW (without optical coating), low threshold current density of 200 $A \cdot cm^{-2}$ (67 $A \cdot cm^{-2}$ per quantum well), internal loss of 9.83 cm^{-1}, internal quantum efficiency of 40.6 % and characteristic temperature of 84.3 K. The laser diodes exhibited low operation voltage of 1 V which helped to reduce the heat generation inside the laser structure. Single mode behavior emission with FWHM of ~ 0.1 nm and SMSR > 14 dB has been observed for 5 µm wide (and below) straight waveguide. The loss characterization in the S-bend lasers was unsuccessful due to the inconsistency in measurement data, thus requiring further investigation.

Widely tunable Y-junction lasers have been realized in the wavelength range of 2.34 – 2.39 µm, as presented in section 5.5, to achieve the main goal of this thesis. Y-junction lasers of different configuration with different r (bend radius) and ΔL (length difference between two cavities) have been fabricated and characterized. The Y-junction structure with large r and small ΔL is preferable to maximize the output power and wavelength tunability while having sufficient SMSR for gas detection. We demonstrated a single-mode emission tuning range as wide as 50 nm of the Y-junction laser with an r of 1000 µm and a ΔL of 20 µm, of which the

tuning regime has behaved as expected. In addition, the devices exhibited good output performance in terms of power, FWHM and SMSR with the typical values of 2 mW, ~ 0.1 nm and 23 dB, respectively. Together with RT operation in cw mode, the fabricated Y-junction lasers have fulfilled the conditions of light source of TDLAS for trace-gas sensing applications [5].

6.2. Future outlook

Though optimization of fabrication process carried out in this work can lead to the successful operation of the Y-junction laser, it requires further research to improve its performance. Ideas and suggestions are presented in this section.

6.2.1. Computations and simulations of laser diodes

To date, the optimal output characteristics of the diode lasers are usually the results of experimentally optimizing the growth of laser materials and the device fabrication process, which involves various parameters and is a very complicated, costly and time-consuming process. Therefore, it would be more efficient to simulate the laser operation by varying the laser structural parameters, such as number of wells, width of wells… to optimize the output characteristics of the diode lasers prior to fabricating the devices. Whereas numerous experimental research works have been performed for strained GaInAsSb/AlGaAsSb QW diode lasers, theoretical studies of this laser system have received much less attention. With the development of advanced software simulation tools, it is possible to model such complex system prior to the growth and fabrication of devices. By integrating various models, including spontaneous and stimulated emission, Shockley-Read-Hall (SRH) recombination, Auger recombination, and strained zinc-blende three-band model, etc., simulation tools such as ATLAS can be utilized to replicate the output performance of the laser diodes. Moreover, several parameters can be also extracted from simulation results, such as near- and far-field patterns, optical loss, radiative recombination rate, SRH recombination rate, and Auger recombination rate. These output parameters provide a basis for a thorough analysis of the laser performance, thus enabling optimization of the design of the laser structures and the laser devices. For example, one could increase the compressive strain of the QW in the laser structure in order to reduce the Auger recombination rate, especially at the longer wavelengths.

6.2.2. Improvement of index contrast for waveguiding in Y-junction structure with high bend loss

Regardless the long-term reliability, the most straightforward approach to enhance the index contrast for waveguiding in Y-junction structure is etching through the active region. This will lead to pure index guiding mechanism for lateral mode confinement inside the ridge structure with a large index contrast of more than 1.5. However, the propagation of light in Y-junction structures could experience a high optical loss due to waveguide sidewall roughness. Particularly along the curved sections, the light scattering becomes severe as all propagating light hits the sidewalls and reflects back. We observed non-lasing behavior of Y-junction lasers

with small bend radii of 300 and 500 µm when etching through the active region. The working laser with large bend radii of 750 and 1000 µm performed worse than previous study (section 5.5). Therefore, it is essential to reduce the waveguide sidewall roughness to improve the performance of laser devices. The reduction of waveguide sidewall roughness is a result of the optimization of mask design and manufacture, waveguide formation lithography, and etching process. For as-etched waveguide, one can reduce the roughness of waveguide sidewalls by applying chemical treatments, such as phosphoric acid-based wet etch [140], or oxygen-enhanced wet thermal oxidation [141]. It should be noted that these chemical treatments were applied for III-As waveguides. Therefore, the effect of chemical treatments on the reduction of III-AsSb waveguide sidewall roughness require further investigation.

An alternative approach to increase the index contrast for waveguiding in the ridge waveguide structure is to engineer the laser structure. One of the factors that can affect the index contrast is the thickness of the active region as shown in Eq. 2.21. Simulation results show that the index contrast can increase by decreasing the thickness of the active region. As seen in Fig. A.1, the index contrast can reach to the value of 0.14 when the thickness of the active region is 200 nm. The tradeoff of this method is increasing of light leakage into the cladding layers as the active region is too thin, as seen in Fig. A.2.

Another solution is to push the light toward the upper cladding by bringing the refractive index of the upper cladding closer to that of the active region. That means the light generated in the active region will be intentionally leaked toward the upper cladding as shown in Fig. A.3. In that case, the propagating light will be guided inside the ridge which has a much higher refractive index than that of the surrounding isolation layer. Again, the waveguide sidewall roughness needs to be controlled in order to minimize the light scattering at the sidewalls.

6.2.3. Investigation of other interferometric laser structures

Interferometric tuning mechanism plays an important role for realization of tunable laser diodes. An investigation into interferometric waveguide structures would result in further understanding of tuning behavior and improvement of tunability and SMSR of the lasers.

For Y-junction waveguide structure, the SMSR provided by the Y-junction structure may be not sufficient to ensure single mode operation for applications which require high spectral purity light sources. To improve SMSR of the Y-junction laser, one can add a grating structure similar to the DFB structure. Another solution is to use a three-branch (Y3) junction laser [55, 82]. The Y3-junction lasers improve over the conventional Y-junction lasers by simultaneously achieving a better SMSR and a wider tuning range. However, by adding one more waveguide, the control of currents in different waveguides becomes more complicated.

An interesting alternative is waveguide-coupling laser structures which consist of two lasers, a straight waveguide laser and an S-bend waveguide laser, which are slightly separated at one end of the cavities. The geometrical path difference ΔL creates two different mode-combs of these two lasers. When the separation gap is small enough, the light coupling between two lasers enables the interferometric tuning behavior when the mode-comb of one cavity is shifted relative to the other, known as Vernier effect. Initial results in Appendix D show that the tuning

range can be up to 45 nm depending on the current ratio in the bend and straight lasers and the separation gap. Further investigation in this laser structure can provide the thorough analysis regarding the light coupling mechanism between two lasers which can lead to the understanding of the tuning behavior of the laser devices.

Appendix A

SIMULATION RESULTS

This chapter contains results from simulation of lateral index contrast for waveguiding and mode confinement in ridge waveguide structure. The results may be helpful for optimization of light confinement inside the high-loss Y-junction waveguide. Simulation results in Fig. A.1 was achieved by ERIM, see in chapter 2, using MATLAB. The simulations in Fig. A.2 and Fig. A.3 were performed using LIGHTS – Online optical simulation software by Sarangan [142].

In Fig. A.1, the dependence of the effective refractive index contrast Δn_{eff} on the thickness of the active region, calculated by ERIM, are shown. The ERIM simulation is applied for $\lambda = 2.33$ µm, $n_2 = n_{core} = 3.523$, $n_1 = n_{cladding} = 3.25$, $n_0 = n_{insulation} = 1.5$, and the etch stop is at the interface between the upper cladding and the active region. The maximum value of index contrast is 0.14 when the thickness of the active region is 200 nm. However, as the thickness of the active region reduces to 200 nm, the leakage of light into the cladding layers can increase in comparison to our current laser structure with the thickness of the active region of 366 nm, as shown in Fig. A.2 (a) and (b).

In Fig. A.3, the light generated in the active region is intentionally leaked into the upper cladding for better waveguiding if the refractive index of the upper cladding layer is closer to that of the active region. Here, the simulation was applied for the refractive index of the active region of 3.523 and the refractive index of the upper cladding of 3.55. However, it is still a challenge to find the material composition for the upper cladding with such refractive index while having higher bandgap than that of the active region.

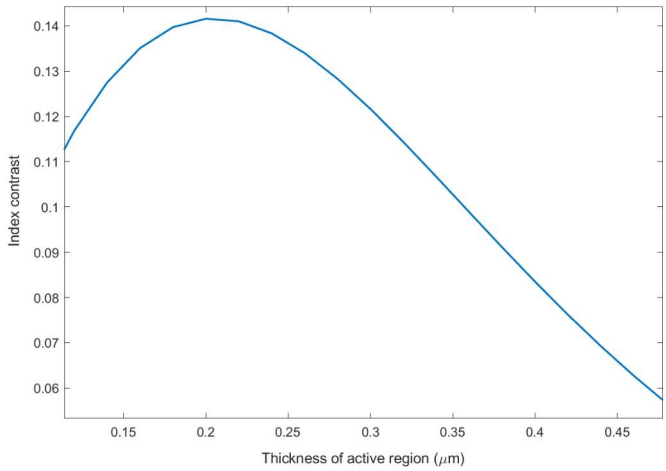

Figure A.1: The dependence of the effective refractive index contrast Δn_{eff} on the thickness of the active region. The ERIM simulation is applied for λ = 2.33 μm, $n_{active\ region}$ = 3.523, $n_{cladding}$ = 3.25, $n_{insulation}$ = 1.5, and the etch stop is at the interface between the upper cladding and the active region. It should be noted that for our laser growth and fabrication, the index contrast is approximately 0.09, corresponding to 366 nm thickness of the active region.

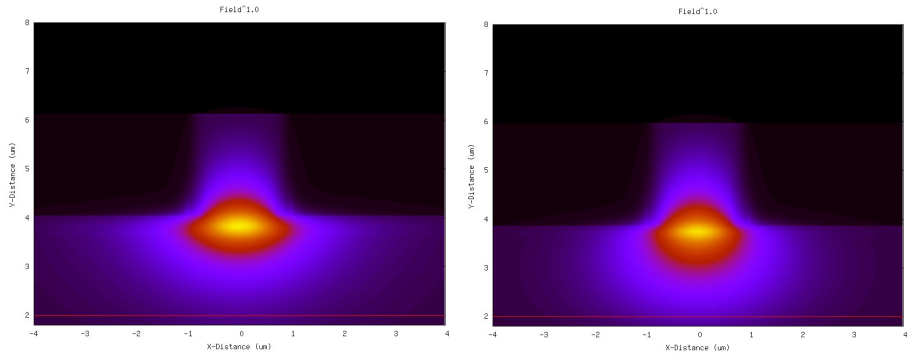

(a) (b)

Figure A.2: The mode confinement inside the ridge waveguide structure when etch stop is at the interface between the upper cladding and the active region. The simulation is applied for λ = 2.33 μm, $n_{active\ region}$ = 3.523, $n_{cladding}$ = 3.25, $n_{insulation}$ = 1.5. (a) Our current laser structure with the thickness of the active region of 366 nm. (b) Laser structure with the thickness of the active region of 200 nm.

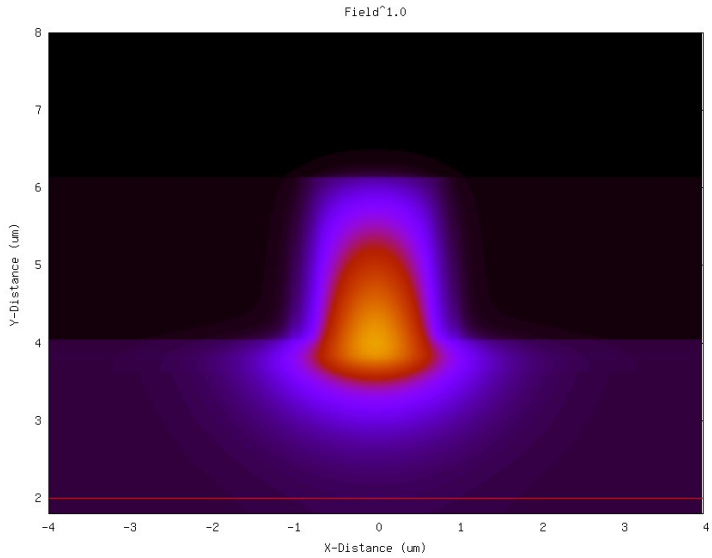

Figure A.3: Intentional leakage of light into the upper cladding layer for better waveguiding. The simulation is applied for $\lambda = 2.33$ µm, $n_{active\ region} = 3.523$, $n_{lower\ cladding} = 3.25$, $n_{upper\ cladding} = 3.55$, and $n_{insulation} = 1.5$.

Appendix B

LASER GROWTH STRUCTURES

This chapter contains the growth structures of Sb159, Sb176, Sb188, Sb308 and Sb309. Sample Sb308 and Sb309 has the same growth structures.

Table B.1. Layer information for the nominal laser structure of sample Sb159 emitting at 2.23 µm. The carrier concentrations in the grading layers and superlattice layer are the carrier concentrations that would have resulted for doped GaSb.

Layer	Material composition	Thickness (nm)	Type of doping / Carrier concentration (cm^{-3})	Growth temp. (°C)
Substrate	GaSb	5.0×10^5	n-type / 5.0×10^{17}	-
Buffer	GaSb	130	n-type / 5.0×10^{17}	530
30×superlattice	AlSb/GaSb	0.1/0.3	n-type 4.1×10^{17}	530
Buffer	GaSb	250	n-type / 5.0×10^{17}	530
Grading	AlGaAsSb/GaSb	42	n-type / 5.0×10^{17} → 1.6×10^{17}	530
Lower cladding	$Al_{0.9}Ga_{0.1}As_{0.06}Sb_{0.94}$	2.0×10^3	n-type / 1.6×10^{17} → 1.0×10^{17}	530
SCL	$Al_{0.35}Ga_{0.65}As_{0.025}Sb_{0.975}$	165	Intrinsic	400
MQW × 3	$Ga_{0.65}In_{0.35}As_{0.1}Sb_{0.9}$	10	Intrinsic	400
Barrier × 2	$Al_{0.35}Ga_{0.65}As_{0.025}Sb_{0.975}$	20	Intrinsic	400
SCL	$Al_{0.35}Ga_{0.65}As_{0.025}Sb_{0.975}$	165	Intrinsic	400
Upper cladding	$Al_{0.9}Ga_{0.1}As_{0.06}Sb_{0.94}$	2.0×10^3	p-type / 2.0×10^{17} → 5.0×10^{18}	400
Grading	AlGaAsSb/GaSb	42	p-type / 5.0×10^{18} → 5.0×10^{19}	400
Cap	GaSb	100	p-type / 2.0×10^{19}	400

Table B.2. Layer information for the nominal laser structure of sample Sb176 emitting at 2.4 μm. The carrier concentrations in the grading layers and superlattice layer are the carrier concentrations that would have resulted for doped GaSb.

Layer	Material composition	Thickness (nm)	Type of doping / Carrier concentration (cm^{-3})	Growth temp. (°C)
Substrate	GaSb	5.0×10^5	n-type / 5.0×10^{17}	-
Buffer	GaSb	130	n-type / 5.0×10^{17}	530
30×superlattice	AlSb/GaSb	0.1/0.3	n-type / 4.1×10^{17}	530
Buffer	GaSb	250	n-type / 5.0×10^{17}	530
Grading	AlGaAsSb/GaSb	42	n-type / 5.0×10^{17} → 1.6×10^{17}	530
Lower cladding	$Al_{0.9}Ga_{0.1}As_{0.06}Sb_{0.94}$	1.6×10^3	n-type / 1.6×10^{17} → 1.0×10^{17}	530
SCL	$Al_{0.35}Ga_{0.65}As_{0.025}Sb_{0.975}$	162	Intrinsic	430
MQW × 3	$Ga_{0.67}In_{0.33}As_{0.1}Sb_{0.9}$	14	Intrinsic	430
Barrier × 2	$Al_{0.35}Ga_{0.65}As_{0.025}Sb_{0.975}$	17	Intrinsic	430
SCL	$Al_{0.35}Ga_{0.65}As_{0.025}Sb_{0.975}$	162	Intrinsic	430
Upper cladding	$Al_{0.9}Ga_{0.1}As_{0.06}Sb_{0.94}$	1.4×10^3	p-type / 2.0×10^{17} → 5.0×10^{18}	350
Grading	AlGaAsSb/GaSb	42	p-type / 5.0×10^{18} → 5.0×10^{19}	350
Cap	GaSb	100	p-type / 2.0×10^{19}	350

Table B.3. Layer information for the nominal laser structure of sample Sb188 emitting at 2.25 μm. The carrier concentrations in the grading layers and superlattice layer are the carrier concentrations that would have resulted for doped GaSb

Layer	Material composition	Thickness (nm)	Type of doping / Carrier concentration (cm^{-3})	Growth temp. (°C)
Substrate	GaSb	5.0×10^5	n-type / 5.0×10^{17}	-
Buffer	GaSb	130	n-type / 5.0×10^{17}	520
30×superlattice	AlSb/GaSb	0.1/0.3	n-type / 4.1×10^{17}	520
Buffer	GaSb	250	n-type / 5.0×10^{17}	520
Grading	AlGaAsSb/GaSb	42	n-type / 5.0×10^{17} → 1.6×10^{17}	520
Lower cladding	$Al_{0.9}Ga_{0.1}As_{0.06}Sb_{0.94}$	2.0×10^3	n-type / 1.6×10^{17} → 1.0×10^{17}	520
SCL	$Al_{0.35}Ga_{0.65}As_{0.025}Sb_{0.975}$	145	Intrinsic	430
MQW × 3	$Ga_{0.67}In_{0.33}As_{0.1}Sb_{0.9}$	12	Intrinsic	430
Barrier × 2	$Al_{0.35}Ga_{0.65}As_{0.025}Sb_{0.975}$	20	Intrinsic	430
SCL	$Al_{0.35}Ga_{0.65}As_{0.025}Sb_{0.975}$	145	Intrinsic	430
Upper cladding	$Al_{0.9}Ga_{0.1}As_{0.06}Sb_{0.94}$	1.4×10^3	p-type / 2.0×10^{17} → 5.0×10^{18}	370
Grading	AlGaAsSb/GaSb	42	p-type / 5.0×10^{18} → 5.0×10^{19}	370
Cap	GaSb	100	p-type / 2.0×10^{19}	370

Table B.4. Layer information for the nominal laser structure of sample Sb308 and Sb309 emitting at 2.3 μm. The carrier concentrations in the grading layers and superlattice layer are the carrier concentrations that would have resulted for doped GaSb.

Layer	Material composition	Thickness (nm)	Type of doping / Carrier concentration (cm^{-3})	Growth temp. (°C)
Substrate	GaSb	5.0×10^5	n-type / 5.0×10^{17}	-
Buffer	GaSb	130	n-type / 5.0×10^{17}	520
30×superlattice	AlSb/GaSb	0.1/0.3	n-type / 4.1×10^{17}	520
Buffer	GaSb	250	n-type / 5.0×10^{17}	520
Grading	AlGaAsSb/GaSb	42	n-type / 5.0×10^{17} → 1.6×10^{17}	520
Lower cladding	$Al_{0.9}Ga_{0.1}As_{0.06}Sb_{0.94}$	2.0×10^3	n-type / 1.6×10^{17}	520
SCL	$Al_{0.35}Ga_{0.65}As_{0.025}Sb_{0.975}$	165	Intrinsic	430
MQW × 3	$Ga_{0.67}In_{0.33}As_{0.1}Sb_{0.9}$	12	Intrinsic	430
Barrier × 2	$Al_{0.35}Ga_{0.65}As_{0.025}Sb_{0.975}$	20	Intrinsic	430
SCL	$Al_{0.35}Ga_{0.65}As_{0.025}Sb_{0.975}$	165	Intrinsic	430
Upper cladding	$Al_{0.9}Ga_{0.1}As_{0.06}Sb_{0.94}$	2.0×10^3	p-type / 5.0×10^{18}	350
Grading	AlGaAsSb/GaSb	42	p-type / 5.0×10^{18} → 5.0×10^{19}	350
Cap	GaSb	100	p-type / 2.0×10^{19}	350

Appendix C

LASER PROCESSING RECIPE

The following pages contain the recipe used for processing of Fabry – Perot and Y-junction lasers. These parameters in this recipe were applying under normal conditions, but they could be changed to compensate for problems during the processing (i.e. instrument calibration, source changes…). The process requires various instruments and typically takes several weeks from start to finish.

Processing Run Card for laser fabrication

Sample:

Sample nr: _____
Sketch of sample:

1. Ridge-waveguide Etching

Sample Clean 1. 5 min in Acetone 2. 5 min in Ethanol 3. 5 min in Isopropalnol (IPA) 4. IPA rinse 5. Deionized water (DIW) rinse + immediate N_2 dry 6. Dehydration bake 150 ^oC / 10 min	Comments:
Photolitography – Ridge formation 1. Spin AZ 5214E @ 4000 rpm for 46 s 2. Clean backside of sample carefully with a swab moisted with acetone if photoresist (PR) is present 3. Soft bake 110 ^oC / 50 s 4. Edge bead removal with exposure dose of 700 mJ/cm^2 5. Develop in AZ 726 MIF until edge bead is gone followed by spin dry + softbake 6. Exposure - 150 mJ/cm^2. Hard contact for better sidewall profile. 7. Develop in AZ 726 MIF for 20-25 s (Varies from run to run, keep an eye on it, always use a test) 8. Spin dry @ 1000 rpm / 45 s	Comments: Estimated thickness: 1.4 µm

ICP-RIE etch
 	
1. Check that it has been used for Cl-gases
    1. If not, run the necessary cleaning steps
2. Do condition run w/o sample
    1. Use recipe developed by Oxford.
3. Do test run with test sample (preferably cladding sample)
4. Check etch rate and etch depth from test sample
5. Etch to desired etch depth (typically 100 nm above core) using Endpoint Detection (control etch depth with high accuracy)
6. PR removal
    1. Remove PR by putting sample in acetone (5-15 min)
	Comments:
	(etch depth, rates, selectivity, etc)

1. If not removed - use acetone gun or swabs 2. Rinse immediately in IPA + N_2 dry 7. Rinse sample in running DIW for 5 min (Cl-removal)	

2. Passivation

a. SiO_2

Sample Clean 1. Acetone + IPA rinse + N_2 dry 2. 5 min dehydration bake @ 150 ºC on hot plate	Comments:
PECVD 1. Deposit 100 nm SiO_2 in PECVD	Comments: (Deposited thickness, dep. rate)

b. Resist

Do for all samples

Sample Clean 1. Acetone + IPA rinse + N_2 dry 2. 5 min plasma clean 3. 10 min dehydration bake 150 ºC	Comments:
Resist 1. Spin ma-N 440 @ 7000 rpm / 30 s (for better edge bead) 2. Soft bake: 60 s @ 95 ºC 3. Do not expose the sample!! 4. Place sample on 3" Si wafer on black ceramic hot plate @ 100 ºC 5. Ramp to 160 C, bake at 160 C for 5 minutes 6. Start timer for 2 minutes, ramp to 260 ºC (TC) 7. Take off sample after 3 minutes (including ramp time, so approx 1 min at 260 ºC) 8. Run 1st annealing step by Rapid thermal processing (RTP)	Comments: Without cleaning can cause uneven PR etchback -> Clean residual PR.
Etch Back, RIE 1. Do condition run for 10-30 minutes (plasma should be yellow not blue) 2. Etch sample(s), recipe: "O_2 resist etch 100W" for 10-12 minutes until ridge is clean	Comments:

1. Do many etches, e.g. 1-2 minutes, and check result every time (microscope / profilometer) 3. Inspect in microscope/profilometer to make sure ridge is uncovered 4. Do Si_3N_4/SiO_2 etch if sample has oxide/nitride passivation 1. Recipe: CHF_3 ... (33 sccm Ar, 17 sccm CHF_3 or other way around)	

3. Top contact layer

Sample Clean 1. Acetone + IPA rinse + N_2 dry 2. 10 min dehydration bake 150 C	Comments:
Photolitograhy 1. Spin AZ 5214E @ 4000 rpm / 46 s 2. Softbake: 110 ºC / 50 s 3. Edge bead removal by flood exposure (150 x 5 mJ/cm^2) the edge of sample (sample was covered by a piece of Si except the edge). Remove PR at the edge by developer 4. Align and expose: ca. 18 mJ/cm^2 5. Image reversal bake: 115 ºC / 120 s 6. Flood exposure: 200 mJ/cm^2 7. Develop in AZ 726 MIF: ca. 40 s 8. DIW rinse	Comments:
Metallization 1. Oxide removal : Ar sputter : 16W, 1 min. 2. Metallization: Ti/Pt/Au 50nm/50nm/600nm (for bonding).	Comments:
Lift-off 1. Put sample in closed acetone container for 1-2 h 2. If lift-off is not successfull, try following (stop when lift-off is done) 1. Spray sample with acetone gun 2. Ultrasonic in plastic beaker (max 20 min) 3. Acetone + swab 4. If nothing works, change recipe!!! 3. Clean sample in ethanol + IPA + N_2 rinse 4. Inspect sample	Comments:

4. Bottom contact, Lapping

Done at Supporting lab

Sample mount 1. Find "slipeklokke" for mounting sample on 2. Take off metal piece in center and put on hot plate, 150 ºC 3. Check sample thickness, and write it down 4. Put crystalbond 509 on metal piece, and make it flat and thin 5. Place sample, backside up on waxed metal piece and cover sample in more wax (to protect the edges during lapping) 6. Mount sample on "slipeklokke" and set it to 170-200 µm 1. Sample should be 100-150 µm thick when done, 120-150 µm is probably safer with regards to breakage. Remember that you must account for the wax thickness	Comments:
Lapping 1. Find some lapping sheets, the ones marked 4000 2. Either lap it in a fume cupboard or using a spinner with suction, avoid breathing in the antimony particles. Use plenty of water. 3. Remember to throw the lapping sheet and particles into toxic waste, e.g. use the box in the MBE lab. 4. Clean off the sample and remove it from the metal piece using the hot plate again. Slide it off carefully 5. Put it in acetone for 1-2 h to dissolve the remaining wax 6. Clean sample in acetone + IPA + N_2 blow (never let acetone dry on sample) 7. Inspection	Comments:

5. Bottom contact, Metallization

Done at nanolab.

Mounting 1. Clean and dehydrate a piece of silicon large enough to fit all samples 2. Spin ma-N 440 @ 1000 rpm / 30 s 3. Place all samples, backside up, on the photoresist *BEFORE* baking 4. Soft bake 110 ºC / 8-10 min	Comments:

Metallization 1. Oxide removal: Ar sputter, 16W, 1 min. 2. Do n-type contact deposition: Pd/Ge/Au/Pt/Au (87Å/560Å/233Å/476Å/1056Å) (make thicker Au layer at end, at least 300 nm)	
De-mount 1. Place samples in acetone for 1 hour in closed beaker (as always) 2. Remove and clean acetone + IPA + N_2 dry 3. Inspect	

6. Bottom contact, Annealing:

Done at Nanolab.

Rapid thermal annealer
 	
1. Make or use annealing recipe in the RTP
    1. Recipe made by Magnus can be used as a template. Made for Pd/Ge/Au/Pt/Au contacts for 45 s @ 300 ºC
    2. For Ti/Au only, a lower temperature can be used
	Comments:

7. Scribing:

Supporting lab (Nanolab)

1. Mount sample on blue tape
2. Make a recipe based on the length of the laser
3. Make sure you hit the laser at the end - will be difficult!! Machine not calibrated
    1. **DO NOT** scribe across the ridge - the laser will not work (just cleave)
    2. Use edge scribes for scribing perpendicular to the ridge
	Comments:

8. Mounting and bonding:

Either nanolab or basement at IET

1. Glue laser to a laser copper plate using silver epoxy or silver glue 2. Tape the bonding pads to the copper with kapton tape (double sided) Bonding pads must have soldered on wires BEFORE taping them to the copper

3. Wirebond the laser contacts to the laser bonding pads.

Bonding settings, nanolab:

T = 118 ºC

Ultrasonic:	180	280
Time:	100	55
Force:	85	65

Tail: 300
Feed +/- 12

⇨ Should be ready for testing! (If test setup in FTIR lab is operational)

Appendix D

WAVEGUIDE-COUPLING LASER STRUCTURES

This chapter contains the initial results of the output performance of the waveguide-coupling laser structures. The laser structure consists of two lasers, a straight waveguide laser and an S-bend waveguide laser, which are slightly separated at one end of the cavities, as shown in Fig. D.1. The separation gap s between two lasers is varied from 2 to 5 µm. The ridge waveguide structures of these lasers are formed by etching through the active region in order to disconnect the active region between two lasers, as seen in Fig. D.2. All lasers were fabricated and characterized following the procedures described in section 3.2, section 3.3 and in Appendix C.

Fig. D.3 and Fig. D.4 show the tuning behavior of the waveguide-coupling laser structures as a function of current ratio I_b/I_s for different separation gaps, where I_b is the injected current in the S-bend waveguide laser and I_s is the injected current in the straight waveguide laser. For the case of 5 µm separation gap, the tuning range can be up to 45 nm, as shown in Fig. D.3. As the separation gap reduces, the coupling between two lasers becomes stronger which results in a longer tuning range, as seen in Fig. D.4.

Finally, Fig. D.5 shows the output characteristics of the waveguide coupling laser structure as a function of I_b for different separation gaps when keeping I_s identical.

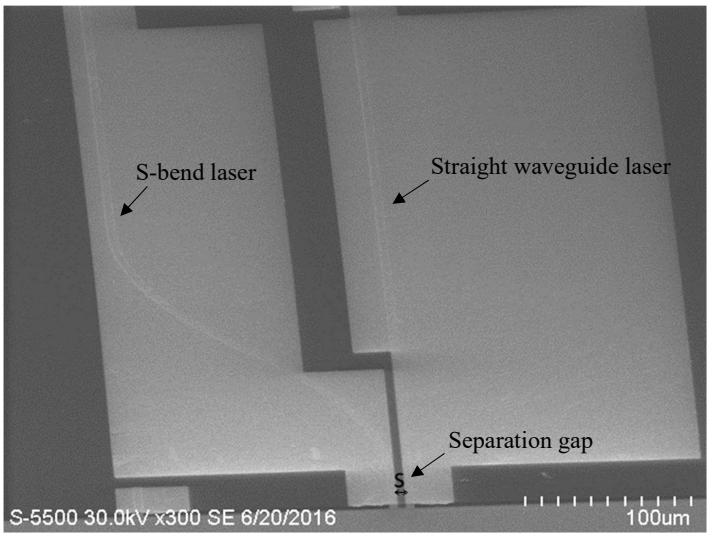

Figure D.1: Top view of the waveguide-coupling laser structure with two separated lasers. The S-bend laser has a bend radius of the curve section of 750 μm, creating a length difference ΔL = 50 μm between two lasers. The separation gap *s* between two lasers is varied from 2 to 5 μm.

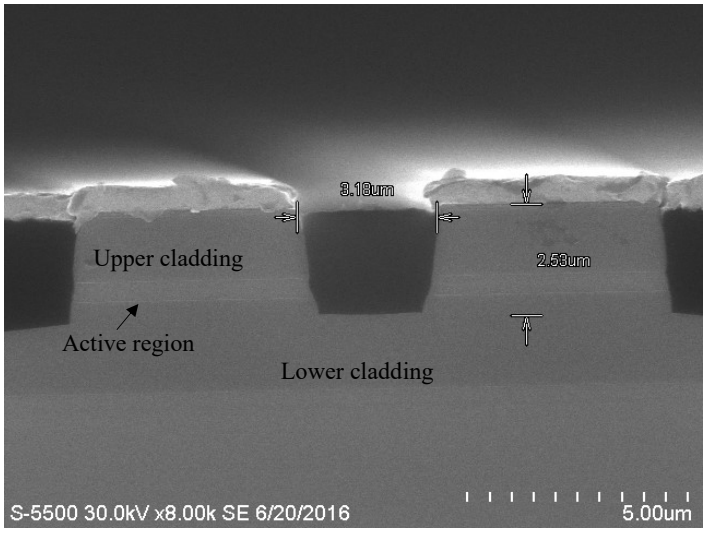

Figure D.2: Cross-section at the facet of the laser structures where two lasers are slightly separated. The separation gap between two lasers is measured to be about 3 μm. The etching was performed through the active region in order to disconnect the active region between two lasers.

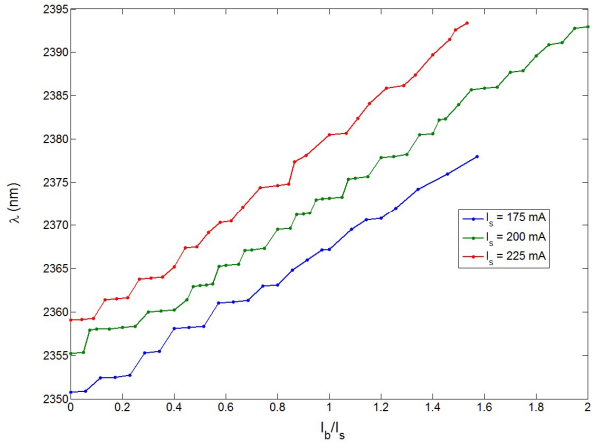

Figure D.3: Tuning behavior of the waveguide-coupling laser structure (separation gap s = 5 μm) as a function of current ratio I_b/I_s when I_s is constant and I_b is varied. The emitting wavelength was measured from the straight waveguide laser.

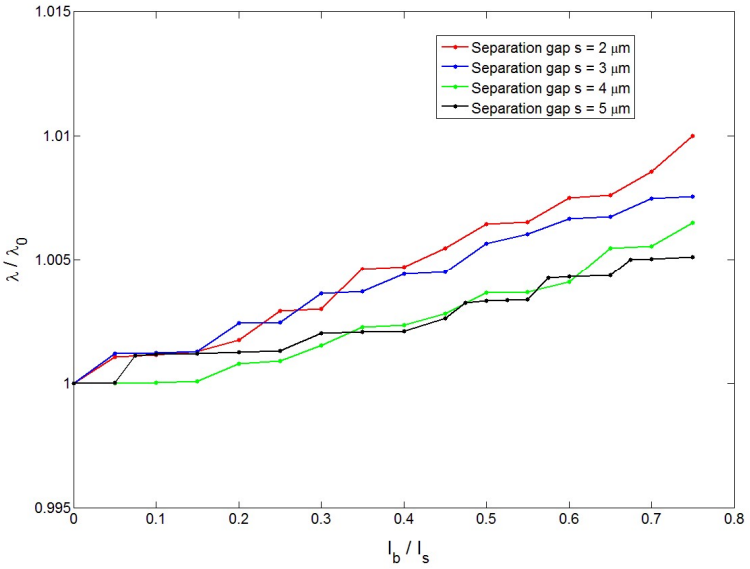

Figure D.4: Tuning behavior of the waveguide-coupling laser structure as a function of current ratio I_b/I_s for different separation gaps (I_s = 200 mA). The emitting wavelength was measured from the straight waveguide laser. The tuning rate is faster as the separation gap reduces due to stronger coupling between two lasers.

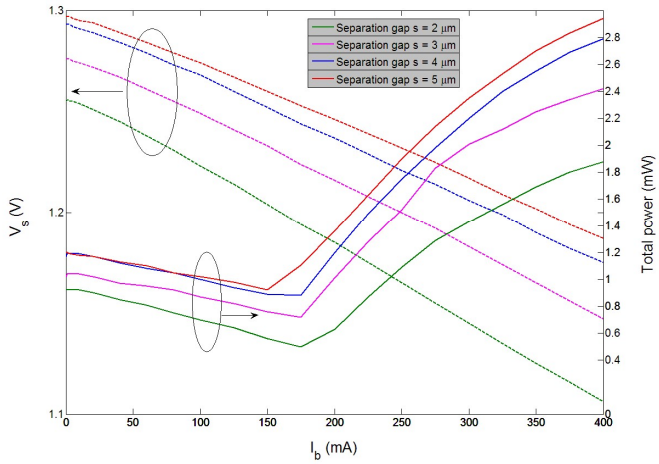

Figure D.5: Output characteristics of the waveguide-coupling laser structure as a function of I_b for different separation gaps (I_s was kept identical and equaled to 200 mA). The output power was measured from both lasers as they were close to each other, and the voltage was measured across the straight waveguide laser. For the output power, as I_b increases, the total output power slightly reduces due to light coupling before the S-bend laser starts lasing at around 160 mA.

References

[1] UK Health and safety executive, "EH40/2005 Workplace exposure limits" (2013).

[2] L. S. Rothman, I. E. Gordon, Y. Babikov, A. Barbe, D. C. Benner, P. F. Bernath, M. Birk, L. Bizzochi, V. Boudon, L. R. Brown, A. Campargue, K. Chance, E. A. Cohen, L. H. Coudert, V. M. Devi, B. J. Drouin, A. Fayt, J. -M. Flaud. "The HITRAN2012 molecular spectroscopic database". *Journal of Quantitative Spectroscopy and Radiative Transfer*, **130** (2013). pp. 4-50.

[3] S. Lundqvist, and P. Kluczynski. "Process analytical applications in the mid-infrared". *Proceedings of SPIE*, Vol. 7945 (2011).

[4] P. Werle. "A review of recent advances in semiconductor laser based gas monitors". *Spectrochimica Acta Part A: Molecular and Biomolecular Spectroscopy*, **54** (1998), pp. 197-236.

[5] Y. Rouillard, S. Belahsene, M. Jahjah, G. Boissier, P. Grech, G. Narcy, A. Vicet, L. Naehle, M. v. Edlinger, M. Fischer, and J. Koeth. "Quantum well lasers emitting between 3.0 and 3.4 µm for gas spectroscopy". *Proceedings of SPIE*, Vol. 8268 (2012).

[6] E. Tournié, and A. N. Baranov. "Mid-Infrared Semiconductor Lasers: A Review". *Advances in Semiconductor Lasers*. Editor. J. J. Coleman, B. Catrina & C. Jagadish. Academic Press (2012). ISBN: 9780123910660.

[7] N. Bandyopadhyay, Y. Bai, B. Gokden, A. Myzaferi, S. Tsao, S. Slivken, and M. Razaghi. "Watt level performance of quantum cascade lasers in room temperature continuous wave operation at λ~3.76 µm". *Applied Physics Letters*, **97** (2010), p. 131117.

[8] H. K. Choi, G. W. Turner, and S. J. Eglash, "High-power GaInAsSb-AlGaAsSb multiple-quantum-well diode lasers emitting at 1.9 µm". *IEEE Photonics Technology Letters*, **6** (1994). pp. 7-9.

[9] J. G. Kim, L. Shterengas, R. U. Martinelli, G. L. Belenky, D. Z. Garbuzov, and W. K. Chan. "Room-temperature 2.5 µm InGaAsSb/AlGaAsSb diode lasers emitting 1 W continuous waves". *Applied Physics Letters*, **81** (2002), pp. 3146-3148.

[10] D. Donetsky, G. Kipshidze, L. Shterengas, T. Hosoda, and G. Belenky. "2.3 µm type-I quantum well GaInAsSb/AlGaAsSb/GaSb laser diodes with quasi-CW output power of 1.4 W". *Electronics Letters*, **43** (2007), pp. 810-811.

[11] L. Shterengas, G. Belenky, M. V. Kisin, and D. Donetsky. "High power 2.4 µm heavily strained type-I quantum well GaSb-based diode lasers with more than 1 W of continuous wave output power and a maximum power-conversion efficiency of 17.5 %". *Applied Physics Letters*, **90** (2007), p. 011119.

[12] M. Kim, C. L. Canedy, W. W. Bewley, C. S. Kim, J. R. Lindle, J. Abell, I. Vurgaftman, and J. R. Meyer. "Interband cascade laser emitting at λ = 3.75 μm in continuous wave above room temperature". *Applied Physics Letters*, **92** (2008), p. 191110.

[13] Y. Bai, S. Slivken, S. R. Darvish, and M. Razeghi. "Room temperature continuous wave operation of quantum cascade lasers with 12.5 % wall plug efficiency". *Applied Physics Letters*, **93** (2008), p. 021103.

[14] A. Lyakh, C. Pflugl, L. Diehl, Q. J. Wang, F. Capasso, X. J. Wang, J. Y. Fan, T. Tanbun-Ek, R. Maulini, A. Tsekoun, R. Go, and C. Kumar N. Patel. "1.6 W high wall plug efficiency, continuous-wave room temperature quantum cascade laser emitting at 4.6 μm". *Applied Physics Letters*, **92** (2008), p. 111110.

[15] J. Chen, G. Kipshidze, L. Shterengas, T. Hosoda, Y. Wang, D. Donetsky, and G. Belenky. "2.7 μm GaSb-Based Diode Lasers With Quinary Waveguide". *IEEE Photonics Technology Letters*, **21** (2009), pp. 1112-1114.

[16] M. T. Kelemen, J. Gilly, S. Ahlert, H. Kissel, J. Biesenbach, M. Rattunde, and J. Wagner. "Diode laser arrays for 1.8 to 2.3 μm wavelength range". *Proceedings of SPIE*, Vol. 7483 (2009).

[17] T. Hosoda, G. Kipshidze, L. Shterengas, and G. Belenky. "Diode lasers emitting near 3.44 μm in continuous-wave regime at 300 K". *Electronics Letters*, **46** (2010), pp. 1455-1457.

[18] Y. Bai, N. Bandyopadhyay, S. Tsao, S. Slivken, and M. Razeghi. "Room temperature quantum cascade lasers with 27 % wall plug efficiency". *Applied Physics Letters*, **98** (2011), p. 181102.

[19] G. Belenky, L. Shterengas, G. Kipshidze, and T. Hosoda. "Type-I Diode Lasers for Spectral Region Above 3 μm". *IEEE Journal of Selected Topics in Quantum Electronics*, **17** (2011), pp. 1426-1434.

[20] Q. Y. Lu, Y. Bai, N. Bandyopadhyay, S. Slivken, and M. Razeghi. "2.4 W room temperature continuous wave operation of distributed feedback quantum cascade lasers". *Applied Physics Letters*, **98** (2011), p. 181106.

[21] J. D. Bruno, R. P. Leavitt, J. L. Bradshaw, K. M. Lascola, J. T. Pham, and F. J. Towner. "High-performance interband cascade lasers emitting between 3.3 and 3.5 μm". *Proceedings of SPIE*, Vol. 8374 (2012).

[22] R. Geunmin, A. N. Chryssis, J. Amirloo, S. Saini, F. J. Towner, and M. Dagenais. "Gain and Losses and Room-Temperature Operation in Interband Cascade Lasers". *IEEE Photonics Journal*, **4** (2012), pp. 133-142.

[23] W. W. Bewley, C. L. Canedy, C. S. Kim, M. Kim., C. D. Merritt, J. Abell, I. Vurgaftman, and J. R. Meyer. "High-power room-temperature continuous-wave mid-infrared interband cascade lasers". *Optics Express*, **20** (2012), pp. 20894-20901.

[24] W. W. Bewley, C. L. Canedy, C. S. Kim, M. Kim., C. D. Merritt, J. Abell, I. Vurgaftman, and J. R. Meyer. "Continuous-wave interband cascade lasers operating above room temperature at λ = 4.7-5.6 μm". *Optics Express*, **20** (2012), pp. 3235-3240.

[25] N. Bandyopadhyay, Y. Bai, S. Tsao, S. Nida, S. Slivken, and M. Razeghi. "Room temperature continuous wave operation of λ ~ 3–3.2 μm quantum cascade lasers". *Applied Physics Letters*, **101** (2012), p. 241110.

[26] N. Bandyopadhyay, S. Slivken, Y. Bai, and M. Razeghi. "High power, continuous wave, room temperature operation of λ ~ 3.4 μm and λ ~ 3.55 μm InP-based quantum cascade lasers". *Applied Physics Letters*, **100** (2012), p. 212104.

[27] L. Shterengas, R. Liang, G. Kipshidze, T. Hosoda, G. Belenky, S. S. Bowman, and R. L. Tober. "Cascade type-I quantum well diode lasers emitting 960 mW near 3 μm". *Applied Physics Letters*, **105** (2014), p. 161112.

[28] L. Shterengas, R. Liang, G. Kipshidze, T. Hosoda, S. Suchalkin, and G. Belenky. "Cascade pumping of GaSb-based type-I quantum well diode lasers". *Proceedings of SPIE*, Vol. 9002 (2014).

[29] R. Liang, L. Shterengas, T. Hosoda, A. Stein, M. Lu, G. Kipshidze, and G. Belenky. "Diffraction limited 3.15 μm cascade diode lasers". *Semiconductor Science and Technology*, **29** (2014), p. 115016.

[30] C. L. Canedy, J. Abell, C. D. Merritt, W. W. Bewley, C. S. Kim, M. Kim, I. Vurgaftman, and J. R. Meyer. "Pulsed and CW performance of 7-stage interband cascade lasers". *Optics Express*, **22** (2014), pp. 7702-7710.

[31] Y. Jiang, L. Li, R. Q. Yang, J. A. Gupta, G. C. Aers, E. Dupont, J. -M. Baribeau, X. Wu, and M. B. Johnson. "Type-I interband cascade lasers near 3.2 μm". *Applied Physics Letters*, **106** (2015), p. 041117.

[32] N. Kobayashi , and Y. Horikoshi, and C. Uemura. "Room temperature operation of InGaAsSb/AlGaAsSb laser at 1.8 μm wavelength". *Japan Journal of Applied Physics*, **19** (1980), pp. L30-32.

[33] D. A. Yarekha, G. Glastre, A. Perona, Y. Rouillard, F. Genty, E. M. Skouri, G. Boissier, P. Grech, A. Joullié, C. Alibert, and A. N. Baranov. "High temperature GaInSbAs/GaAlSbAs quantum well singlemode continuous wave lasers emitting near 2.3 μm". *Electronics Letters*, **36** (2000), pp. 537-539.

[34] R. Liang, J. Chen, G. Kipshidze, D. Westerfeld, L. Shterengas, and G. Belenky. "High-Power 2.2 μm Diode Lasers With Heavily Strained Active Region". *IEEE Photonics Technology Letters*, **23** (2011), pp. 603-605.

[35] L. Shterengas, G. L. Belenky, J. G. Kim, and R. U. Martinelli. "Design of high-power room-temperature continuous-wave GaSb-based type-I quantum-well lasers with λ > 2.5 μm". *Semiconductor Science and Technology*, **19** (2004), p. 655.

[36] M. Grau, C. Lin, O. Dier, C. Lauer, and M. -C. Amann. "Room-temperature operation of 3.26μm GaSb-based type-I lasers with quinternary AlGaInAsSb barriers". *Applied Physics Letters*, **87** (2005), p. 241104.

[37] V. Kristijonas, and and M. -C. Amann. "Room-temperature 3.73 μm GaSb-based type-I quantum-well lasers with quinternary barriers". *Semiconductor Science and Technology*, **27** (2012), p. 032001.

[38] A. Joullié, and P. Christol, "GaSb-based mid-infrared 2–5 μm laser diodes". *Comptes Rendus Physique*, **4** (2003), pp. 621-637.

[39] L. Shterengas, R. Liang, G. Kipshidze, T. Hosoda, S. Suchalkin, and G. Belenky. "Type-I quantum well cascade diode lasers emitting near 3 μm". *Applied Physics Letters*, **103** (2013), p. 121108.

[40] I. Vurgaftman, C. L. Canedy, C. S. Kim, M. Kim, W. W. Bewley, J. R. Lindle, J. Abell, and J. R. Meyer. "Mid-infrared interband cascade lasers operating at ambient temperatures". *New Journal of Physics*, **11** (2009), p. 125015.

[41] R. Q. Yang. "Infrared laser based on intersubband transitions in quantum wells". *Superlattices and Microstructures*, **17** (1995), pp. 77-83.

[42] W. W. Bewley, J. R. Lindle, C. S. Kim, M. Kim, C. L. Canedy, I. Vurgaftman, and J. R. Meyer. "Lifetimes and Auger coefficients in type-II W interband cascade lasers". *Applied Physics Letters*, **93** (2008), p. 041118.

[43] Z. Tian, L. Li, H. Ye, R. Q. Yang, T. D. Mishima, M. B. Santos, and M. B. Johnson. "InAs-based interband cascade lasers with emission wavelength at 10.4 μm". *Electronics Letters*, **48** (2012), pp. 113-114.

[44] Y. Bai, S. Slivken, S. R. Darvish, A. Haddadi, B. Gokden, and M. Razeghi. "High power broad area quantum cascade lasers". *Applied Physics Letters*, **95** (2009), p. 221104.

[45] S. Belahsene, L. Naehle, M. Fischer, J. Koeth, G. Boisser, P. Grech, G. Narcy, A. Vicet, and Y. Rouillard. "Laser Diodes for Gas Sensing Emitting at 3.06 μm at Room Temperature". *IEEE Photonics Technology Letters*, **22** (2010), pp. 1084-1086.

[46] M. Kamp, J. Hofmann, F, Schafer, M. Reinhard, M. Fischer, T. Bleuel, J. P. Reithmaier, and A. Forchel. "Lateral coupling – a material independent way to complex coupled DFB lasers". *Optical Materials*, **17** (2001), pp. 19-25.

[47] N. Koslowski, A. Heger, K. Roessner, M. Legge, J. Koeth, and L. Hildebrandt. "Monolithic wide tunable laser diodes for gas sensing at 2100 nm". *Proceedings of SPIE*, Vol. 8640 (2013).

[48] S. Wang, H.K. Choi, and I. Fattah. "Studies of semiconductor lasers of the interferometric and ring types". *IEEE Journal of Quantum Electronics*, **18** (1982), pp. 610-617.

[49] I. H. A. Fattah, and S. Wang. "Semiconductor interferometric laser". *Applied Physics Letters*, **41** (1982), pp. 112-114.

[50] M. Schilling, H. Schweizer, K. Dutting, W. Idler, E. Kuhn, A. Nowitzki, and K. Wunstel. "Widely tunable Y-coupled cavity integrated interferometric injection laser". *Electronics Letters*, **26** (1990), pp. 243-244.

[51] M. Schilling, E. Kuhn, G. Laube, H. Schweizer, K, Wunstel, and O. Hildebrand. "Integrated interferometric injection laser: novel fast and broad-band tunable monolithic light source". *IEEE Journal of Quantum Electronics*, **27** (1991), pp. 1616-1624.

[52] K. Dutting, O. Hildebrand, D. Baums, W. Idler, M. Schilling, and K. Wunstel. "Analysis and simple tuning scheme of asymmetric Y-lasers". *IEEE Journal of Quantum Electronics*, **30** (1994), pp. 654-659.

[53] O. Hildebrand, D. Baums, W. Idler, K. Dutting, G. Laube, and K. Wunstel. "The Y-laser: a multifunctional device for optical communication systems and switching networks". *Journal of Lightwave Technology*, **11** (1993), pp. 2066-2075.

[54] M. Kuznetsov, P. Verlangieri, A. G. Dentai, C. H. Joyner, and C. A. Burrus. "Asymmetric Y-branch tunable semiconductor laser with 1.0 THz tuning range". *IEEE Photonics Technology Letters*, **4** (1992), pp. 1093-1095.

[55] M. Kuznetsov. "Design of widely tunable semiconductor three-branch lasers". *Journal of Lightwave Technology*, **12** (1994), pp. 2100-2106.

[56] M. C. Zheng, P. Q. Liu, X. Wang, J. -Y. Fan, M. Troccoli, and C. F. Gmachl. "Wide single-mode tuning in quantum cascade lasers with asymmetric Mach-Zehnder interferometer type cavities with separately biased arms". *Applied Physics Letters*, **103** (2013), p. 211112.

[57] P. Q. Liu, X. Wang, and C. F. Gmachl. "Single-mode quantum cascade lasers employing asymmetric Mach-Zehnder interferometer type cavities". *Applied Physics Letters*, **101** (2012), p. 161115.

[58] J. Jin, L. Wang, T. Yu, Y. Wang, and J. -J. He. "Widely wavelength switchable V-coupled-cavity semiconductor laser with ~40 dB side-mode suppression ratio". *Optics Letters*, **36** (2011), pp. 4230-4232.

[59] J. -O. Wesstrom, S. Sarlet, S. Hammerfeldt, L. Lundqvist, P. Szabo, and P. -J. Rigole. "State-of-the-art performance of widely tunable modulated grating Y-branch lasers". In *Optical Fiber Communication Conference, OFC 2004*, (2004).

[60] R. Bugge, and B. -O. Fimland. "A novel tunable wet etched mid-IR pentenary AIInGaAsSb junction laser at 2.34-2.44 μm". In *Device Research Conference Digest, DRC 2005*, (2005).

[61] M. Breivik. *Fabrication of mid-infrared laser diodes for gas sensing applications*. Doctoral thesis, Norwegian University of Science and Technology, Trondheim (2013), ISBN: 9788247148990.

[62] J. Buus, M. -C. Amann, and D. J. Blumenthal. *Tunable diode lasers and related optical sources*. New York, Wiley-Interscience (2005), ISBN: 9780471208167.

[63] S. K. Patra. *Antimonide-based mid-infrared laser structures: Growth and characterization*. Doctoral thesis, Norwegian University of Science and Technology, Trondheim (2016), ISBN: 9788232620470.

[64] *Sacher Lasertechnik*. May 2016. URL: https://www.sacher-laser.com/home/laser-diodes/laser_diodes/fabry_perot/fabry_perot_diode_lasers_single_mode.html.

[65] G. P. Agrawal, N. K. Dutta. *Long-wavelength semiconductor lasers*. Van Nostrand Reinhold (1986). ISBN: 9870442209957.

[66] S. Adachi. "Band gaps and refractive indices of AlGaAsSb, GaInAsSb, and InPAsSb: Key properties for a variety of the 2–4 μm optoelectronic device applications". *Journal of Applied Physics*, **61** (1987), pp. 4869-4876.

[67] S. K. Patra, M. Kildemo, J. Gasiorowski, C. Cobet, B. -O. Fimland. "Dispersive refractive index in the 1-5 μm range of AlGaInAsSb pentenary and AlGaAsSb quaternary materials grown by molecular beam epitaxy". *To be submitted*.

[68] T. Hosoda, G. Kipshidze, L. Shterengas, S. Suchalkin, and G. Belenky. "200 mW type I GaSb-based laser diodes operating at 3 μm: Role of waveguide width". *Applied Physics Letters*, **94** (2009), p. 261104.

[69] M. Hirao, S. Tsuji, K. Mizuishi, A. Doi, and M. Nakamura. "Long Wavelength InGaAsP/InP Lasers for Optical Fiber Communication Systems". *Journal of Optical Communications*, **1** (1980), pp. 10-14.

[70] I. Mito, M. Kitamura, K. Kobayashi, S. Murata, M. Seki, Y. Odagiri, H. Nishimoto, M. Yamaguchi, and K. Kobayashi. "InGaAsP double-channel- planar-buried-heterostructure laser diode (DC-PBH LD) with effective current confinement". *Journal of Lightwave Technology*, **1** (1983), pp. 195-202.

[71] J. Wang, W. Yuan, C. S. Seibert, and D. C. Hall. "Loss characterization of high-index-contrast ridge waveguide oxide-confined InAlGaAs quantum well racetrack ring-resonator lasers". *Proceedings of SPIE*, Vol. 7230 (2009).

[72] D. Liang, J. Wang, and D. C. Hall. "High-efficiency native-oxide-passivated high-index-contrast ridge waveguide lasers". *Electronics Letters*, **42** (2006), pp. 349-350.

[73] D. Liang, J. Wang, J. Y. -T. Huang, J. -Y. Yeh, L. J. Mawst, and D. C. Hall. "Deep-Etched Native-Oxide-Confined High-Index-Contrast AlGaAs Heterostructure Lasers

With 1.3 μm Dilute-Nitride Quantum Wells". *IEEE Journal of Selected Topics in Quantum Electronics*, **13** (2007), pp. 1324-1331.

[74] T. Lee, C. Burrus, B. Miller, and R. Logan. "$Al_xGa_{1-x}As$ double-heterostructure rib-waveguide injection laser". *IEEE Journal of Quantum Electronics*, **11** (1975), pp. 432-435.

[75] K. Aiki, N. Nakamura, T. Kuroda, and J. Umeda. "Channeled-substrate planar structure (AlGa)As injection lasers". *Applied Physics Letters*, **30** (1977), pp. 649-651.

[76] R. B. Bylsma, G. E. Derkits, and W. R. Heffner. "Semiconductor laser reliability test structure and method". *Google Patents* (2001).

[77] J. Buus. "The effective index method and its application to semiconductor lasers". *IEEE Journal of Quantum Electronics*, **8** (1982), pp. 1083-1089.

[78] H. Kawaguchi, and T. Kawakami. "Transverse-mode control in an injection laser by a strip-loaded waveguide". *IEEE Journal of Quantum Electronics*, **13** (1977), pp. 556-560.

[79] K. S. Mobarhan. "Application Note: Test and Characterization of Laser Diodes: Determination of Principal Parameters". Newport Corporation.

[80] Y. Yonglin, and R. O'Dowd. "Influence of mode competition on the fast wavelength switching of an SG-DBR laser". *Journal of Lightwave Technology*, **20** (2002), pp. 700-704.

[81] L. A. Coldren, and S.W. Corzine. "Continuously-tunable single-frequency semiconductor lasers". *IEEE Journal of Quantum Electronics*, **23** (1987), pp. 903-908.

[82] M. Kuznetsov, P. Verlangieri, A. G. Dentai, C. H. Joyner, and C. A. Burrus. "Widely tunable (45 nm, 5.6 THz) multi-quantum-well three-branch Y3-lasers for WDM networks". *IEEE Photonics Technology Letters*, **5** (1993), pp. 879-882.

[83] K. Haddeland. *Fabrication of GaSb-based Y-junction laser for gas spectroscopy*. Master of Science thesis, Norwegian University of Science and Technology, Trondheim (2015).

[84] S. Forouhar, R. M. Briggs, C. Frez, K. J. Franz, and A. Ksendzov. "High-power laterally coupled distributed-feedback GaSb-based diode lasers at 2 μm wavelength". *Applied Physics Letters*, **100** (2012), p. 031107.

[85] R. M. Briggs, C. Frez, M. Bagheri, C. E. Borgentun, J. A. Gupta, M. F. Witinski, J. G. Anderson, and S. Forouhar. "Single-mode 2.65 μm InGaAsSb/AlInGaAsSb laterally coupled distributed-feedback diode lasers for atmospheric gas detection". *Optics Express*, **21** (2013), pp. 1317-1323.

[86] S. Dorian, C. Laurent, and T. Eric. "Mid-IR GaSb-based monolithic vertical-cavity surface-emitting lasers". *Journal of Physics D: Applied Physics*, **46** (2013), p. 495101.

[87] C. Gierl, T. Gruendl, P. Debernardi, K. Zogal, C. Grasse, H. A. Davani, G. Böhm, S. Jatta, F. Küppers, P. Meißner, and M.-C. Amann. "Surface micromachined tunable 1.55 µm-VCSEL with 102 nm continuous single-mode tuning". *Optics Express*, **19** (2011), pp. 17336-17343.

[88] G. Almuneau, F. Genty, A. Wilk, P. Grech, A. Joullié, and L. Chusseau. "GaInSb/AlGaAsSb strained quantum well semiconductor lasers for 1.55 µm operation". *Semiconductor Science and Technology*, **14** (1999), p. 89.

[89] K. Shim, H. Rabitz, and P. Dutta. "Band gap and lattice constant of $Ga_xIn_{1-x}As_ySb_{1-y}$". *Journal of Applied Physics*, **88** (2000), pp. 7157-7161.

[90] H. K. Choi, and G. W. Turner. "Antimonide-based strained quantum-well diode lasers". *Physica Scripta*, **T69** (1997), p. 17.

[91] R. Kaspi, C. A. Lu, T. C. Newell, C. Yang, and S. Luong. "GaSb-based >3 µm laser diodes grown with up to 2.4% compressive strain in the quantum wells using strain compensation". *Journal of Crystal Growth*, **424** (2015), pp. 24-27.

[92] S. D. Sifferman, H. P. Nair, R. Salas, N. T. Sheehan, S. J. Maddox, A. M. Crook, and S. R. Bank. "Highly Strained Mid-Infrared Type-I Diode Lasers on GaSb". *IEEE Journal of Selected Topics in Quantum Electronics*, **21** (2015), pp. 1-10.

[93] S. L. Chuang. "Efficient band-structure calculations of strained quantum wells". *Physical Review B*, **43** (1991), pp. 9649-9661.

[94] S. W. Corzine, R. -H. Yan, and L. A. Coldren. "Optical gain in III-V Bulk and Quantum well semiconductors". *Quantum Well Lasers*, Editor. P.S. Zory, Academic Press (1993), pp. 17-96. ISBN: 9780127818900.

[95] R. Bugge, and B. -O. Fimland. "Annealing effects in InGaAsSb quantum wells with pentenary AlInGaAsSb barriers". *Physica Scripta*, **T126** (2006), pp. 15-20.

[96] M. Rattunde, J. Schmitz, C. Mermelstein, R. Kiefer, and J. Wagner. "III-Sb-based Type-I QW Diode Lasers". *Mid-infrared Semiconductor Optoelectronics*, Editor. A. Krier, Springer London (2006), pp. 131-157. ISBN: 9781846282089.

[97] E. Selvig. *Molecular beam epitaxial growth and characterization of GaInAsSb/AlGaAsSb mid-infrared laser structures*. Doctoral thesis, Norwegian University of Science and Technology, Trondheim (2004). ISSN: 1503-8181.

[98] M. Hammer. "1-D mode solver for dielectric multilayer slab waveguides". *Software on line from SiIo.Eu*. URL: http://www.computational-photonics.eu/oms.html.

[99] M. Fatemi, and R. E. Stahlbush. "X-ray rocking curve measurement of composition and strain in Si-Ge buffer layers grown on Si substrates". *Applied Physics Letters*, **58** (1991), pp. 825-827.

[100] W. Bond. "Precision lattice constant determination". *Acta Crystallographica*, **13** (1960), pp. 814-818.

[101] M. Fatemi. "An x-ray rocking curve technique for the absolute characterization of epitaxial layers and single-crystal solids". *Applied Physics Letters*, **80** (2002), pp. 935-937.

[102] S. Perkowitz, D. Seiler, and W. M. Duncan. "Optical characterization in microelectronics manufacturing". *Journal of Research of the National Institute of Standards and Technology*, **99** (1994), p. 605.

[103] B. G. Streetman, and S. K. Banerjee. *Solid state electronic devices, 7th.* Pearson Education Inc. (2014). ISBN: 9780133356038.

[104] W. C. Simpson, and J. A. Yarmoff. "Fundamental studies of halogen reactions with III-V semiconductor surfaces". *Annual Review of Physical Chemistry*, **47** (1996), pp. 527-554.

[105] A. Piotrowska, E. Kaminska, T. T. Piotrowski, M. Guziewicz, K. Golaszewska, E. Papis, J. Wrobel, and L. Perchuc. "Application of CCl_2F_2- and CCl_4-based plasmas for RIE of GaSb and related materials". *Vacuum*, **56** (2000), pp. 57-61.

[106] K. Swaminathan, P. E. Janardhanan, and O. V. Sulima. "Inductively coupled plasma etching of III–V antimonides in $BCl_3/SiCl_4$ etch chemistry". *Thin Solid Films*, **516** (2008), pp. 8712-8716.

[107] L. Zhang, L. F. Lester, R. J. Shul, C. G. Willison, and R. P. Leavitt. "Inductively coupled plasma etching of III–V antimonides in BCl_3/Ar and Cl_2/Ar". *Journal of Vacuum Science & Technology B*, **17** (1999), pp. 965-969.

[108] S. J. Pearton, C. R. Abernathy, R. F. Kopf, and F. Ren. "Low Temperature Chlorine-Based Dry Etching of III–V Semiconductors". *Journal of The Electrochemical Society*, **141** (1994), pp. 2250-2256.

[109] G. A. Vawter. "Ion Beam Etching of Compound Semiconductors". *Handbook of Advanced Plasma Processing Techniques*, Editor. R. Shul and S. Pearton, Springer Berlin Heidelberg (2000), pp. 507-547. ISBN: 9783540667728.

[110] "Collection of etch recipe for the Plasmalab System 100 ICP 180". Oxford Instrument Plasma Technology (2009).

[111] H. C. Casey Jr., and M. B. Panish. *Heterostructure Lasers, Part B: Material and Operating Characteristics*. Orlando, Academic Press (1978). ISBN: 9780121631024.

[112] L. Redaelli, M. Martens, J. Piprek, H. Wenzel, C. Netzel, A. Linke, Y. V. Flores, S. Einfeldt, M. Kneissl, and G. Trankle. "Effect of ridge waveguide etch depth on laser threshold of InGaN MQW laser diodes". *Proceedings of SPIE*, Vol. 8262 (2012).

[113] N. T. Tran, M. Breivik, S. K. Patra, and B. -O. Fimland. "High precision AlGaAsSb ridge-waveguide etching by in situ reflectance monitored ICP-RIE". *Proceedings of SPIE*, Vol. 9134 (2014).

[114] J. A. Gupta, A. Bezinger, P. J. Barrios, J. Lapointe, D. Poitras, and P. Waldron. "High-resolution methane spectroscopy using InGaAsSb/AlInGaAsSb laterally-coupled index-grating distributed feedback laser diode at 3.23 μm". *Electronics Letters*, **48** (2012), pp. 396-397.

[115] M. Reason, B. R. Bennett, R. Magno, and J. B. Boos. "Molecular Beam Epitaxial Regrowth of Antimonide-Based Semiconductors". *Journal of Electronic Material*s, **40** (2011), pp. 6-10.

[116]. K. Haring, J. Viheriälä, M. -R. Viljanen, J. Paajaste, R. Koskinen, S. Suomalainen, A. Laakso, K. Leinonen, T. Niemi, and M. Guina. "Laterally-coupled distributed feedback InGaSb/GaSb diode lasers fabricated by nanoimprint lithography". *Electronics Letters*, **46** (2010), pp. 1146-1147.

[117] *Virginia Semiconductor*, "The General Properties of Si, Ge, SiGe, SiO_2 and Si_3N_4". (2002). URL: https://www.virginiasemi.com/pdf/generalpropertiesSi62002.pdf.

[118] *Ioffe Institute*. "New Semiconductor Materials. Biology sytems. Characteristics and Properties". URL: *http://www.ioffe.rssi.ru/SVA/NSM/Semicond/index.html*.

[119] A. Voigt (*Micro Resist Technology*). Personal communication, Aug. 2015.

[120] M. A. Hartney, D. W. Hess, and D. S. Soane. "Oxygen plasma etching for resist stripping and multilayer lithography". J*ournal of Vacuum Science & Technology B*, **7** (1989), pp. 1-13.

[121] E. Papis-Polakowska, A. Piotrowska, E. Kaminska, M. Guziewicz, T. T. Piotrowski, A. Kudla, and A. Wawro. "Chemical processing of GaSb related to surface preparation and patterning". *Proceedings of SPIE*, Vol. 4413 (2001).

[122] R. H. Williams. "III-V Semiconductor Surface Interactions". *Physics and Chemistry of III-V Compound Semiconductor Interfaces*. Editor. C. Wilmsen, Springer US (1985), pp. 1-72. ISBN: 9781468448351.

[123] K. Wasmer, C. Ballif, R. Gassilloud, C. Pouvreau, R. Rabe, J. Michler, J. -M. Breguet, J. -M. Solletti, A. Karimi, and D. Schulz. "Cleavage Fracture of Brittle Semiconductors from the Nanometer to the Centimeter Scale". *Advanced Engineering Materials*, **7** (2005), pp. 309-317.

[124] A. Tsekoun, R. Go, M. Pushkarsky, M. Razeghi, and C. K. N. Patel. "Improved performance of quantum cascade lasers via manufacturable quality epitaxial side down mounting process utilizing aluminum nitride heatsinks". *Proceedings of SPIE*, Vol. 6127 (2006).

[125] K. L. Chan, Z. Ning, D. Westerdahl, K. C. Wong, Y. W. Sun, A. Hartl, and M. O. Wenig. "Dispersive infrared spectroscopy measurements of atmospheric CO_2 using a Fabry–Pérot interferometer sensor". *Science of The Total Environment*, **472** (2014), pp. 27-35.

[126] B. W. Hakki, and T. L. Paoli. "Gain spectra in GaAs double−heterostructure injection lasers". *Journal of Applied Physics*, **46** (1975), pp. 1299-1306.

[127] M. Kinzer, Q. K. Yang, S. Hugger, M. Brunner, F. Fuchs, and J. Wagner. "Diffraction-Limited Infrared-Imaging of the Near-Field Intensity Emitted by Quantum-Cascade Lasers". *IEEE Journal of Quantum Electronics*, **48** (2012), pp. 696-702.

[128] J. L. Guttman, J. M. Fleischer, and A. M. Cary. "Real-Time Scanning Goniometric Radiometer for Rapid Characterization of Laser Diodes and VCSELs". In *Laser Beam Optics Characterization VI*, Munich, Germany (2001).

[129] E. B. Macak, W. D. Münz, and J. M. Rodenburg. "Plasma–surface interaction at sharp edges and corners during ion-assisted physical vapor deposition. Part I: Edge-related effects and their influence on coating morphology and composition". *Journal of Applied Physics*, **94** (2003), pp. 2829-2836.

[130] M. Hempel. *Defect mechanisms in diode lasers at high optical output power*. Doctoral thesis, Humboldt-Universität zu Berlin, Mathematisch-Naturwissenschaftliche Fakultät I, Berlin (2013).

[131] M. Ebrahim-Zadeh, and I. T. Sorokina. *Mid-Infrared Coherent Sources and Applications*. Springer Dordrecht (2008). ISBN: 9781402064630.

[132] N. Hodgson, H. Weber. *Laser Resonators and Beam Propagation*. Springer New York (2005), pp. 189-215. ISBN: 9870387400785.

[133] Y. Katagiri, and H. Ukita. "Ion beam sputtered $(SiO_2)_x(Si_3N_4)_{1-x}$ antireflection coatings on laser facets produced using O_2–N_2 discharges". *Applied Optics*, **29** (1990), pp. 5074-5079.

[134] O. Myrvang. *Facet coating on mid-IR laser diodes*. Master of Science thesis, Norwegian University of Science and Technology, Trondheim (2014).

[135] V. Mikhelashvili, and G. Eisenstein. "Optical and electrical characterization of the electron beam gun evaporated TiO_2 film". *Microelectronics Reliability*, **41** (2001), pp. 1057-1061.

[136] H. W. Lehmann, and K. Frick. "Optimizing deposition parameters of electron beam evaporated TiO_2 films". *Applied Optics*, **27** (1988), pp. 4920-4924.

[137] *Thorlabs Inc.*, "Beamsplitter-coated fiber optic patch cables". June 2016. URL: https://www.thorlabs.de.

[138] Y. Bai, S. R. Darvish, N. Bandyopadhyay, S. Slivken, and M. Razeghi. "Optimizing facet coating of quantum cascade lasers for low power consumption". *Journal of Applied Physics*, **109** (2011), p. 053103.

[139] A. D. Andreev, and D. V. Donetsky. "Analysis of temperature dependence of the threshold current in 2.3–2.6 μm InGaAsSb/AlGaAsSb quantum-well lasers". *Applied Physics Letters*, **74** (1999), pp. 2743-2745.

[140] H. Knötig, B. Hinkov, R. Weih, S. Hofling, J. Koeth, and G. Strasser. "Continuous-wave operation of vertically emitting ring interband cascade lasers at room temperature". *Applied Physics Letters*, **116** (2020), p. 131101.

[141] C. S. Seibert, D. C. Hall, D. Liang, and Z. A. Shellenbarger. "Reduction of AlGaAs Heterostructure High-Index-Contrast Ridge Waveguide Scattering Loss by Sidewall Smoothing Through Oxygen-Enhanced Wet Thermal Oxidation". *IEEE Photonics Technology Letters*, **22** (2010), pp. 18-20.

[142] A. Sarangan. *LIGHTS Online Optical Simulation Software*. Jan 2023. URL: http://maxwellsequations.org/.

ISBN 978-82-326-7544-9 (printed ver.)
ISBN 978-82-326-7543-2 (electronic ver.)
ISSN 1503-8181 (printed ver.)
ISSN 2703-8084 (online ver.)

NTNU

Norwegian University of
Science and Technology